

https://dspace.org/

Two-dimensional expansion wave diffraction around a 90 convex corner.

Mahomed, Irshaad

2014-02-12
http://hdl.handle.net10539/13736

Downloaded from a DSpace repository. https://dspace.org/

Two-dimensional expansion wave diffraction around a 90° convex corner

Irshaad Mahomed

A dissertation submitted to the Faculty of Engineering and the Built Environment, University of the Witwatersrand, Johannesburg, in fulfilment of the requirements for the degree of Master of Science in Engineering.

Johannesburg, July 2013

Declaration

I declare that this dissertation is my own, unaided work, except where otherwise acknowledged. It is being submitted for the degree of Master of Science in Engineering in the University of the Witwatersrand, Johannesburg. It has not been submitted before for any degree or examination at any other university.

Signed this 15th day of July 2013

Acknowledgements

I would like to thank the following people:

Prof B.W. Skews, for his continuous support, assistance and thoughtful insight during consultations. For his assistance and advice in preparation of material, for two international conferences where this work has been presented.

Mr. R.T Paton, for his assistance and advice in preparing the papers and presentations for the conferences and valuable assistance on the experimental, simulation and discussion aspects of this work.

The members of technical staff at the Mechanical Engineering laboratory for their work in the manufacturing and advice on the modification of the experimental rig, required for this work.

I would also like to thank the Flow Research Unit for making available funds to finance the study through the Fluxion scholarship.

Lastly, I would like to thank my parents and family for their continued support throughout my studies.

Abstract

The diffraction of a one-dimensional expansion wave over a 90° corner was explored using experiment and simulation methods. Unlike studies in shock diffraction, expansion wave diffraction was hardly explored in the literature and therefore is considered as novel. Two independent parameters were identified for the present study: 1) the initial diaphragm shock tube pressure ratio, and 2) the position of the diaphragm from the apex of the 90° corner. The experimentation only considered variation in the shock tube pressure ratio whereas the simulation varied both independent parameters. A Navier-Stokes solver with Menters SST k-ω turbulence model was found to adequately model the flow field.

A number of major flow features were identified, that occurred in the vicinity of the 90° corner. The flow features identified were: a shear layer which originated by flow separation near the apex of the 90° corner, a separation bubble that remained attached to a wall boundary in absence of rig-dependent effects, and a reflected compression wave due to perturbation signals generated by diffraction of the expansion wave.

For a narrow-width expansion wave existing prior to diffraction, it was found that after diffraction a reflected compression wave developed which would steepen into an outwardly propagating, weak, cylindrical shock wave. Other major flow features identified were a strong indication of an oblique shock located near the separation bubble and a large wake region immediately downstream of the separation bubble. The wake region, through schlieren imaging, was found to consist of two distinct layers.

The experimental results through shadowgraph and schlieren imaging have indicated large-scale turbulent structures within the separation bubble and the shear layer. Shear layer instability and vortex shedding off the separation bubble were also evident. The Navier-Stokes solver was found not to resolve the experimentally observed turbulence, the wake region and the vortex shedding.

Published Work

Aspects of this dissertation have been published in the following references:

I.Mahomed and B.W Skews, Diffraction of an expansion wave around a 90° corner, Presented at the 29^{th} International Symposium of Shock Waves, Madison, 2013

I.Mahomed and B.W Skews, Two-dimensional expansion wave diffraction, 30^{th} International Congress on High-Speed Photography and Photonics, R.Paton, B.Skews (ed.) ISBN: 978-0-620-56214-0, pp. 287-292, 2013

Contents

Declaration i

Acknowledgements iii

Abstract iv

Published Work v

Contents vi

List of Figures xiii

List of Tables xx

List of Symbols xxi

1 Introduction 1

1.1 Background 1

1.2 Problem Statement 2

1.3 Objectives 2

1.4 Chapter Overviews 3

2 Literature Survey **4**

2.1 Introduction 4

2.2 Basic Theories and Concepts 4

2.2.1 Shock Tube Theory 4

2.2.2 Wave Diagram 5

2.2.3 Real Flow Effects 7

2.2.4 The Ideal Gas Assumption 7

2.3 Unsteady One-Dimensional Wave Motion 8

2.3.1 General Behaviour 8

2.3.2 Finite-Compression Waves 9

2.3.3 Finite-Expansion Waves 10

2.4 Unsteady One-Dimensional Compressible Flow Equations 11

2.4.1 Moving Normal Shock Waves 11

2.4.2 Expansion Waves 12

2.5 The Shock Tube Relation 15

3 Preliminary Information **17**

3.1 Introduction 17

3.2 Solution to the Shock Tube Relation 17

3.3 Basic One Dimensional Expansion Wave Dynamics 19

3.3.1 Fundamental Behaviour 19

3.3.1.1 Pressure, Temperature, and Density Plots 19

3.3.1.2 Velocity and Mach Number Plots 20

3.3.2 Supersonic Flow Conditions 22
3.3.2.1 Acceleration of flow to Mach ≥ 1, through the expansion wave 22
3.3.2.2 Mach ≥ 1 for the trailing characteristic 25
3.3.3 Dynamic Motion of the Expansion Wave 26
3.3.4 Parameters Influencing the Propagation Speed of an Expansion Wave 27
3.4 The Reynolds Number 28

4 Experimental Method **29**

4.1 Introduction 29
4.2 Experimental Objectives 29
4.3 The Initial Shock Tube 30
4.3.1 Rig Description 30
4.3.2 Rig Constraints 31
4.4 The Modified Shock Tube 33
4.5 Facility Description and Instrumentation 35
4.6 Repeatability of Experimental Results and Rig Performance 36
4.6.1 Experiment Repeatability 36
4.6.2 Rig Performance 38
4.7 Experimental Procedure 38
4.7.1 The Pre-Check List 38
4.7.2 The Procedure and Precautions 39

5 Computational Method **40**

5.1 Introduction 40

5.2 Computational Objectives 41
5.3 Computational Model 41
5.3.1 The Experiment Domain 42
5.3.2 The Extended Domain 42
5.3.3 Euler Solver 43
5.3.4 Grid Independence Study 44
5.3.5 Validation Study 48
5.4 Turbulence Modelling 51
5.4.1 Grid Generation and the RANS Solver 51
5.4.1.1 Menter's SST k-w Turbulence Model 52
5.4.1.2 Laminar Model 55
5.5 Comparison of Results 56
5.6 Conclusion 59

6 Results and Discussion **60**

6.1 Introduction 60
6.2 Summary of Test Cases 60
6.3 Major Flow Features 61
6.4 The Reflected and Diffracted Waves 64
6.4.1 The Diffracted Region 65
6.4.2 The Reflected Compression Wave 66
6.4.3 The Steepening of The Reflected Compression Wave 68
6.5 The Separation Bubble 71

6.5.1 The Viscous Vortex and the Near-Corner Flow Structure 75
6.5.2 Shear Layer Instability 77
6.5.3 Vortex Shedding 78
6.5.4 The Wake Region 79
6.5.5 Characterizing the Separation Bubble 80
6.6 The Oblique and Re-Compression Shock 84
6.6.1 Identification of the Oblique Shock 85
6.6.2 Evolution of the Supersonic Region 86
6.6.3 Shock-Free Transition from Super- to Sub-Sonic Flow 89
6.6.4 Behaviour of the Oblique shock 91
6.6.5 The Re-Compression Shock 93
6.7 Sonic and Supersonic Flow Conditions 95
6.7.1 Euler Solver 95
6.7.2 Flow Features for P41 > 10.4 97
6.7.3 Analysis of the External Flow Field 98
6.7.3.1 The Oblique Shock 98
6.7.3.2 The Supersonic Region 100
6.7.3.3 The Reflected Compression Waves 101

7 Conclusions **103**

7.1 Summary of Results for the Major Flow Features 103
7.2 Summary of Results for the Reflected and Diffracted Waves 104
7.3 Summary of Results for the Separation Bubble 105

7.4 Summary of Results for the Oblique and Re-compression Shock 106

7.5 Summary of Results for Sonic and Supersonic Flow Conditions 107

7.6 Comparison With Shock Wave Diffraction Over a 90° Corner 108

8 Recommendations 109

8.1 Experiment and Simulation 109

8.2 Further Research 110

A Appendix A: Details of the Verification Check for the Shock Tube Relation 114

B Appendix B: Details of the Equipment and Instrumentation 116

B.1 Pressure Sensor and Signal Conditioner 116

B.2 Oscilloscope 117

B.3 Time Delay Unit and Trigger Box 117

B.4 High Resolution and High-Speed Camera's 118

C Appendix C: Establishing the Onset of Rig-Dependent Effects 119

C.1 Rig-Dependent Effects 119

C.1.1 Simulation and High-Speed Imaging 119

C.1.1.1 Simulation Data 120

C.1.1.2 High Speed Image Data 122

C.1.2 High-Resolution Imaging 122

C.1.2.1 Establishing Onset Rig-Dependency for High-Resolution Images 124

C.1.2.2 High-Resolution Image Data 125

D Appendix D: Simulation results for P41 = 18 129

E Appendix E: Digital Appendix **130**

List of Figures

1.1 Schematic to illustrate the concept between shock and expansion wave diffraction, prior to propagation over a 90° convex corner. 1

1.2 Shock tube schematic with 90° test piece to illustrate definition of the independent parameters for the present study. 2

2.1 Annotated diagram of a standard, simple shock tube. 5

2.2 Wave diagram describing flow events in a shock tube following diaphragm rupture. 6

2.3 Generation of compression waves by piston motion. 9

2.4 Wave diagram to a illustrate finite compression wave. 9

2.5 Generation of expansion waves by piston motion. 10

2.6 Wave diagram to illustrate a finite expansion wave. 10

2.7 Post diaphragm-burst shock tube events with vector notation for the wave elements. 11

3.1 Post diaphragm-burst shock tube events with vector notation for the wave elements. 17

3.2 Variation of P34 and P21 with P41. 20

3.3 Variation of T34 and ρ34 with P41. (P41 ranged between 1-60 bar, P1 = 0.834 bar and T1 = 300 K.) 21

3.4 Variation of P43 with P41. (P41 ranged between 1-60 bar, P1 = 0.834 bar and T1 = 300 K.) 21

3.5 Variation of the flow velocity, sound speed and propagation speed of the trailing characteristic, at region 3, with P41. 23

3.6 Variation of the flow and trailing characteristic Mach numbers at region 3, with P41. 24

3.7 Variation of expansion wave width with P41 against non-dimensional time for a one-dimensional expansion wave. Maximum propagation time considered was 800 μs. 27

4.1 Schematic of the shock tube to illustrate the independent parameters. 31

4.2 Exploded isometric view of the initial shock tube. 32

4.3 CAD drawing of the flange. Thickness = 10 mm. 34

4.4 Exploded CAD drawing of the modified shock tube. 35

4.5 Photograph illustrating the modified shock tube. 36

4.6 Selected high-speed shadowgraph images to illustrate experiment repeatability. **(a, b)**: P41 = 1.8, **(c, d)**: P41 = 7.7. t_f = 350 μs. 37

4.7 Selected high-speed shadowgraph images to illustrate experiment repeatability. **(a, b)**: P41 = 1.8, **(c, d)**: P41 = 7.7. t_f = 400 μs. 37

5.1 Schematic of the experimental flow domain as modelled in ANSYS FLUENT. 42

5.2 Schematic of the extended flow domain modelled in ANSYS FLUENT 43

5.3 Plot of static pressure through the one-dimensional region of the expansion wave, at fixed time and shown for various mesh topologies. 45

5.4 Verification plot for the 1 dimensional region established by considering the variation of gas velocity through the expansion wave. 46

5.5 Verification plot for the 2 dimensional region taken below the 90° corner. . . 47

5.6 Qualitative comparison between the Euler solver and high-speed shadowgraph images at P41 = 3.2 (± 0.2 bar for experiment). Times from arrival of leading characteristic at the corner (μs): **(a, b)** 150, **(c, d)** 232, **(e, f)** 317. 49

5.7 Qualitative comparison between the Euler solver and high-speed shadowgraph images at P41 = 6.5 (± 0.2 bar for experiment). Times from arrival of leading characteristic at the corner (μs): **(a, b)** 150, **(c, d)** 232, **(e, f)** 317. 50

5.8 Variation of velocity through the boundary layer in a region of uniform flow and $\frac{\partial p}{\partial x} \approx 0$ 52

5.9 Region for the velocity profile plot through the boundary layer 53

5.10 Grid topology for the Navier-Stokes solver for the *extended domain.* 54

5.11 Grid topology at the diffraction corner for the Laminar solver for the *rig domain.* 56

5.12 Qualitative comparison between Menter's SST k-ω turbulence model and high-speed shadowgraph images at P41 = 3.2 (± 0.2 bar for experiment). Times from arrival of leading characteristic at the corner (μs): **(a, b)** 150, **(c, d)** 232, **(e, f)** 317. 57

5.13 Plot of stagnation point distance from the 90° corner against non-dimensional time, for the various solvers, at P41 = 3.2 and 7.7. 58

5.14 Plot of stagnation point distance from the 90° corner against non-dimensional time, for Menter's SST k-ω turbulence model, the Laminar solver, and experiment data, at P41 = 3.2 and 7.7. 58

6.1 Selected, high-speed shadowgraph images to sequentially illustrate the flow field at the diffraction corner for P41 = 3.2 and 7.7. Time-delay values (μs): **(a, b)**: 200, **(c, d)**: 400, **(e, f)**: 600. 61

6.2 High speed shadowgraph images for P41 = 3.2 (**a**), 7.7 (**b**) at a time delay of 300 μs 62

6.3 Pressure contours and velocity vector plots using Menters SST k-ω turbulence model, for P41 = 3.2 and 7.7, at t_f = 150 μs. 62

6.4 Annotated contour plot of pressure for P41 = 6 at t_f = 250 μs and D = 0 mm 65

6.5 Contour plot of pressure for P41 = 6 at t_f = 250 μs and D = 70 mm 65

6.6 Contours of pressure for P41 = 3 and 6, D = 40 mm. Times, t_f (μs) **(a,b)**: 350, **(c,d)**: 400, **(e,f)**: 450. 67

6.7 Pressure profile along shock tube channel height for P41 = 3, D = 40 mm and at three instances of time (μs). The channel height of 0 mm refers to the horizontal wall position of the test corner and the origin of each pressure curve coincided with the stagantion point of the primary separation bubble (on the horizontal wall). 68

6.8 Contours of pressure for P41 = 9, D = 70 mm. Times, t_f (μs) **(a)**: 350, **(b)**: 400, **(c)**: 450) 69

6.9 Instantaneous contours of pressure for P41 = 3, D = 0 and 10 mm. Times, t_f (μs) **(a,b)**: 50, **(c,d)**: 200, **(e,f)**: 350 70

6.10 Instantaneous pressure profile, along the shock tube channel height, for P41 = 3 and 6. Time, t_f (μs) 400. D (mm): **(a,b)**: 10, **(c,d)**: 40, **(e,f)**: 70. 71

6.11 Instantaneous pressure profile along shock tube channel height for P41 = 3 and 6. Time, t_f (μs) 400. D (mm) = 10, 40, and 70. 72

6.12 Shadowgraph images (high resolution) for P41 = 3.2, demonstrating formation of the separation bubble at early times. 72

6.13 Shadowgraph images (high resolution) for P41 = 3.2, demonstrating formation of the separation bubble at late time and rig dependent effects 73

6.14 Shadowgraph images (high resolution) for P41 = 3.2 and 7.7 to demonstrate features of the separation bubble prior to rig dependent effects. Time-delay values (μs): **(a,e)** 200, **(b,f)** 250, **(c,g)** 300, **(d,h)** 350. 74

6.15 Velocity vector plot illustrating the flow structure near the diffraction corner using Menters SST k-ω solver for P41 = 3.2 and 7.7 at 320 μs. Zoomed-in images are inlcuded in the bottom row. (D = 83 mm). 75

6.16 Velocity vector plot illustrating the flow structure near the diffraction corner using Menters SST k-ω solver for P41 = 3.2 and 7.7 at 200 μs. Zoomed-in images are inlcuded in the bottom row. D = 83 mm. 77

6.17 Shadowgraph images for P41 = 6.5 emphasizing the wake region and vortex shedding. (D = 83 mm). 78

6.18 Schlieren imaging with a horizontal knife-edge highlighting structure in the wake region and shear layer for P41 = 6.5 and time-delay (μs): 300 **(a)**, 350 **(b)**, $D = 83$ mm. 79

6.19 Density contours for P41 = 3 and time, $t_f = 200$ μs. 81

6.20 Density contours for P41 = 6 and time, $t_f = 200$ μs. 82

6.21 Density contours for P41 = 9 and time, $t_f = 200$ μs. 82

6.22 Horizontal movement of the stagnation point from the 90° corner for P41 = 3, 6, 9 and $D = 10$ mm. 83

6.23 Horizontal movement of the stagnation point from the 90° corner for P41 = 3, 6, 9 and $D = 40$ mm 83

6.24 Horizontal movement of the stagnation point from the 90° corner for P41 = 3, 6, 9 and $D = 70$ mm 84

6.25 Shadowgraph images to highlight the strong indication of the shock positioned towards the rear of above the separation bubble; identified for P41 = 7.7 and time-delay (μs): 300 (**a**) and 350 (**b**) 85

6.26 Vector plot of velocity magnitude to classify the type of shock. The selected conditions found to favourably produce this shock are: P41 = 9, $D = 10$ mm, and $t_f = 600$ μs. 86

6.27 Mach number contours for P41 = 3 and $D = 0$ and 40 mm. Simulation times, t_f (μs): **(a, b)** 100, **(c, d)** 200, **(e, f)** 300. 87

6.28 Mach number contours for P41 = 3 and $D = 0$ and 40 mm. Simulation times (μs): **(a, b)** 400, **(c, d)** 500, **(e, f)** 600. 88

6.29 Mach number contours for P41 = 6 and 9 for $D = 10$ mm. Simulation times (μs): **(a, b)** 100, **(c, d)** 200, **(e, f)** 300. Results for P41 = 9 are slightly zoomed-in. 89

6.30 Mach number contours for P41 = 6 and 9 for $D = 40$ mm. Simulation times (μs): **(a, b)** 100, **(c, d)** 200, **(e, f)** 300. Results for P41 = 9, are slightly zoomed-in. 90

6.31 Mach number contours for P41 = 3 and $t_f = 600$ μs. D (mm) : **(a)** 0, **(b)** 10, **(c)** 40, and **(d)** 70. 91

6.32 Contour plots of Mach number for P41 = 6 and $t_f = 600$ μs. D (mm) : **(a)** 0, **(b)** 10, **(c)** 40 and **(d)** 70. 92

6.33 Contour plots of Mach number with supersonic region, for P41 = 9 and $t_f = 600$ μs. D (mm) = **(a)** 0, **(b)** 10, **(c)** 40, **(d)** 70. 92

6.34 Contour plots of, **(a)** Mach number and, **(b)** density to illustrate the re-compression shock. P41 = 3, $t_f = 600$ μs and $D = 40$ mm. 94

6.35 Contour plots of, **(a)** Mach number and, **(b)** density to illustrate the re-compression shock. P41 = 6, $t_f = 600$ μs and $D = 40$ mm. 94

6.36 Comparison between Euler (Left column) and Navier-stokes (Right column) solutions by Mach number contours for P41 = 15 and $t_f = 300$ μs. D (mm): (**a**, **b**) 0, (**c**, **d**) 10, and (**e**, **f**) 40. 96

6.37 Contour plot of Mach number to illustrate flow features towards the separation bubble for supersonic following flow. P41 = 15, $D = 10$ mm and $t_f = 500$ μs. 97

6.38 Contour plot of Mach number to illustrate flow features away from the separation bubble for supersonic following flow. P41 = 15, $D = 10$ mm and $t_f = 500$ μs. 98

6.39 Contour plots of Mach number to emphasize the shock structure with variation in D. P41 = 12 and $t_f = 300$ μs. 99

6.40 Contour plots of Mach number, to emphasize the shock structure, with variation in D. P41 = 15 and $t_f = 300$ μs. 99

6.41 Contour plots of Mach number, to emphasize the shock structure, with variation in D. P41 = 12 and $t_f = 600$ μs. 100

6.42 Contour plots of Mach number, to emphasize the shock structure, with variation in D. P41 = 15 and $t_f = 600$ μs. 101

C.1 Contours of pressure for P41 = 3.2 at various times, measured from the 90° corner. 120

C.2 Contours of pressure for P41 = 7.7 at various times, measured from the 90° corner. 121

C.3 High-speed shadowgraph images for P41 = 3.2 at various times, measured from the 90° corner. 123

C.4 High-speed shadowgraph images for P41 = 7.7 at various times, measured from the 90° corner. 123

C.5 Plot of stagnation point position from the 90° corner for high-speed shadowgraph data. 124

C.6 Identification of rig-dependent effects for the high-resolution data, using a graphical plot of stagnation point position from the 90° corner for the high-speed data. 125

C.7 High-resolution shadowgraph images for P41 = 3.2 at various time-delay values. 126

C.8 High-resolution shadowgraph images for P41 = 7.7 at various time-delay values 127

D.1 Contour plots of Mach number, to emphasize the shock structure, with variation in D. P41 = 18 and $t_f = 300$ μs. 129

E.1 Flow chart to illustrate the important steps in the solution of the shock tube relation. 131

List of Tables

3.1 Directional behaviour of a left running expansion wave with Mach number. . 23

3.2 Reynolds number per unit length behind the expansion wave 28

4.1 Pressure data for experimentation in the driver section 30

5.1 Initial conditions in the driver section 44

5.2 Summary of mesh data for the Euler solver 48

5.3 Summary of mesh data for the Navier-Stokes solver 53

5.4 Summary of mesh data for the Navier-Stokes solver 55

A.1 Experimental data to verify the numerical code for the shock tube relation. . 114

A.2 Analytical data to verify the numerical code for the shock tube relation. . . . 115

B.1 Calibration and model data for pressure transducers 116

B.2 Model data for the trigger-out oscilloscope 117

B.3 Model data for the trigger-out oscilloscope 117

B.4 Model data for the time-delay unit 117

B.5 Model data for the high-speed digital camera 118

List of Symbols

The units of quantities defined by a symbol are indicated in square brackets following the description of the symbol. Quantities with no indicated units may be assumed to be dimensionless.

a Local sound speed [m.s^{-1}].

γ Ratio of specific heats.

M Mach number.

P Static pressure [kPa].

ρ Density [kg.m^{-3}].

T Absolute temperature [K].

t Flow time [s].

u Velocity [m.s^{-1}].

1 Introduction

1.1 Background

Consider the one-dimensional, non-linear wave system generated in a shock tube as shown in figure 1.1. With reference to this figure, the shock wave propagates downstream into the driven section and the expansion waves propagate upstream, into the driver section, of the shock tube. Should a backward facing step be positioned downstream in the driven section, the shock wave will undergo diffraction. In the literature, much attention was given to shock diffraction studies and are too numerous to mention. Skews [1967] experimentally explored the behaviour of shock diffraction over various two-dimensional sharp corners. Mathews and Howard [1956] experimentally studied the basic flow structure behind a diffracting shock wave. The basic flow structure following shock diffraction was found to consist of expansion waves, a shear layer, a contact surface, and vortices. Now consider the backward facing step positioned upstream, in the driver chamber, of the shock tube. The current study seeks to explore the diffraction process of an unsteady expansion wave around a two dimensional sharp corner. To date, hardly any experimental or numerical work exists in the literature on the diffraction of an unsteady expansion wave over large corner geometries.

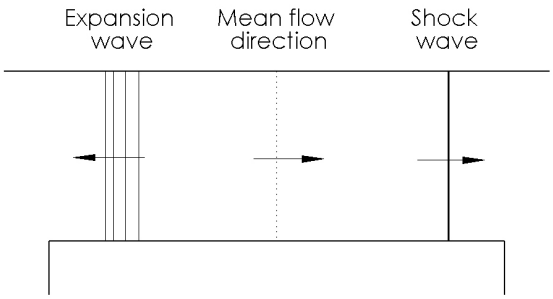


Figure 1.1: Schematic to illustrate the concept between shock and expansion wave diffraction, prior to propagation over a 90° convex corner.

1.2 Problem Statement

The idea of placing a backward facing step in the driver section of the shock tube has not been considered before. A recent (2011) unpublished study at the University of the Witwatersrand, Flow Research Unit, identified an unusual flow field pattern upon expansion wave diffraction around planar, two-dimensional sharp corners. No immediate explanation for this flow field could be offered at the time.

The present study seeks to qualitatively explore expansion wave diffraction around a 90° corner using flow visualization and simulation techniques. Two independent parameters were to be considered: 1) a range of diaphragm pressure ratios (P41) and 2) placement of the diaphragm at various downstream positions from the corner (D). The simulation technique was to consider Euler and viscous computations. A schematic of the shock tube used in the present study, is shown in Figure 1.2 to visually define the independent parameters: P41 = $\frac{P_4}{P_1}$ and D.

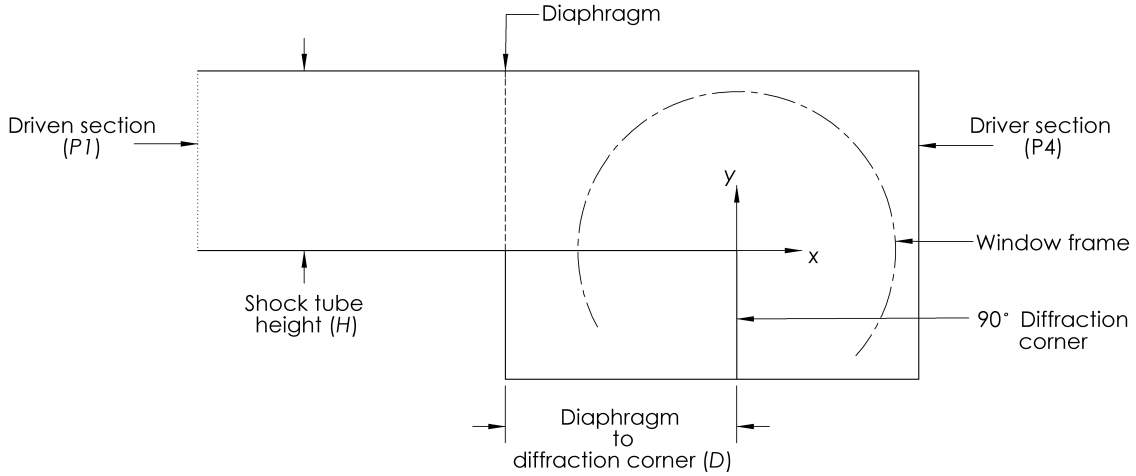


Figure 1.2: Shock tube schematic with 90° test piece to illustrate definition of the independent parameters for the present study.

1.3 Objectives

The objectives for the qualitative study of expansion wave diffraction around a 90° corner , using experiment and simulation techniques, was established as:

- To improve the operation of an existing experiment rig and position the diaphragm closer to the 90° corner.
- To experimentally explore the effect of varying the diaphragm pressure ratio (P41) using shadowgraph and schlieren flow visualization techniques.
- Using Euler and Navier-Stokes solvers, explore the effect of varying D (the downstream distance between the diaphragm and the 90° corner), and P41 (the diaphragm pressure ratio), beyond those values achievable by experiment.
- To identify and describe the flow physics of the major flow features that characterize expansion wave diffraction.

1.4 Chapter Overviews

This section provides an overview of the dissertation layout. The present chapter introduced the topic of expansion wave diffraction and broadly described the studies objectives.

Chapter 2 presents literature material relevant to expansion wave diffraction, discussing finite non-linear waves and introducing relevant equations for the one-dimensional expansion wave. This theory was applied in Chapter 3 and built upon certain information contained in the literature that was not readily found in any standard text on gas dynamics or relevant publications and was found useful for the study.

Chapter 4 describes the experimental method. The experimental objectives were expanded upon from section 1.3. Details are provided on the experiment rig with the required modifications including a brief operational procedure. Since the experimental facility was commissioned for the present study, major precautions and hazards are discussed in some detail. The performance of the rig was qualitatively assessed to establish experimental repeatability.

The computational method is discussed in Chapter 5. The simulation objectives were expanded upon from section 1.3. The pre-processing and solver set-up for Euler and Navier-stokes solutions are described.

The results from the experiment and simulation are discussed in Chapter 6 where four, distinct topic areas were developed. This chapter concludes with a section on Consolidation of Results.

Chapters 7 and 8 presents the conclusions and recommendations, respectively. Significant results and findings from the study are summarized in the conclusion. Recommendations for future work and areas highlighted for further study are documented.

2 Literature Survey

2.1 Introduction

Appropriate theories and concepts relevant to the study of expansion (rarefaction) wave diffraction are reviewed in the present and following chapters; where the post diffracted flow-field was assumed as two-dimensional. In senior texts on gas dynamics, such as Shapiro [2002], it was found the theory and analysis of expansion waves did not extend beyond the expansion wave being considered as one-dimensional.

2.2 Basic Theories and Concepts

It is appropriate to introduce some aspects of shock tube theory and real flow effects and thereafter consider unsteady wave motion. In an ideal, one-dimensional, shock tube environment, unsteady wave motion is associated with the shock and expansion waves.

Real flow effects in a shock tube should be considered when analysing the experimental results. A comprehensive treatment on the shock tube can be found in Wright [1961] or Skews [1961]. The solution to the one-dimensional, unsteady, compressible flow equations was also important to determine the flow properties in any simple region of the shock tube of which pertinent equations are covered in this chapter. A set of these equations relate to the expansion wave and formed the basis for Chapter 3 where certain graphical plots and analysis are presented. These plots are not readily covered in the literature.

2.2.1 Shock Tube Theory

A shock tube is a gas dynamic instrument used primarily to study the effects caused by shock wave interaction with various objects and high temperature flows. A shock tube with a constant flow cross-section and consisting of two chambers separated by a gas-tight diaphragm

appears sketched in figure 2.1. One chamber is pressurized and denoted the driver section whereas the remaining chamber is either at a lower pressure relative to the driver section or left-open to ambient conditions. This chamber is denoted as the driven section. A pressure differential is applied across the diaphragm which can be achieved through positive pressure in the driver section or creating a partial vacuum in the driven section.

To study shock wave diffraction, a shock tube of typical construction has a viewing window located in the driven section, to visualize shock phenomena. Clearly, to study the diffraction (or reflection and refraction effects) of an expansion wave, a viewing window was necessary in the driver section. This made construction of the shock tube for the present study of an unusual design.

The flow field generated in a shock tube following diaphragm rupture and in absence of wave interactions is governed by the one-dimensional unsteady, compressible flow equations. These equations assume ideal gas behaviour but neglect factors such as: fluid viscosity, heat transfer, surface roughness effects and diaphragm effects. These factors are present in an experiment and would lead to real flow effects which are considered from a qualitative view-point since this was found helpful to explain portions of the experimental results. Before proceeding with real flow effects, the wave diagram is introduced as this was a convenient method to explain flow events in a one-dimensional shock tube.

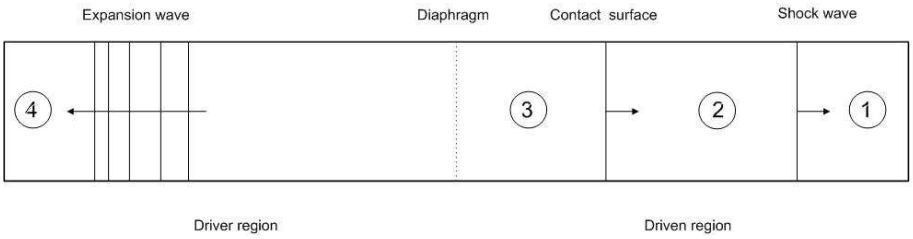


Figure 2.1: Annotated diagram of a standard, simple shock tube.

2.2.2 Wave Diagram

Upon diaphragm rupture, a shock wave develops by coalescence of simple compression waves (introduced in section 2.3) and propagates downstream into the driven section. Simultaneously, an expansion wave develops and propagates upstream into the driver section. We note here the direction of travel of the expansion wave which is opposite to both that of the shock wave and the flows' direction. Consider a shock tube closed at both ends with the driver section pressurized as sketched in figure 2.1. The flow field in the shock tube is completely specified by static conditions of pressure and temperature in regions 1 and 4, prior to diaphragm rupture where the shock tube regions of interest are labelled in figure 2.2. The ratio

of the initial pressure in the driver and driven regions is termed the *diaphragm pressure ratio* (P41).

The air ahead of the shock wave undergoes shock compression raising its temperature whereas the air ahead of the expansion wave expands to a lower temperature. As a result, the steady regions of flow behind the shock and expansion waves have a mismatch in temperature (and likewise for density). This mismatch is resolved by the presence of a contact surface. The contact surface moves at the velocity of the flow which is equivalent in regions 2 and 3, as expected, the static pressure is preserved across the contact surface.

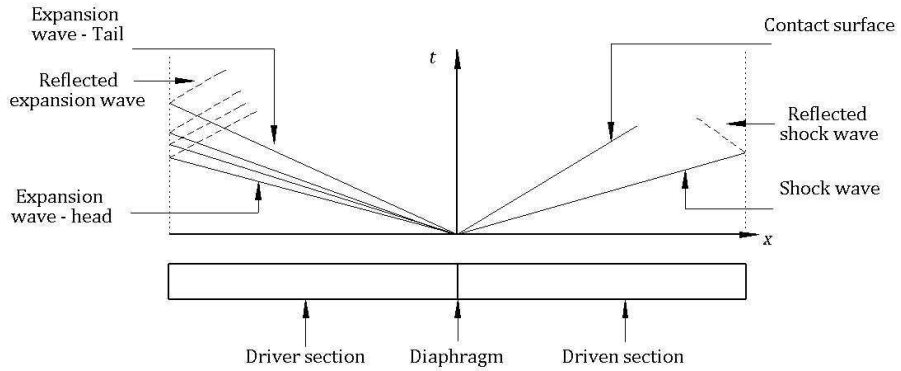


Figure 2.2: Wave diagram describing flow events in a shock tube following diaphragm rupture.

The shock tube events described above can be conveniently summarized using a wave diagram. The wave diagram graphically depicts the propagation of sound waves and particle paths. Both are influenced by the presence of compression and expansion waves and discontinuities in the flow. The discontinuities comprise shock waves and the contact surface. The expansion wave is bounded by a head (leading characteristic) and a tail (trailing characteristic) waves. The change in flow properties through the expansion wave is smooth and isentropic whereas that through a shock wave (coalescence of compression waves) occurs as a discontinuous jump in the flow field and is an irreversible process. Figure 2.2 gives the instantaneous position for a finite duration of time of the wave elements at any location in the shock tube along a single co-ordinate direction.

On the wave diagram, the expansion and compression waves are the characteristics of the non-linear wave equation in one-dimension. An assumption made is that of a centered expansion wave and instantaneous shock wave formation. Practically this does not occur but the assumption is valid for rapid de-pressurization of a vessel (Rudinger [1955]).

2.2.3 Real Flow Effects

Fluid viscosity and viscous effects near the wall tends to attenuate the propagation speed of a shock or expansion wave. The shock wave (which is a coalescence of finite compression waves) can have its motion attenuated by the fluid viscosity in the core flow and the boundary layer along the wall, a similar consideration can be given for an expansion wave. A well designed shock tube will have a hydraulically smooth inner surface to minimize the effect of viscous attenuation upon the shock and expansion waves. A smooth surface also aids to reducing perturbations of various strengths being propagated into regions of subsonic flow.

The diaphragm bursting process would create an unsteady three-dimensional flow pattern since the diaphragm bows under a pressure differential. The results in a component of velocity not directed along the longitudinal axis of the shock tube. This effect was found to develop a system of transverse waves that are known to propagate downstream of the shock tube, (Glass and Patterson [1953]).

2.2.4 The Ideal Gas Assumption

It will be assumed throughout all physical and numerical tests that the ideal gas law remains valid. The energy equation used in the present study was developed using the assumption of a thermally and calorically perfect gas which obeys the ideal gas law. It will be necessary to consider those processes due to the thermodynamic behaviour of the shock and expansion waves which can lead to the ideal gas law being invalid or the gas not being thermally perfect.

A shock wave heats the gas in passing whereas an expansion wave would cool the gas. These two thermodynamic processes are briefly considered with regards the validity of the ideal gas assumption.

For air ($\gamma = 1.4$), at room temperature (≈ 300 K), its liquefaction point is ≈ 82 K (Brown et al. [1996]). At P41 =1000, the region behind the expansion wave would have decreased to $\approx$ 83 K where liquefaction would almost begin. The second aspect concerns the gas dissociation and ionization of gas particles which can occur at 1500 K in air. However the shock heated gas at P41 = 1000 would have attained a temperature of 860 K. Therefore, at P41 = 1000, the thermally perfect and ideal gas assumption remains valid for the shock wave but breaks down for the expansion wave.

For sufficiently strong shocks the temperature rise across the shock can be severe to cause dissociation and ionization of the gas particles ($T_2 = 1500$ K). These are considered as real

gas effects and the value for T_2 is achieved at P41=210 000) for an air filled shock tube initially at $\approx$ 300 K.

The maximum value of P41 considered in the present study was 18 and therefore the assumption for an ideal and thermally perfect gas is valid.

2.3 Unsteady One-Dimensional Wave Motion

A brief, descriptive account is provided of unsteady wave motion in a gaseous medium as occurs in a standard, simple, one-dimensional, shock tube environment. Additional information on this topic can be found in a standard text of compressible flows such as Anderson [2003].

2.3.1 General Behaviour

In this section the general behaviour of a one-dimensional *finite wave* is discussed. A finite wave (non-linear) is a type of wave which propagates through a gaseous medium and creates perturbations in flow properties local to the waves region of influence, where these perturbations are significant in magnitude relative to the medium. The effect of a finite wave results in deformation of the waves shape as the wave travels in a particular spatial direction. The flow field induced by a finite wave is unsteady and therefore, flow properties within the wave depend on a spatial co-ordinate x and time t. i.e. $\rho = \rho(x,t), T = T(x,t), u = u(x,t), P = P(x,t)$. This discussion is restricted to a case where the region into which the finite wave propagates is a quiescent, stagnant gas. Also, in terms of the waves direction of travel, the wave can be either right- or left-running where its motion will be specified relative to an absolute frame of reference.

A wave which induces insignificant changes in density (ρ) within its region of influence, $|\Delta\rho| \ll 0$ and whose shape remains relatively constant during propagation is termed an 'acoustic wave'. This type of wave can be considered a weak finite wave whose perturbations relative to that in the medium of propagation are negligible $\Delta\rho \approx 0$. An assumption of negligible perturbations of an 'acoustic wave' permits linearization of the wave equation that otherwise governs non-linear wave motion. The acoustic wave does not predominantly feature in the present study but its existence is worth noting.

Two aspects are noted: The first is a non-linear wave induces perturbations within a gaseous medium that are local to the wave. These perturbations change the local fluid properties that are significant relative to the medium through which the wave propagates. The other aspect

concerns the waves shape which deforms over time and distance, a property of a non-linear wave..

A finite wave consists of two regions, namely: a *finite-compression wave* and a *finite-expansion wave*. A simple (non-linear) wave has either of these finite wave types. Each will be discussed separately in the subsections to follow.

2.3.2 Finite-Compression Waves

Consider a stationery piston in a long duct of constant cross-sectional area as shown in figure 2.3 where the gas ahead of the piston has uniform flow properties and is stagnant ($u_1 = 0$). If the piston were to undergo a steady acceleration to the *right* until a finite piston velocity has been achieved, a series of *compression* waves, would develop *ahead* of the piston. The compression waves, described by characteristic lines in figure 2.4, would eventually converge and coalesce into a shock wave. The flow field in the presence of a shock wave is governed by the equations for a moving normal shock wave and briefly covered in section 2.4.1.

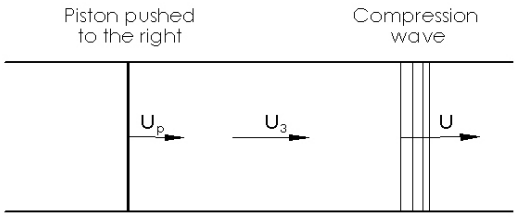


Figure 2.3: Generation of compression waves by piston motion.

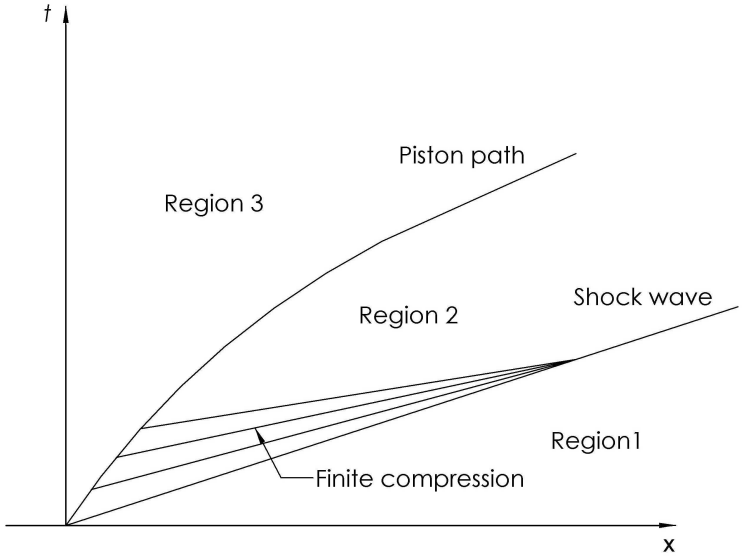


Figure 2.4: Wave diagram to a illustrate finite compression wave.

2.3.3 Finite-Expansion Waves

Now consider the stationary piston in a long duct steadily accelerating to the left until a finite piston velocity has been achieved, as described in the previous section, 2.3.2, for the finite-compression waves. A series of *expansion* waves would develop to the *right* of the piston as illustrated in figure 2.5 and by characteristics in figure 2.6. The expansion wave is bounded by two characteristics termed the *leading* and *trailing* characteristics which continuously *diverge* with time.

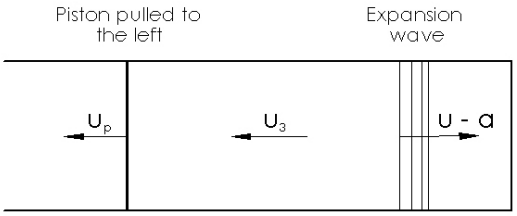


Figure 2.5: Generation of expansion waves by piston motion.

Should the piston be instantaneously accelerated while being withdrawn from the long duct, the expansion wave can be approximated as a centered expansion wave shown in figure 2.6, as assumed to occur in a shock tube following diaphragm rupture. In section 2.4, analytical equations are presented to describe the variation of flow properties: pressure, temperature, velocity and density, through a centered expansion wave.

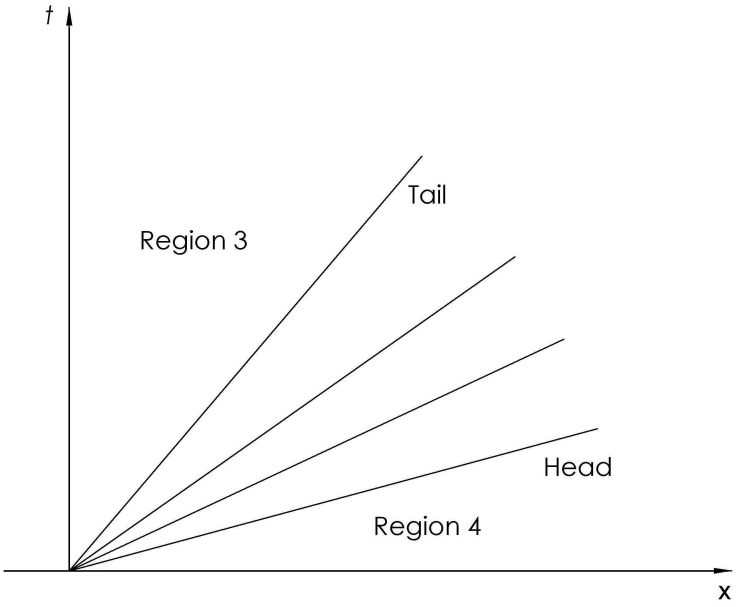


Figure 2.6: Wave diagram to illustrate a finite expansion wave.

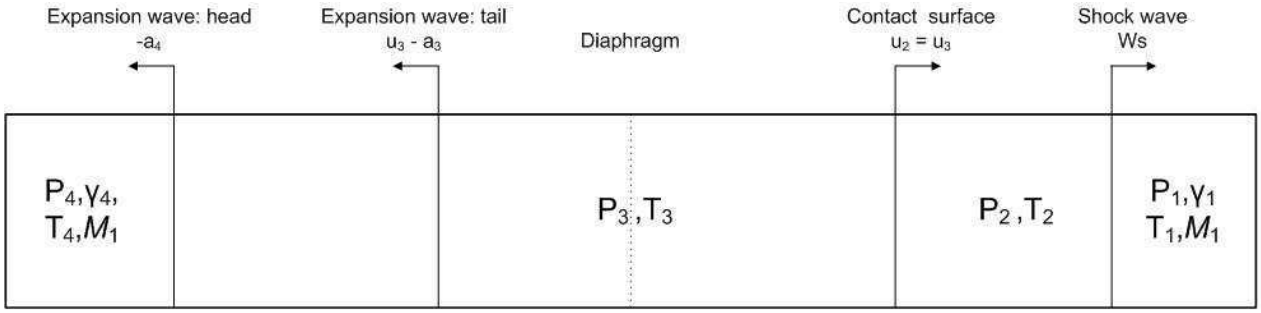


Figure 2.7: Post diaphragm-burst shock tube events with vector notation for the wave elements.

We now consider the induced gas motion within the expansion wave. Such a wave can be represented with infinitely many wave elements between the leading and trailing characteristics. Each element of an expansion wave propagates at a velocity defined by the vector sum of the induced gas motion and the local sound speed the expansion wave propagates at local sound speed defined within the expansion wave. For any point within the wave, the wave velocity is given as u-a, for either a left or right running wave (Anderson [2003]).

2.4 Unsteady One-Dimensional Compressible Flow Equations

A summary of the required equations to analyse flow properties in a simple, standard, shock tube are described. These equations, with appropriate shock tube boundary conditions are combined to arrive at the shock tube relation in section 2.5.

2.4.1 Moving Normal Shock Waves

A shock wave has a finite propagation velocity and is an unsteady phenomena, sonic in the case of sound and supersonic for shock waves; the analysis which follows considers shock wave motion from a moving frame of reference. For a shock wave moving into a quiescent gas where the gas is assumed to be calorically perfect, the shock Mach number is given by equation 2.1. The assumption of a calorically perfect gas allows the use of constant specific heats and the ideal gas law.

$$M_s = \sqrt{\frac{\gamma+1}{2\gamma}\left(\frac{p_2}{p_1}-1\right)+1} \tag{2.1}$$

Refer to figure 2.7. The shock Mach number is defined by the ratio of its propagation speed (W_s) and the sound speed of the gas ahead of the shockwave (a_1). The ratio is then $\frac{W}{a_1}$ and through equation 2.1, the shock velocity can now be specified. The shock velocity is given by equation 2.2.

$$W = a_1\sqrt{\frac{\gamma+1}{2\gamma}\left(\frac{p_2}{p_1}-1\right)+1} \tag{2.2}$$

Equation 2.2 shows the shock velocity is uniquely specified by the pressure ratio across the shock wave P21 and sound speed of the gas ahead of the shock (a_1). The ratio of P21 is termed the shock strength and the importance of obtaining this quantity is reflected in solving the equations that describe the properties for an expansion wave in a shock tube. This will be covered in the next section. Another important parameter influenced by the shock wave is the velocity of the accelerated gas behind the shock (u_p) where the acceleration is assumed to occur instantaneously. The gas velocity behind the shock is given by equation 2.3.

$$u_p = W\left(1-\frac{\rho_1}{\rho_2}\right) \tag{2.3}$$

It is convenient to express the gas velocity in terms of the parameters P21 and a_1. The *Hugoniot* equation which relates change in thermodynamic variables across a normal shock wave and its derivation can be found in a standard text on gas dynamics such as Anderson [2003]. By the assumption of calorically perfect gas it then becomes possible to express the gas velocity in terms of the above parameters, in closed form, by obtaining an expression for the ratio $\frac{\rho_1}{\rho_2}$. Combining the expression for this ratio with equation 2.2 a convenient form for the gas velocity is obtained as:

$$u_p = \frac{a_1}{\gamma}\left(\frac{p_2}{p_1}-1\right)\left(\frac{\frac{2\gamma}{\gamma+1}}{\frac{p_2}{p_1}+\frac{\gamma-1}{\gamma+1}}\right)^{0.5} \tag{2.4}$$

2.4.2 Expansion Waves

This section presents the one-dimensional, unsteady, compressible flow equations which describe flow properties within a centered expansion wave, bounded by the leading and trailing characteristics. These equations are applied in Chapter 3 to develop a variety of plots to explore the behaviour of a centered expansion wave. It was found such plots were not readily available in the literature and were considered as fundamental analysis that may aid further study.

Figure 2.2 illustrates the boundary conditions which were considered for a left running expansion wave, where the gas in region 4 (the driver section of the shock tube), is stagnant $u_4 = 0$. The velocity of the leading characteristic, given by equation 2.5, is then -a_4 and is dependent on the temperature in region 4. Note: the positive direction of motion is taken to the right.

$$a_4 = \sqrt{\gamma R T_4} \tag{2.5}$$

The Method of Characteristics brings forth a Riemann variable that remains constant at any point in a one-dimensional expansion wave (Anderson [2003]). For a left-running expansion wave the Riemann variable is given by equation 2.6.

$$u + \frac{2a}{\gamma - 1} = constant \tag{2.6}$$

Applying equation 2.6, in the general case for a one-dimensional simple expansion wave (left running), gives:

$$u_4 + \frac{2a_4}{\gamma - 1} = constant \tag{2.7}$$

Application of the boundary conditions in region 4, to equation 2.7 and relating the resulting expression to any point with in an expansion wave gives:

$$\frac{a}{a_4} = 1 - \frac{\gamma - 1}{2}\frac{u}{a_4} \tag{2.8}$$

The temperature profile through an expansion wave can be determined with the aid of equation 2.5. Note the profile is parabolic. It will be shown u to be a monotonic linear function through the expansion wave.

$$\frac{T}{T_4} = \left[1 - \frac{\gamma - 1}{2}\frac{u}{a_4}\right]^2 \tag{2.9}$$

For isentropic flow, the following two relations arise between density and temperature, with pressure:

$$\frac{P}{P_4} = \left(\frac{\rho}{\rho_4}\right)^{\gamma} = \left(\frac{T}{T_4}\right)^{\left(\frac{\gamma}{\gamma-1}\right)} \tag{2.10}$$

Expressions for the pressure and density variation within the expansion wave are obtained by combining the isentropic flow relations with equation 2.9. These expressions are given by equations 2.11 and 2.12 respectively. Note the monotonic non-linear nature of these expressions.

$$\frac{P}{P_4} = \left[1 - \frac{\gamma - 1}{2}\frac{u}{a_4}\right]^{\left(\frac{2\gamma}{\gamma-1}\right)} \tag{2.11}$$

$$\frac{\rho}{\rho_4} = \left[1 - \frac{\gamma - 1}{2}\frac{u}{a_4}\right]^{\left(\frac{2}{\gamma-1}\right)} \tag{2.12}$$

The above equations describe the flow properties in an expansion wave and are functions of two variables, namely: a flow property and the local gas velocity. An expression is now required for the velocity profile of the fluid within an expansion wave. In the previous section it was shown the characteristic equation of a left running centered expansion wave is $\frac{dx}{dt} = u$ - a which appears as a straight line through the origin on the wave diagram. This equation represents the actual velocity for the wave element. When integrated along the straight line gives equation 2.13. An expression for the local gas velocity within an expansion wave was obtained combining equations 2.7 and 2.13. The result is given by equation 2.14.

$$x = (u - a)\, t \tag{2.13}$$

$$u = \frac{2}{\gamma + 1}\left(a_4 + \frac{x}{t}\right) \tag{2.14}$$

In turn equation 2.14 is a function of two variables, namely a spatial co-ordinate and time and apples to a left-running expansion wave. A right running expansion wave would have $\frac{dx}{dt}$ $= u + a$. The region into which the expansion wave propagates (region 4) must be quiescent and stagnant. If the gas is not stagnant in region 4 then the gas velocity must be accounted for in equation 2.7. We now quantify the limits represented by the leading and trailing characteristics.

It is important to note that equation 2.14 is valid for a range of values $\frac{x}{t}$ defined by the width of the expansion wave. Since the expansion wave produces an unsteady flow, the width is dynamic and broadens out with time. The boundary conditions are then given as:

$$\text{-}a_4 \leq \frac{x}{t} \leq u_3 - a_3 \tag{2.15}$$

Behind the trailing characteristic the flow state is uniform and steady. In a shock tube, this effect is maintained for as long as reflected waves do not arrive at the rear of the trailing characteristic.

2.5 The Shock Tube Relation

Consider figure 2.7, in section 2.4 which illustrates the propagation of wave elements in the shock tube and their vector notation. The driver region of the shock tube is positively pressurized and the driven section left open to atmosphere. The gas types in these two sections are identical having the same specific heat ratio γ and molecular weight ratio M. The pressure ratio across the driver and driven section is termed the *diaphragm pressure ratio*.

The gas velocity and static pressure across the contact surface is identical. This gives rise to the following boundary conditions for regions 2 and 3: $u_2 = u_3$ and $P_2 = P_3$. Application of equations 2.4, 2.11 and the boundary conditions stated above yields the following expression between the diaphragm pressure ratio and shock pressure ratio. The derivation can be found in a standard textbook on gas dynamics such as Anderson [2003].

$$\frac{P_4}{P_1} = \frac{P_2}{P_1}\left[1 - \frac{(\gamma_4 - 1)\left(\frac{a_1}{a_4}\right)\left(\frac{P_2}{P_1} - 1\right)}{\sqrt{2\gamma_1\left[2\gamma_1 + (\gamma_1 + 1)\left(\frac{P_2}{P_1} - 1\right)\right.}}\right]^{\frac{-2\gamma_4}{\gamma_4 - 1}} \tag{2.16}$$

Equation 2.16 gives diaphragm pressure ratio as an implicit function of shock strength P21. The shock strength parameterizes the equations which describe the effect of a moving normal shock wave. Since P41 is known from the initial conditions in the shock tube, the problem reduces to one of obtaining a value for the shock strength such that equation 2.16 is mathematically true i.e. the left side equals the right side. A solution technique for this equation is discussed in Chapter 3.

The importance of obtaining P21 is reflected in the manner through which the expansion wave strength P34 is derived. This term can be re-written as follows and accounting for the pressure boundary conditions between regions 2 and 3:

$$\left(\frac{p_3}{p_4}\right) = \frac{(p_3/p_1)}{(p_4/p_1)} \tag{2.17}$$

The evaluation of the density and temperature behind the expansion wave is determined through the isentropic relations given by equation 2.10, repeated here but applied across regions 3 and 4:

$$\frac{P_3}{P_4} = \left(\frac{\rho_3}{\rho_4}\right)^{\gamma} = \left(\frac{T_3}{T_4}\right)^{\left(\frac{\gamma}{\gamma-1}\right)} \tag{2.18}$$

It is now evident of the importance to obtain the shock strength as this quantity permits the solution of all flow properties in regions 2 and 3 of the shock tube. Consider the term $(\frac{a_1}{a_4})$ in equation 2.16, if the temperature in regions 1 and 4 corresponding to the driven and driver sections respectively are equal then this term is 1.

3 Preliminary Information

3.1 Introduction

It is useful to explore the fundamental behaviour of an unsteady, one-dimensional, centred expansion wave before proceeding to the case in two-dimensions. This chapter describes a solution to the shock tube relation, which required a numerical approach. Other topics considered was: dynamics of a one-dimensional expansion wave including the influence of the independent parameters P41 and D on the waves width, Mach ≥ 1 condition through the expansion wave, self-similar behaviour of the expansion wave, and the evaluation of the flow Reynolds number behind the trailing characteristic.

The following figure 3.1, introduced in Chapter 2, was referred to in later sections within this chapter. The reader should consult this figure when required.

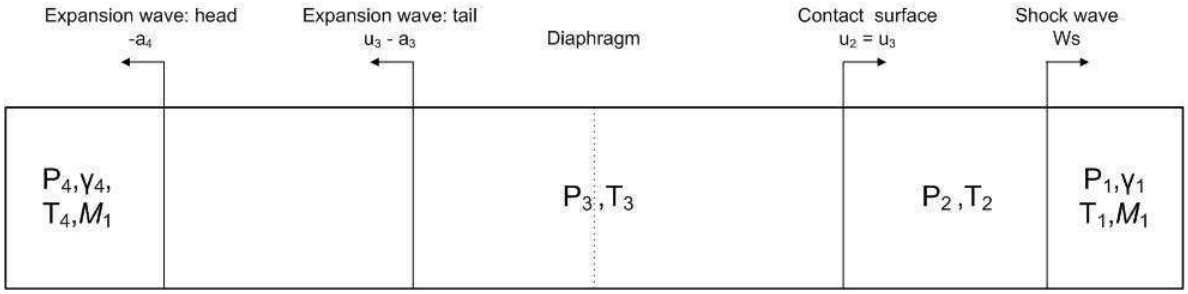


Figure 3.1: Post diaphragm-burst shock tube events with vector notation for the wave elements.

3.2 Solution to the Shock Tube Relation

To solve the analytical equations which describe the flow properties within a one-dimensional expansion wave, it was necessary to solve for the shock strength (P21) expressed implicitly

in equation 2.16. This equation, including those for the expansion and shock waves were formally introduced in chapter 2.

The importance of obtaining this ratio, P21 from the known information of: the diaphragm pressure ratio (P41), the gas molecular weight (M), the specific heat ratio (γ) and the temperature (T) for the driver and driven sections, was discussed in chapter 2. A solution to this equation returned the shock strength for a given diaphragm pressure ratio.

Refer to the shock tube wave diagram shown in figure 3.1. This figure illustrates the typical post diaphragm-burst events in the shock tube. P21 appeared implicit in equation 2.16 and was required to solve for flow properties behind the shock heated gas and to determine the expansion wave strength P34. A numerical scheme was formulated that required equation 2.16 to be expressed in the following form:

$$\varepsilon = \frac{P_2}{P_1}\left[-\frac{(\gamma_4-1)\left(\frac{a_1}{a_4}\right)\left(\frac{P_2}{P_1}-1\right)}{\sqrt{2\gamma_1\left[2\gamma_1+(\gamma_1+1)\left(\frac{P_2}{P_1}-1\right)\right.}}\right]^{\frac{-2\gamma_4}{\gamma_4-1}} - \frac{P_4}{P_1} \tag{3.1}$$

The rationale behind the numerical scheme will now be covered: Let the shock strength (P21) be referred to as γ_{shock}. The primary condition was a simple mathematical concept which required the left side of this equation, which is exact and known, to almost equate to the right side, that will be approximated. The value of ϵ in 3.1 refers to the approximation error in the numerical method between the exact and approximate values. A flow chart of the numerical method appears in Appendix E and the code for the numerical scheme is included in the digital appendix, should the reader wish to modify or review working details of this code. A brief operational review is now discussed. The program requires identical values for the specific heat ratio and molecular gas constant, also the initial gas state must be quiescent and stagnant. The input data provided by the user was then:

- The diaphragm pressure ratio P41,
- The initial temperature in the driver and driven sections of the shock tube (T4 and T1 respectively),
- The specific heat ratio of the gas (γ),
- The molecular gas constant (M) and,
- An acceptable level of error, expressed as a percentage, between the ratio of the exact and approximate value of the pressure rise across the shock (γ_{shock}).

It was necessary to perform a verification check on the performance of this code as the outputs were extensively applied for the present chapter. Data for initial shock tube conditions, prior to diaphragm rupture was obtained from Skews [1961]. This data, obtained through measurement, was: The (initial) diaphragm pressure ratio (P41), initial driver and driven temperatures (T1 and T2), and the shock wave velocity. The parameters, P41, T1, and T2 were inputs for this code, and the output to serve as a verfication check was the shock wave velocity. Favourable agreement was obtained where these results are tabulated in Appendix A.

Once the value of γ_{shock} was obtained and the strength of the expansion (P34) wave established, the flow properties through the expansion wave and in regions 3 and 2 of figure 3.1, could then be computed using the unsteady compressible flow equations presented in chapter 2.

3.3 Basic One Dimensional Expansion Wave Dynamics

This section develops certain key plots to illustrate the fundamental behaviour of the one-dimensional expansion wave. Other aspects considered the waves physical motion and briefly cover the variables influencing the propagation speed of the expansion wave.

3.3.1 Fundamental Behaviour

In chapter 2, it was shown for air, that the diaphragm pressure ratio can be of magnitude (P41 =1000) to induce real gas effects leading to a breakdown of the assumptions that underlie the ideal gas equation. On this basis it would not be useful to consider an infinitely large diaphragm pressure ratio but rather to observe the trend that would arise were P41 made sufficiently large. Two curves illustrate the variation of P41 with the pressure drop across the expansion wave (P34), and with the pressure rise across the shock wave (P21), in figure 3.2.

3.3.1.1 Pressure, Temperature, and Density Plots

From figure 3.2 the following was observed: the shock strength steadily rose with increasing diaphragm pressure ratio (P41) whereas the expansion wave strength (P34) tended towards zero. This meant the pressure drop across the expansion wave decreased with the diaphragm pressure ratio.

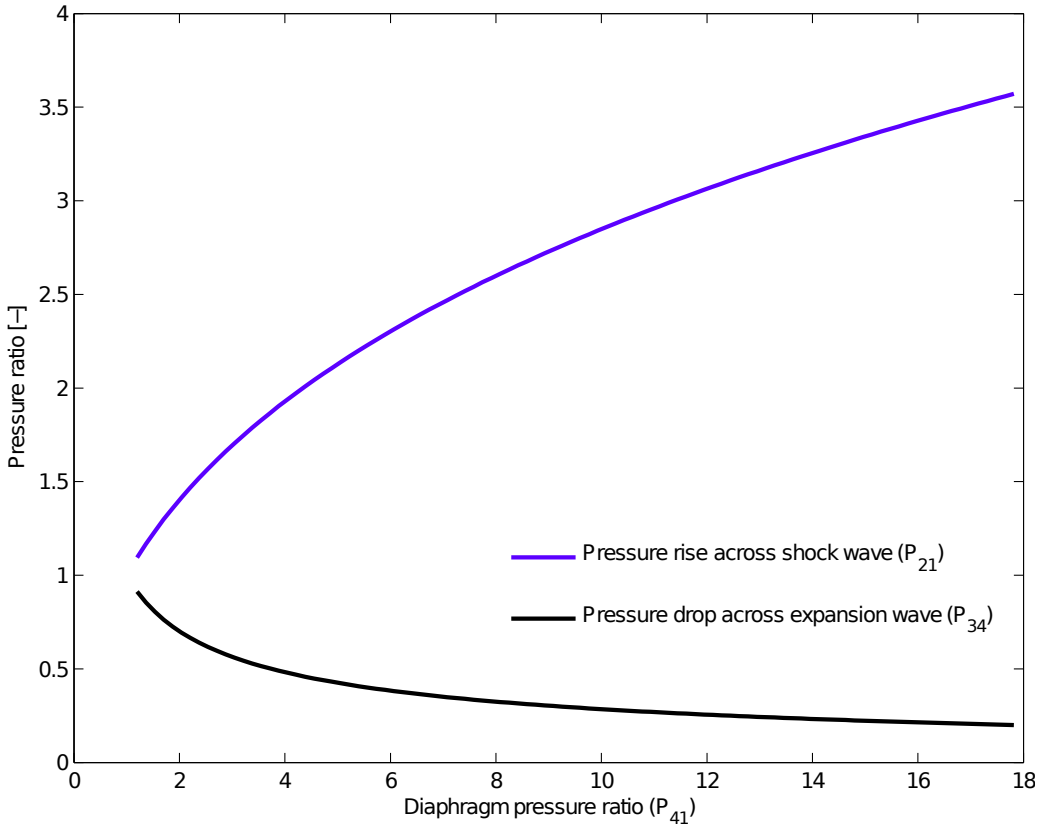


Figure 3.2: Variation of P34 and P21 with P41.

We now consider plots of temperature and density ratios across the expansion wave, (T34) and (ρ34) respectively. The independent variable, P41, was non-dimensionalised by the static pressure in the driven section. The dependent variables, (T34 and ρ34) were non-dimensionalised by region 4 of the shock tube, where this region is illustrated in figure 3.1 and is shown in figure 3.3.

Consider figure 3.4 which shows the variation of P43 with P41. This figure allowed for a convenient approach to obtain P34 by its inverse, 1/P43, for a desired diaphragm pressure ratio (P41). The inverse of the expansion wave strength may be used to read-off density and temperature ratios across the expansion wave in figure 3.3 whereas an alternative method would require the evaluation of the shock pressure ratio (P21) given P41.

3.3.1.2 Velocity and Mach Number Plots

Figure 3.5, illustrates the variation of the various velocities associated with a *left-running* expansion wave. The blue curve represents the flow velocity in region 3 of the shock tube, as shown in figure 3.1 and the red curve represents the propagation speed of the trailing

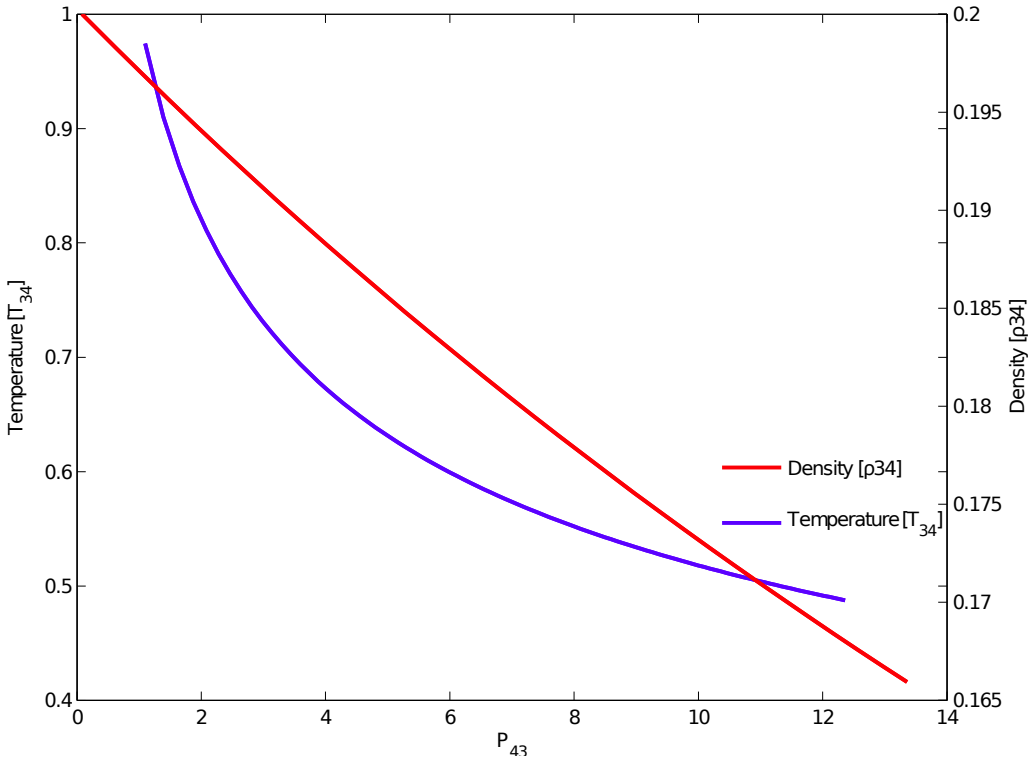


Figure 3.3: Variation of T34 and ρ34 with P41. (P41 ranged between 1-60 bar, P1 = 0.834 bar and T1 = 300 K.)

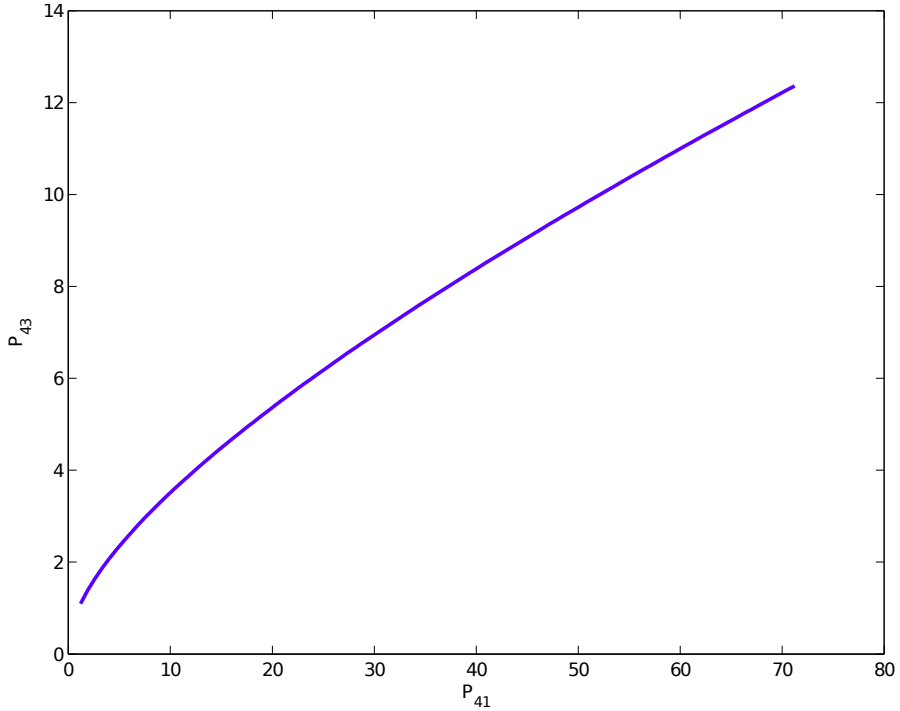


Figure 3.4: Variation of P43 with P41. (P41 ranged between 1-60 bar, P1 = 0.834 bar and T1 = 300 K.)

characteristic. A similar plot which considers the Mach number variations appears in figure 3.6. These figures pertain to a left-running centred one-dimensional expansion wave.

A portion of the red curve, in figure 3.5 attained negative values for P41 < 10.4 which occurred at the intersection of this curve with the zero axis. The value of this intersection point, on the horizontal axis coincides with that obtained by the intersection of the flow velocity curve (blue) and the local sound velocity curve (black). This result means, that the flow velocity at P41 $= 10.4$ is equivalent to the local sound velocity at the trailing characteristic. The calculation of this result appears in section 3.3.2.1.

The flow velocity for u_3 - $a_3 < 0$, in figure 3.5, represents subsonic flow through the expansion wave where, physically, both the leading and trailing characteristics propagate towards the left. However, for $u_3 > 0$, in this figure, the leading and trailing characteristics propagate in opposite directions. The reader may refer to table 3.1 in subsection 3.3.2.1. A similar statement can be made for the Mach number variation in figure 3.6.

Of some interest would be the intersection of the propagation speed of the trailing characteristic and the local sound velocity curves. From the Mach number plot in figure 3.6 this indicated that a wave velocity of Mach 1 occurred for supersonic flow in region 3 at P41 $=$ 56, where this result was calculated in section 3.3.2.2.

3.3.2 Supersonic Flow Conditions

We now explore the conditions for sonic and supersonic flow behind the trailing characteristic for a one-dimensional expansion wave in section 3.3.2.1, and similarly for the wave speed (trailing characteristic) in section 3.3.2.2. We do not consider the leading characteristic since, for various values of P41, the driver temperature is assumed uniform and constant, therefore the velocity of the leading characteristic is constant ($\sqrt{\gamma R T_4}$)

3.3.2.1 Acceleration of flow to Mach $\geq$ 1, through the expansion wave

Consider a left running expansion wave propagating into a quiescent, stagnant gas. A particle traversed by the leading characteristic will experience smooth acceleration until the particle has reached the trailing characteristic. Also, there occurs a reduction in temperature within the expansion wave, therefore the flow Mach number would continually raise between the leading and trailing characteristics. Sonic and supersonic flow is possible at some location within the expansion waves. The flow Mach number affects the propagation behaviour of

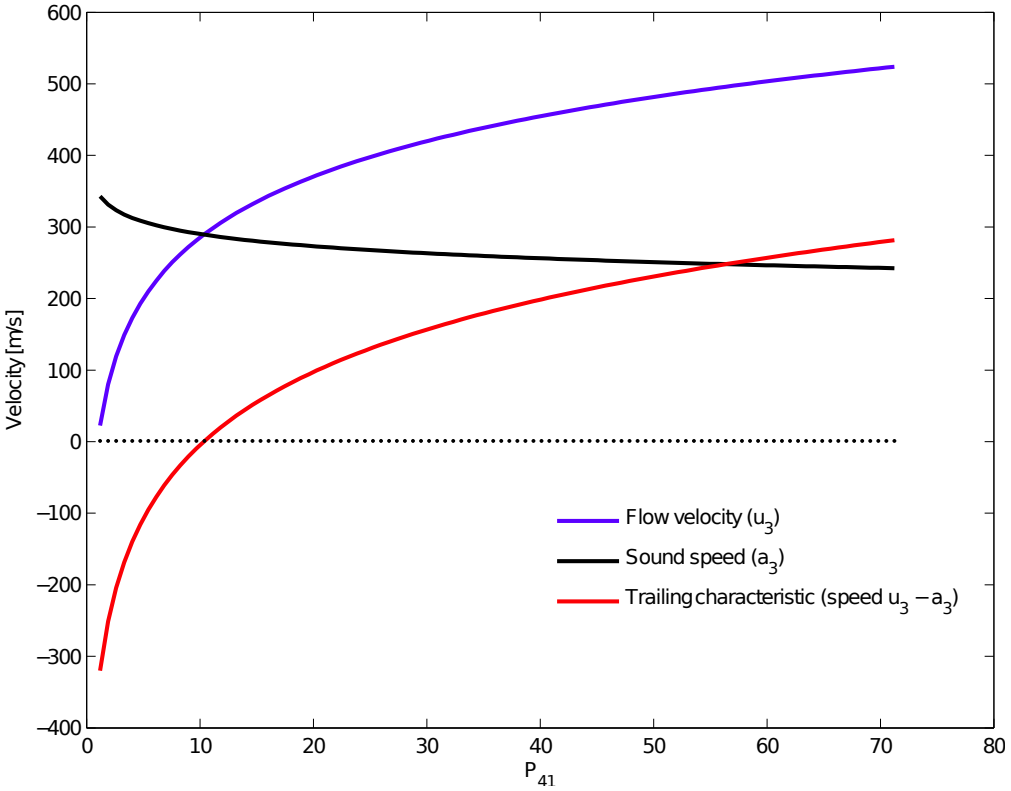


Figure 3.5: Variation of the flow velocity, sound speed and propagation speed of the trailing characteristic, at region 3, with P41.

the expansion wave and is summarized in Table 3.1. (The left arrow head indicates wave propagation to the *left* and similarly the right arrow head for wave propagation to the *right*)

Mach number	**Leading Characteristic**	**Trailing Characteristic**
< 1	$\leftarrow$	$\leftarrow$
$= 1$	$\leftarrow$	0
> 1	$\leftarrow$	$\rightarrow$

Table 3.1: Directional behaviour of a left running expansion wave with Mach number.

Assuming the expansion wave occurs in a shock tube of constant cross-sectional area and without any reflection phenomena, then the region between the trailing characteristic and contact surface will be of uniform flow. Refer to figure 3.1. It would be advantageous to establish a minimum diaphragm pressure ratio which would establish sonic flow at the trailing characteristic. This will now be addressed and the thermodynamic variables were fixed as follows: Constant and uniform temperature in the driver and driven sections at 300 K and ambient pressure of 83400 kPa in the driven section.

For sonic flow between the trailing characteristic of the expansion wave and contact surface (region 3 of the shock tube), the following boundary condition is implied for the flow velocity:

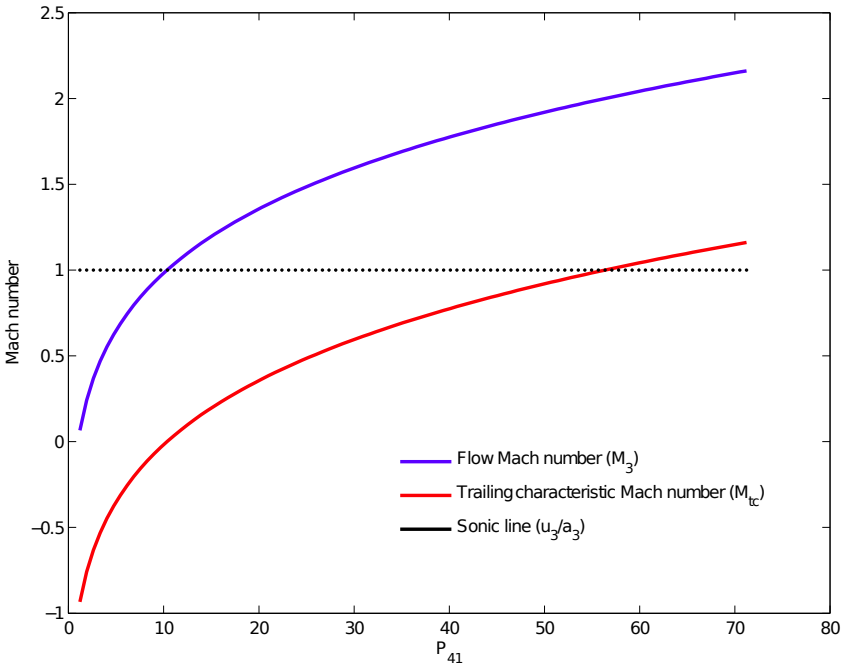


Figure 3.6: Variation of the flow and trailing characteristic Mach numbers at region 3, with P41.

$$u_3 = a_3 \equiv M_{f3} = 1$$

The above boundary condition when substituted for u in equation 2.11 allowed for the pressure ratio across the expansion wave to be established as:

$$\frac{P_3}{P_4} = \left[1 - \frac{\gamma - 1}{2}\left(\frac{a_3}{a_4}\right)\right]^{\left(\frac{2\gamma}{\gamma-1}\right)} \tag{3.2}$$

An expression for the ratio of sound speed in regions 3 and 4 which appears in equation 3.2 is now required. Consider equation 2.8 for sound speed through an expansion wave with the above boundary condition for sonic flow where the resulting equation allows for an explicit expression of $\frac{a_3}{a_4}$

$$\frac{a_3}{a_4} = 1 - \frac{\gamma - 1}{2}\left(\frac{a_3}{a_4}\right) \equiv \frac{a_3}{a_4} = \left(1 + \frac{\gamma - 1}{2}\right)^{-1} \tag{3.3}$$

Combining equations 3.2 and 3.3, and simplifying:

$$\frac{P_3}{P_4} = \left(\frac{2}{\gamma + 1}\right)^{\frac{2\gamma}{\gamma-1}} \equiv P_3 = k_1 P_4 \tag{3.4}$$

where,

$k_1 = \left(\frac{2}{\gamma+1}\right)^{\frac{2\gamma}{\gamma-1}}$

It was then possible to develop a methodology for calculating the diaphragm pressure ratio for sonic conditions between the trailing characteristic and contact surface (using the above results). The shock tube relation was required to solve for the diaphragm pressure ratio where sonic flow exists at the trailing characteristic and which required approximation, similar to that described in Section 3.2: *Solution to the shock tube relation.* Since the pressure in regions 2 and 3 of the shock tube are equal, the second boundary condition is $P_3 = P_2$. Incorporating this condition with equation 3.4 gives: $P_2 = k_1\ P_4$. Combining this result with the shock tube relation, equation 2.16 gives the following final expression:

$$\frac{P_4}{P_1} = k_1 \frac{P_4}{P_1} \left\{ 1 - \frac{(\gamma_4 - 1)\left(\frac{a_1}{a_4}\right)\left(k_1 \frac{P_4}{P_1} - 1\right)}{\sqrt{2\gamma_1\left[2\gamma_1 + (\gamma_1 + 1)\left(k_1 \frac{P_4}{P_1} - 1\right)\right]}} \right]^{\frac{-2\gamma_4}{\gamma_4 - 1}} \tag{3.5}$$

Let the term in the curly brackets be referred to by α, for the approximation method the following form of equation 3.5 was preferred: $1 \approx k\,\alpha$. The methodology followed was identical to that for the approximated shock tube relation, equation 3.1.

3.3.2.2 Mach $\geq$ 1 for the trailing characteristic

Consider the propagation velocity of the trailing characteristic (wave speed) which depends on u_3 - a_3 in region 3 - figure 3.1. For identical conditions in table (above section), the minimum diaphragm pressure ratio (P41) was established for the trailing characteristic to achieve Mach 1. The required boundary condition was then:

$$M_T = \frac{u_3 - a_3}{a_3} = 1 \equiv u_3 = 2a_3 \tag{3.6}$$

A similar analysis was performed for section 3.3.2.1. The required pressure ratio across the expansion wave to achieve Mach 1 for the trailing characteristic is then:

$$\frac{P_3}{P_4} = \left(\frac{1}{\gamma}\right)^{\frac{2\gamma}{\gamma-1}} \equiv P_3 = k_2 P_4 \tag{3.7}$$

where,

$$k_2 = \left(\frac{1}{\gamma}\right)^{\frac{2\gamma}{\gamma-1}}$$

Equation 3.5 was used to evaluate the diaphragm pressure ratio where the methodolgy was identical to that presented in section 3.3.2.1. However, equation 3.7 was required and k_1 must be substituted for k_2.

3.3.3 Dynamic Motion of the Expansion Wave

Consider the instantaneous motion of the expansion wave following diaphragm rupture such as that illustrated in figure 3.1 where the expansion wave would have a finite width, bounded by the leading and trailing characteristics. Also, the flow through the expansion wave is subsonic ($M_f < 0$). In this figure, the leading characteristic propagates at sound speed defined by the temperature in region 4, namely a_4. The trailing characteristic propagates at a velocity defined as u_3 - a_3. Since these velocities are assumed constant with time, the distance covered by the leading characteristic is simply $s_L = (a_4) \times t_1$ and similarly for the trailing characteristic $s_T = (u_3 - a_3) \times t_1$. The expansion wave width (S_w) is then defined by the difference between s_L and s_T, simply written as $S_w = \mid s_L - s_T \mid$. We now consider when ($M_f \geq 0$).

If the flow Mach number (M_f) is supersonic then $S_T < 0$ and S_w evaluates to the sum of S_L and S_T i.e. the leading characteristic travels left-ward and the trailing characteristic travels right-ward on the wave diagram. If M_f is sonic then $S_T = 0$ and the trailing characteristic remains stationery at the origin on the wave diagram. The expansion wave width is then defined by the position of the leading characteristic only relative to the origin of the wave, for $M_f = 1$.

For constant initial shock tube conditions where the diaphragm pressure ratio (P41) is varied, the the expansion wave width is purely a function of P41. Figure 3.7 illustrates the variation of the expansion wave width with P41 against non-dimensional time. The time variable, for this figure, was non-dimensionalized by the maximum propagation time for the expansion wave and was arbitrarily set at 800 μs. It was interesting to note, self-similar behaviour arose for these plots when the independent axis (the expansion wave width in this figure) was non-dimensionalised by each curves respective *maximum width*.

From figure 3.7 the expansion waves width was found to increase linearly with time for various values of P41. This result was expected since the governing equations for propagation speed and distance of the expansion wave, are linear functions. The gradient of the linear curves in this figure was observed to steepen as P41 was increased, however this occurred at a

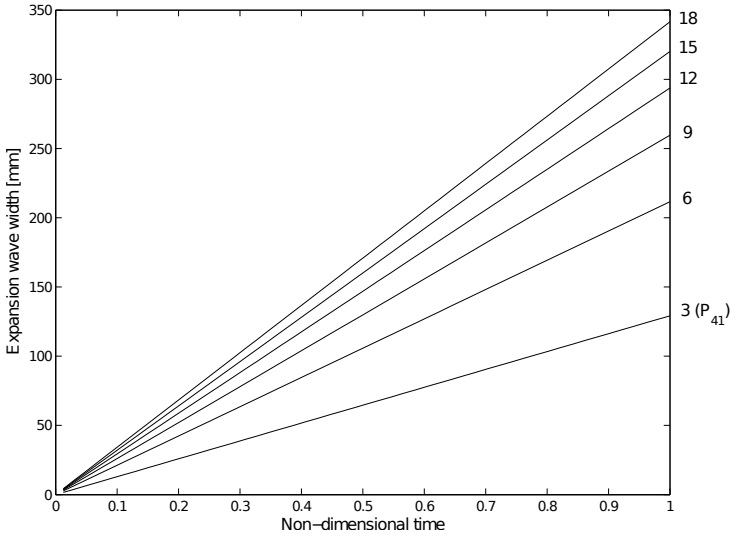


Figure 3.7: Variation of expansion wave width with P41 against non-dimensional time for a one-dimensional expansion wave. Maximum propagation time considered was 800 μs.

decreasing rate. It was concluded earlier in this subsection, that the expansion waves width was a function of P41.

3.3.4 Parameters Influencing the Propagation Speed of an Expansion Wave

This section, is intended to aid the development of a new, revised shock tube, advised for further study in expansion wave behaviour (diffraction, reflection etc). Consider a shock tube where the initial state of the gas in the shock tube's driver and driven section's is quiescent and stagnant. Fpr a left-running expansion depicted in figure 3.1, the velocity of the leading characteristic is W_L = -a_4 and that for the trailing characteristic is, W_T = u_3 - a_3.To increase the expansion waves propagation speed, to develop a narrow-width wave, the following requirements arise: maximize a_4 and minimize the difference between u_3 and a_3. The former requirement addresses the speed of the leading characteristic and the latter that of the trailing characteristic.

The sound speeds a_4 and a_3 depend on the gas type (M_4,γ_4) in the driver section and the respective temperatures (T_4, T_3) in the regions they occur; namely region 4 and 3 respectively in figure 3.1 . T_3 depends on the strength of the expansion wave (P34). Also u_3 is equivalent to u_2 which is the velocity of the shock heated gas therefore we expect the driven gas (M_1,γ_1 and its initial state P_1, T_1) to influence the propagation speed of the trailing characteristic.

In summary the following independent parameters maybe considered to meet the above conditions M_1,γ_1,P_1, T_1 and M_4,γ_4,P_3, T_4. Further analysis may be required which would make for a good fourth year research project.

3.4 The Reynolds Number

It may be useful to have a measure of the flow Reynolds number for the flow induced by an expansion wave and this is briefly considered. Unlike a shock wave whose thickness covers a width of a few mean molecular free paths, the expansion wave has a variable width. In a shock tube this width depends on the initial thermodynamic states of the driver and driven gases and the gas type. It then seems logical to consider the Reynolds number for the flow between the trailing characteristic and the contact surface since, for an instantaneous position, this is a region of steady and uniform flow in absence of wave reflection. The Reynolds numbers are given on a unit length basis and are computed for a range of diaphragm pressure ratios where the objective was to obtain an order of magnitude comparison between these ratios. The equation for the Reynolds number was then written as:

$$\frac{R_e}{D} = \frac{\rho_3 u_3}{\mu_3} \tag{3.8}$$

Since gas viscosity (μ_3) increases with temperature, the fluid viscosity was computed by the Sutherland Law, which is given by equation 3.9.

$$\mu = \mu_{ref} \frac{T}{T_{ref}}^{3/2} \left(\frac{T_{ref} + S}{T + S} \right) \tag{3.9}$$

Table 3.2 presents the results of equation 3.8 for a range of (P41) values.

Pressure ratio	Unit Reynolds number
3	1.94E+07
6	5.26E+07
9	8.65E+07
12	1.20E+08
15	1.54E+08

Table 3.2: Reynolds number per unit length behind the expansion wave

The range of diaphragm pressure ratios in Table 3.2 represents practical values that may be encountered in practice. The unit Reynolds number is valid for region 3 in the shock tube of figure 3.1. Based on the order of magnitude of the unit Reynolds number, the gas in region 3 can be used in experimentation as a test-gas for practical applications.

4 Experimental Method

4.1 Introduction

The flow field generated in a shock tube by the diffraction of an unsteady expansion wave around a two-dimensional sharp corner was investigated using computational and experimental methods. The computational method is treated in Chapter 5. The experimentation was performed using an existing rig in the Mechanical Engineering Laboratory at the University of the Witwatersrand. Certain modifications were required to meet objectives for the present study which are described in the next section. In this chapter, an account is given on the shock tube, the facility and instrumentation description, performance of the experimental facility and pertinent procedure and precautions for the present study.

4.2 Experimental Objectives

The primary experimental objective was to accumulate a set of qualitative data which explored the behaviour of the flow field by diffraction of an unsteady expansion wave over a 90° corner, for various values of initial diaphragm pressure ratio (P41). This objective was necessary since hardly any experiment data, on this particular diffraction process, was found to exist in the literature. The second objective was to provide some means to validate the simulation of this diffraction process where a commercial flow simulation package was used. Values of pressure data for the driver section are listed in table 4.1, the driven section was at nominal atmospheric conditions of 83400 KPa and temperature of 288 K.

The parameter space for the experimentation involved the variation of a single parameter (P41) due to constraints of the rig and is discussed in the next section, 4.3.2. The experiments by simulation, covered in Chapter 5, varied two parameters P41 and D where these two parameters were visually described in section 1.2 and repeated for convinience in figure 4.1.

Table 4.1: Pressure data for experimentation in the driver section

Gauge pressure	Absolute diaphragm pressure ratio
bar	**-**
1.8	3.2
3.6	5.6
4.6	6.5
5.6	7.7

In this section, a brief account is given for the acquired (initial) shock tube and the modified version is described in some detail. The instrumentation and data acquisition systems were of standard set-up and operation. Some recommendations were proposed to further improve upon the design of this shock tube for the study of expansion wave diffraction/reflection. The experimental facility was non-existent at the outset of the present study and was commissioned using some temporary solutions. The major operational hazards are discussed should the study be furthered. The repeatability of the experimental results are analysed in a qualitative fashion.

4.3 The Initial Shock Tube

This shock tube was specially designed to visualize expansion wave diffraction and, as such its design was unconventional compared to a traditional shock tube. Consider figure 4.1, where upon diaphragm rupture an expansion wave would propagate upstream into the driver section and a shock wave would propagate downstream into the driven section. In a typical shock tube, for, e.g. shock diffraction studies, a viewing port and test pieces in located in the driven section whereas for expansion wave diffraction studies, these elements must be located in the driver section.

4.3.1 Rig Description

The initial shock tube consisted of two chambers separated by a gas-tight diaphragm with the driven section exhausting to atmosphere. An exploded CAD view of the initial shock tube appears in in figure 4.2. The shock tube was built from three sections of which two were cantilevered. These sections were: the driver and driven sections and an intermediate

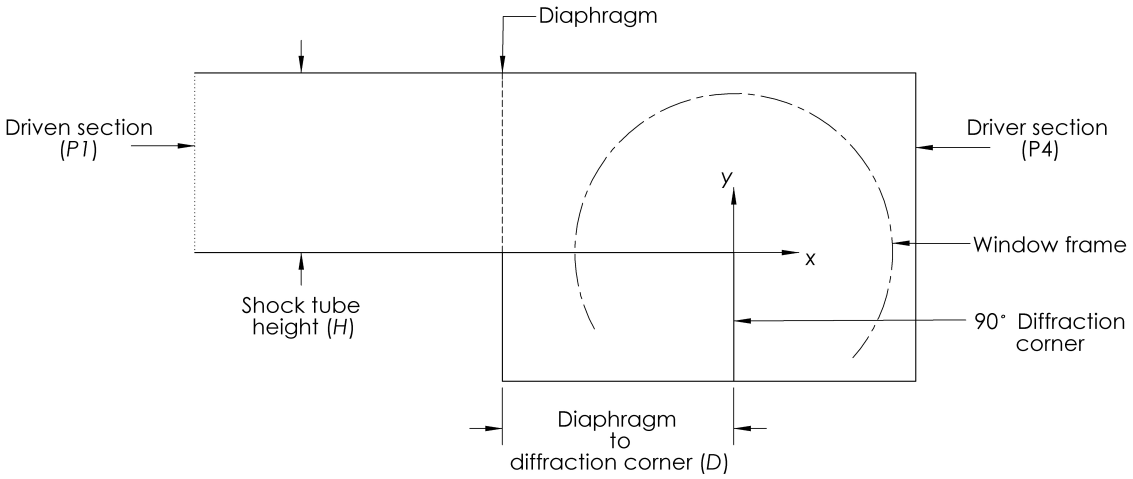


Figure 4.1: Schematic of the shock tube to illustrate the independent parameters.

section. The test piece (diffraction corner) was located in the driver section and the pressure transducers located on opposing sides at the diaphragm location. The diaphragm was positioned between the intermediate and driver sections. Fastening of these three components to clamp the diaphragm into position was performed using bolts, whose paths are identified in this figure.

The driver and driven sections were 450 mm and 160 mm in length, respectively. The flow cross section at the diaphragm position was 90 mm in height and remained constant up to the diffraction corner were this corner had a vertical depth of 60 mm for the side opening into the driver section. The channel width for the shock tube was constant at 40 mm.

The function for the intermediate section was to fasten the driver and driven sections through a total of six M8 bolts. Diaphragm replacement required repetitive removal and fastening of these bolts. This led to unnecessarily long inter-experiment times that could be reduced. The bolt removal and fastening process, coupled with no vertical support structure for the cantilevered components created an operational hazard for the experimenter and/or nearby persons.

4.3.2 Rig Constraints

The constraints of the initial rig were: 1) a maximum gauge pressure of 700 kPa for the driver section, 2) a fixed value (of 103 mm) for the diaphragm position, and 3) a limited, test-time for an experiment until rig dependent effects occur, governed by the geometry of

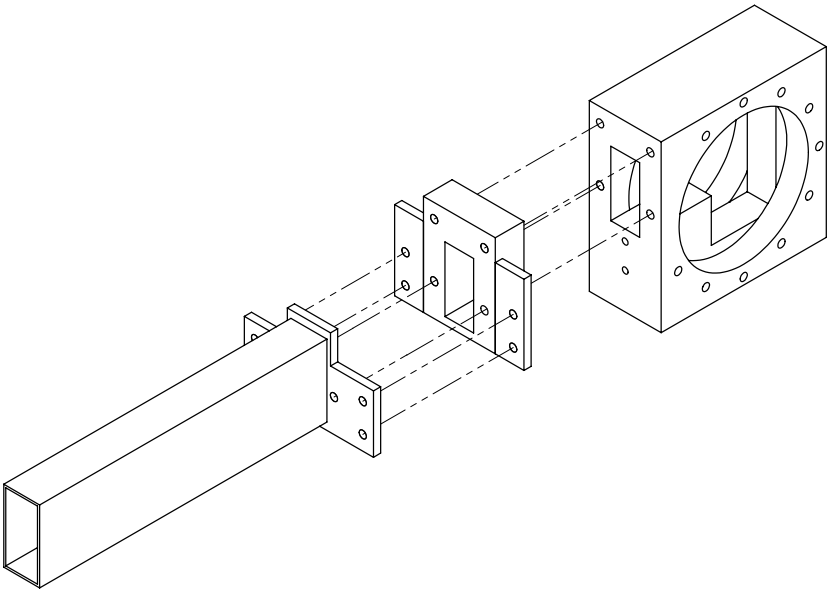


Figure 4.2: Exploded isometric view of the initial shock tube.

the shock tube. Should the diaphragm position be varied, the desired values would fall within an arbitrary range of 0-70 mm from the diffraction corner. This was not possible based on the construction of the driver section and was explored with simulation.

The following issues were raised with regards to the initial design of the specially developed shock tube:

1. The distance over which the (primary) expansion wave travelled up to the diffraction corner was considered too long at D=103 mm. It was shown in chapter 3, section 3.3.3 that the position of the diaphragm from the 90° corner would influence the width of the incident expansion wave prior to diffraction. Therefore the diaphragm was to be located as close as possible to the 90° corner.

2. The intermediate section was eliminated. This required an immediate re-design of the flange on the driven section for direct fastening to the driver section.

3. Suitable fastening methods between the driver and driven sections were necessary. These methods had to be safe, fast and reliable, failure of which may lead to an operational hazard.

4. The existing bolt region to fasten the cantilevered section to the driver section was deemed insufficient to affect a suitable clamping load under a positive pressure differential across the diaphragm. Also, from Budynas and Nisbett [2008] the bolt spacing

between consecutive bolts with regards principles of flange design was found inappropriate. The new flange had to provide adequate clamping load and account for suitable bolt spacing between consecutive bolts, at the maximum gauge pressure in the driver section.

5. Gas leakage was detected at a number of locations at the driver section and location of the diaphragm. It was required to minimize or eliminate these air leaks such that the pressure in the driver section remained at a fairly constant value prior to diaphragm rupture.

6. Machining was required for provision to install additional pressure transducers in the driver section.

The aforementioned points identified the necessary modifications to the initial shock tube whilst adhering to the constraints as previously described to best meet the project's experimental objectives. To change the constraints in a manner that favoured the experimentation, a re-design and manufacture of the rig would be required. Time and costing considerations did not allow for this and the modification approach was adopted instead.

4.4 The Modified Shock Tube

A brief discussion on how the initial shock tube was modified, to best meet the project objectives, is outlined below, based on the modification requirements listed in the previous section.

Diaphragm position Reducing this distance between the diaphragm position and the diffraction corner (D) was accomplished by boring down 20 mm of the driver sections left face. Further boring would lead to insufficient material thickness of < 5 mm on the left face of the driver section. Reducing the length of the test-piece was not advised due to interference by the circular window frame for visualization of the flow field at the diffraction corner. The value of D was reduced to 83 mm which was, practically, the minimum value possible.

Flange re-design and manufacture The new flange was based on the required spacing between bolts and to ensure sufficient clamping area was present in the vicinity between the bolts and the flow cross section. This flange was welded to the driven section. A seal between the driver section and the flange was created using a rubber gasket and high vacuum grease.

For pressurized gasket joints, the acceptable bolt spacing between consecutive bolts should not exceed 6 nominal bolt diameters (Budynas and Nisbett [2008]). This flange was made 10

mm thick and of mild steel. Figure 4.3 shows a CAD rendered image of the new flange. The fastening method between the driver and driven sections comprised four M10 bolts and two steel studs of M10 thread.

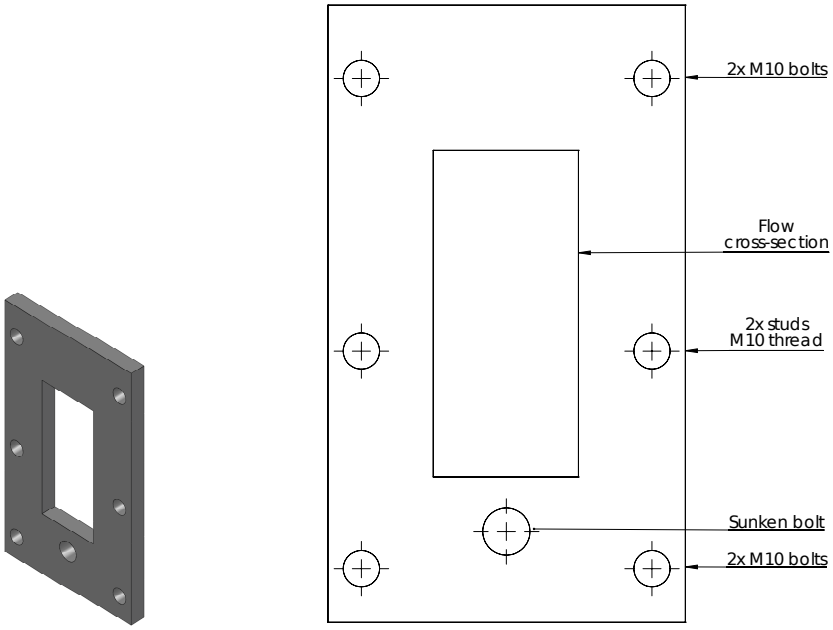


Figure 4.3: CAD drawing of the flange. Thickness = 10 mm.

Pressure transducers Two pressure transducers were added to the rig where their positions are identified in figure 4.4. (The existing transducers, B and C were located on either side of the diaphragm). Transducer-D was positioned directly above the diffraction corner and transducer-A was added to the driven section for potential calculation of the shock speed.

Air leakage Air leaks were found to exist at mating locations between components and along certain areas where the flange attached to the driver block. A combination of high vacuum grease, O-ring seals, clear-set Putty, and silicone were used to semi-permanently seal the air leaks. Some damage was caused to the threads when machining and tapping the hole to accommodate transducer-A. When the transducer was screwed in place resulting air-leakage occurred when the driver block was pressurized to > 4 bar gauge. Plumbing tape was wrapped around the transducer threads resulted in the leak being minimized but not eliminated. The boring down process resulted in certain regions developing air-leaks but was sufficiently contained with high-vacuum grease and clear-set putty. The air leakages could not be eliminated without spending an exorbitant amount of time to solve this problem. This problem was inherent from the initial design and manufacture of the acquired shock tube. It was decided to best contain the air-leaks through minimizing their presence.

Diaphragm picker The acquired shock tube used a diaphragm picker that was a long wire-thin metallic shaft with a pointed tip. This was held in position by the operator and pushed

into the diaphragm. A revised method by the author used a guide block and a sturdy steel rod with a sharp tip. The guide block was secured to the working table using standard G-clamps. This ensured an almost consistent location of where the picker ruptured the diaphragm. Spring or electric actuation would be preferable to entirely eliminate human involvement with the experiment, although time did not permit development of such device.

Earth cable During initial stages of experimentation, the oscilloscope was found to trigger when the picker touched any metallic component of the rig. A copper cable was connected between the driver section and a relatively large steel structure that served to electrically ground the rig. Thereafter no spurious trigger of the oscilloscope occurred should the diaphragm picker come in contact with the rig.

Isometric view of the modified shock tube An exploded isometric view of the modified sock tube is shown in figure 4.4 with relevant changes indicated on the drawing.

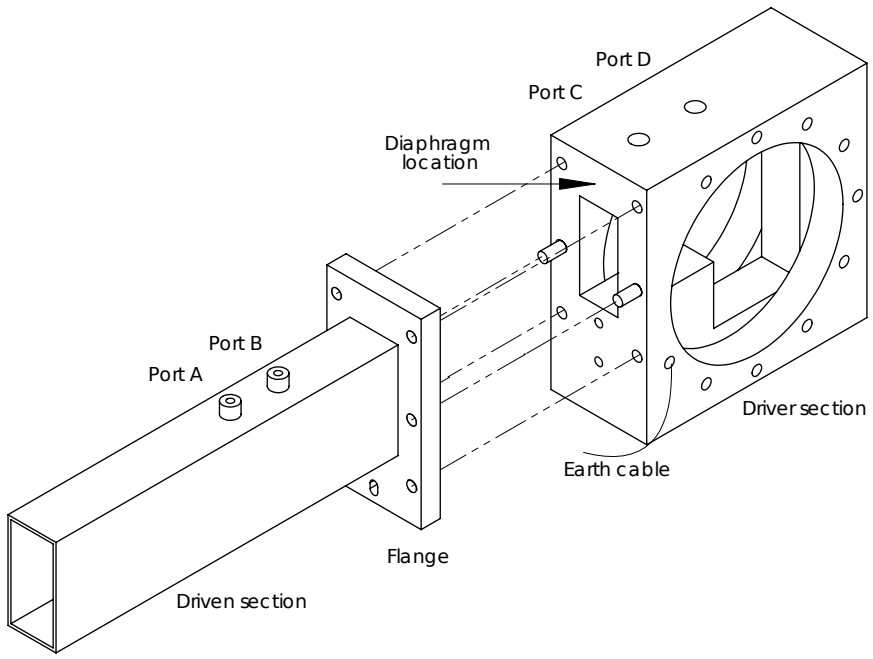


Figure 4.4: Exploded CAD drawing of the modified shock tube.

4.5 Facility Description and Instrumentation

The instrumentation and flow visualization equipment used for the present study was of standard type equipment found at the laboratory. The devices used was: pressure sensors and signal conditioners, an oscilloscope and a trigger-unit. The flow visualization equipment comprised of: digital cameras and accessories, lighting units, optical elements such as lenss

and mirrors and support elements such as optical stands and guide rails. Two configurations were developed for each camera type, Nikon D40 DSLR 10MP digital still camera and Photron SA5 high speed camera (operated at 0.125 MP and 60 000 FPS). Both cameras captured diffracted light passing through the flow-field/test-section. Appendix B, documents calibration data for the pressure transducers and other instrumentation. A photograph of the modified rig is shown in figure 4.5.

Two oscilloscopes were used, the first was to log pressure data however this data was not suitable due to the sampling rate on the oscilloscope during data capture. The second oscilloscope was to provide a trigger signal to initiate data capture for the camera unit.

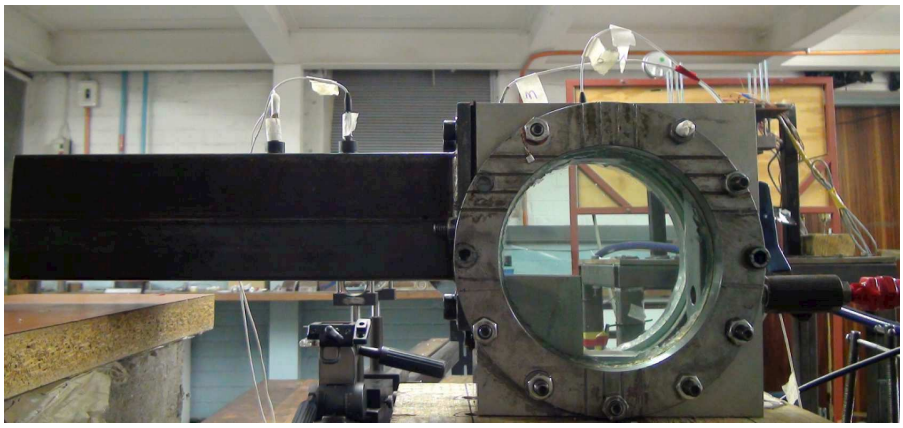


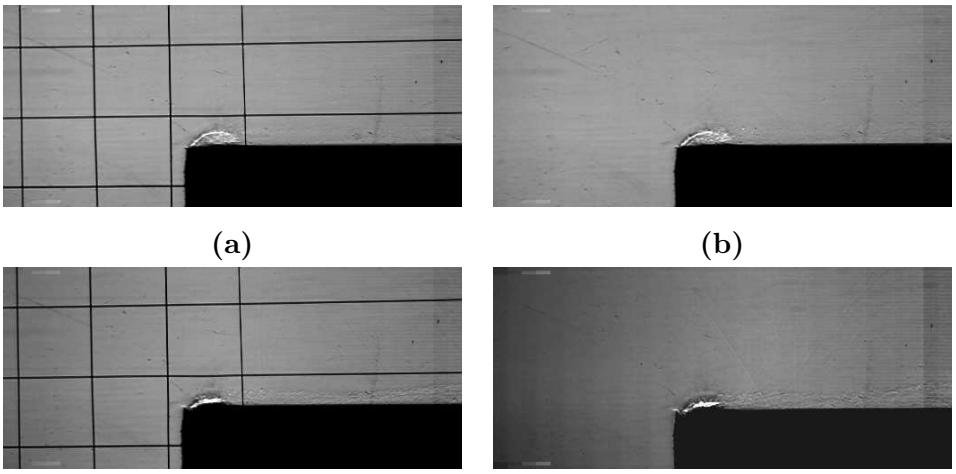
Figure 4.5: Photograph illustrating the modified shock tube.

4.6 Repeatability of Experimental Results and Rig Performance

4.6.1 Experiment Repeatability

A qualitative approach was selected to assess the repeatability of experimental results obtained with the modified version of the shock tube. This was accomplished by comparing, at equivalent frames, the data from two consecutive experiment runs at a fixed diaphragm pressure ratio (P41) and observing the flow field at the 90° corner following diffraction of the incident expansion wave. The data captured was shadowgraph images using a high-speed camera. Two frame positions were considered, and corresponded to 350 and 400 μs, following diaphragm rupture.

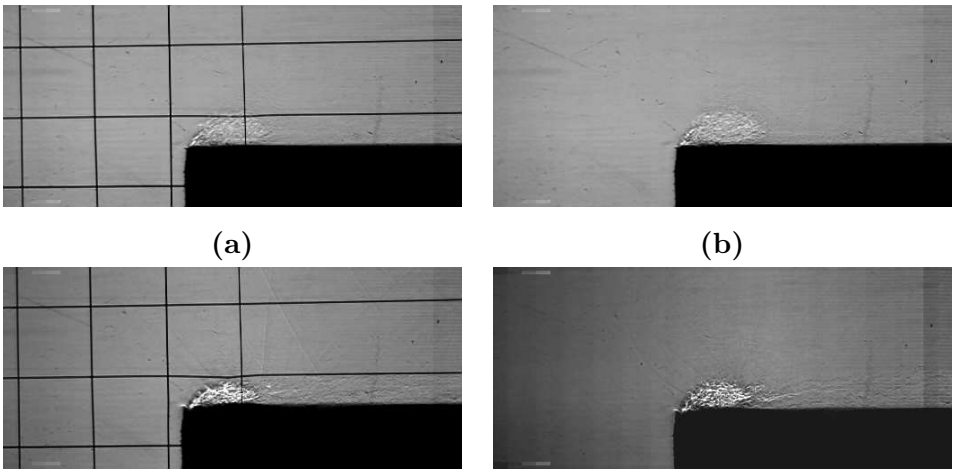
Figures 4.6 and 4.7, describe the comparison of shadowgraph images, at two consecutive experiment runs, for P41 = 1.8 and 7.7 respectively. These P41 values, corresponded to the lower and upper limits of the range (of P41) considered for the experimentation. At 350 μs, it was evident that the flow field at the 90° corner was similar between the two runs. This result was also observed for a later time, shown for 400 μs. Therefore, it was concluded that, the modified shock tube provides sufficient experiment repeatability for a qualitative study of expansion wave diffraction.



(a) **(b)**

(c) **(d)**

Figure 4.6: Selected high-speed shadowgraph images to illustrate experiment repeatability. **(a, b)**: P41 = 1.8, **(c, d)**: P41 = 7.7. t_f = 350 μs.



(a) **(b)**

(c) **(d)**

Figure 4.7: Selected high-speed shadowgraph images to illustrate experiment repeatability. **(a, b)**: P41 = 1.8, **(c, d)**: P41 = 7.7. t_f = 400 μs.

4.6.2 Rig Performance

The performance of the rig is indicated by the available experimental test-time and discussed in Appendix C. Relevent results are included in this subsection. This time would provide a measure of an experiment's duration in absence of rig-dependent effects arising at the 90° corner due to wave reflections off the shock tube walls. The available experiment test time was established to be between $350-400$ μs. This time was measured from when the leading-edge characteristic of the expansion wave propagated over the 90° corner. For a fixed value of D, short-duration test-times was achieved at low values of P41.

4.7 Experimental Procedure

A typical experimental procedure involved a series of pre-checks and activities.

4.7.1 The Pre-Check List

The following activities aid to generate a successful test and maintain a safe operational environment. They involve variables which the experimenter has control over.

1. The test windows and test section must be clean from dust, grease and debris.
2. The diaphragm film must be placed comfortably in its location with no creasing or folding. The film must be free of tiny debris particles.
3. The bolt and nut fasteners on the flange must be tight and secure.
4. The base of the rig must be level and not prone to rocking or sliding.
5. The diaphragm picker guide block must be secure and not prone to any movement, the plunger must be position inside the driven section.
6. The sensor wiring should not interfere with the test-section for flow visualization.
7. The earth cable connection must be secured and place on the rig.
8. The safety lens cover on the camera must be removed (high-resolution camera only).
9. The correct camera settings must be applied.
10. Sufficient time must be allowed for the instrumentation to settle (attain a steady state condition). Roughly two minutes was found adequate.
11. The time and voltage divisions of the data capture oscilloscope must be set.

4.7.2 The Procedure and Precautions

Following the pre-check list, the experimental procedure, in terms of specifying an inlet gauge pressure for the driver section of the modified shock tube was of a fairly standard process and similar to the conventional shock tubes present in the Barlow World laboratory at the University of Witwatersrand. However, the following set of activities were required in an interest of operational safety for the experimenter and near-by persons, during experimentation:

1. A first emergency siren was sounded for roughly 5 seconds. This was to signify initiation to pressurize the driver chamber. Sudden decompression may occur if the diaphragm was not seated correctly, if debris upon the film or bolt clamping region was not cleared, or if the bolts were inadequately secured.
2. The pressurization of the driver section may initiate a voltage from the pressure transducer and reflected on the trigger-oscilloscope. This voltage signal was required to attain steady-state condition.
3. All light sources are switched off except for an operator head lamp for the experimenter to safely navigate within the room.
4. The emergency siren was repeated for 5 seconds to alert near-by persons of a test.
5. The image capture process, too, was of a standard procedure performed using a wireless remote.
6. The pressure valves are then closed.

At all times during the above instruction set, auditory protection must be worn and the usage of the siren was compulsory. This was in the interest of safety to the operator and near-by persons.

5 Computational Method

5.1 Introduction

The primary objective of the present study was to investigate the fundamental behaviour of expansion wave diffraction around a 90° corner and explored using experimental and computational methods. The experiment method was covered in section 4. The broad objective of the computational study was to gain insight into the physics of the diffraction process and extend the parameter space of the investigation beyond that which was achieved by experimentation. Relevant experimental data related to expansion wave diffraction was not available nor reported on in the literature. A necessity arose to validate the simulation results which required some sort of experimental data. This prompted a series of experimentation where the flow visualization techniques: shadowgraph and schlieren imaging were used, discussed in the previous chapter. These results were used for the validation study in section 5.3.5.

The experimental study proved helpful since these results provided physical evidence into the behaviour of expansion wave diffraction around a 90° corner. When compared to simulation data, it was realized the simulation code was unable to resolve certain primary flow features identified by experimentation and vice versa. Therefore, experiment and simulation data was required to meet the present studies primary objective.

The commercial simulation code was ANSYS FLUENT V.13. Post processing of the simulated data was performed through the FLUENT solver and development of Matlab programs. Matlab was the primary environment to initiate or complete the post processing of the simulated data. The simulation objectives are now detailed.

5.2 Computational Objectives

The computational objectives pertaining to the present study for a shock tube generated expansion wave diffracting around a 90° corner were identified as:

1. To vary the parameter P41 beyond that achieved by experimentation. The range of P41 was chosen as: 3, 6, 9, 12, 15, and 18. (The maximum of P41 for the experiment was 8.4.)
2. For each value of P41, to vary the parameter D at reduced values compared to the experimentation. The following values of D were selected: 0, 10, 40, and 70 mm, . (The value of D, for the experiment was constant at 83 mm.)
3. To validate the simulation study using experimental data.
4. To identify the significance or otherwise of viscosity, on the temporal and spatial development of the flow field using suitable turbulence models for closure to the RANS equations.
5. To ensure grid independence and computational efficiency on the final mesh.

5.3 Computational Model

The flow domain (two dimensional) required to model the diffraction of an expansion wave around a 90° corner and the required boundary conditions are described. Two flow domains were generated. The first or *experiment domain* was to validate the user set-up of the simulation code using experiment data. This domain was based on the physical dimensions of the modified rig and subsequently was constrained to a short simulation-time. This constraint was a consequence of, following diaphragm rupture, the reflection of the diffracted expansion waves from the shock tube walls and their arrival into the region of study. This led to rig-dependent effects.

To generate longer test-times in absence of rig dependent effects, for experimentation, a physically, larger rig would be required. A reduction in gas temperature or molecular weight within the driver section may suffice. This would be welcomed for a project to further this research. A viable and time effective alternative to achieve longer test-times was found by simply employing a larger or *extended domain* and this would permit a more meaningful study.

Both, Euler and Navier-Stokes solvers were used however their mesh requirements differed and therefore two flow domains were generated.

5.3.1 The Experiment Domain

This domain was sized based on the physical dimensions of the modified rig and illustrated in figure 5.1 with the appropriate boundary conditions. This domain consists of two rectangular shapes representing the driver and driven sections respectively. These boundary conditions were selected to generate a left-running expansion wave propagating upstream into the driver section (and a shock wave propagating downstream). In this figure, the far right-end of the domain was initialized at atmospheric conditions for pressure and temperature and with zero mass flow-rate. The diaphragm was mimicked in FLUENT by an *interface* boundary, separating the driver and driven sections. To achieve a desired *diaphragm pressure ratio* (P41), the driver section was *patched* to a desired,uniform gauge pressure and similarly for the driven section patched at the atmospheric pressure value.

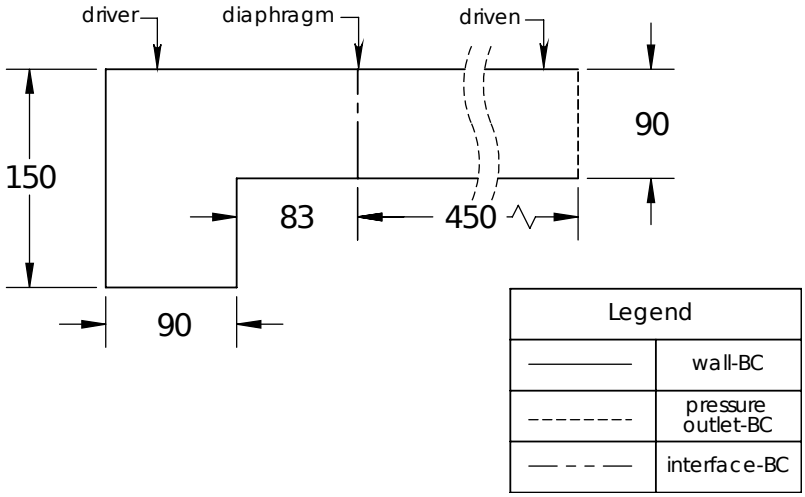


Figure 5.1: Schematic of the experimental flow domain as modelled in ANSYS FLUENT.

5.3.2 The Extended Domain

A simple approach to delay the effects of rig-dependency and to achieve longer simulation test-times was to develop a larger domain compared to figure 5.1, this larger domain appears in figure 5.2. The boundary conditions and their initialization to generate an expansion wave (and shock wave) were identical to that covered in section 5.3.1. The value of D was varied according to values listed in the Computational objectives, section 5.2.

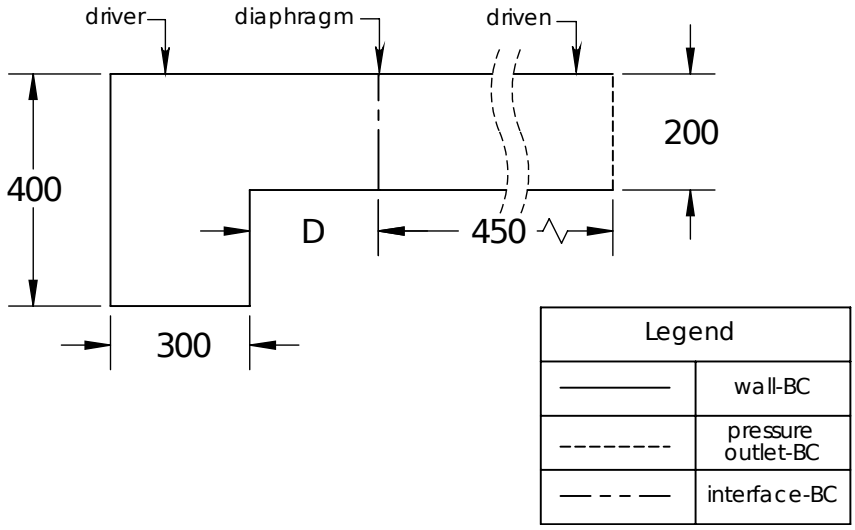


Figure 5.2: Schematic of the extended flow domain modelled in ANSYS FLUENT

5.3.3 Euler Solver

The equations that were numerically solved in ANSYS FLUENT were the unsteady, compressible Euler equations and the Reynolds Averaged Navier-Stokes (RANS) equations, both for two-dimensional flow and with air as an ideal gas. The RANS equations required closure provided in the form of a turbulence model. Two models were considered and are discussed later in this chapter. The solver settings and initial conditions are briefly described and were identical for both Euler and Navier-Stokes. The information with regards preferred selection of options in FLUENT was obtained from Ansys [2009].

The gas type (air) was assumed to obey the ideal gas law. Changes in thermodynamic properties were assumed to occur under the assumption of constant specific heats. This assumption held true for the simulated range of the P41 values and was discussed in chapter 2, section 2.2.4.

For an unsteady compressible flow field with moving shocks, an explicit and density-based (coupled) transient solver should be used. Furthermore, the descritization of spatial terms should be second-order explicit. This provides optimum accuracy (Ansys [2009]). The temporal terms, present only for the transient setting, should be discretized using an explicit time-stepping scheme; this setting has greater computational efficiency than an implicit scheme

A second order implicit solver is recommended for transonic or supersonic flow with stationery shocks. For moving shocks, this scheme behaves in a dispersive manner. Trial simulations performed with this scheme returned shock wave resolution in a dispersed fashion spread over a few grid cells. However, it may be possible to use a first-order accurate, time-implicit

scheme if the time-step to achieve convergence at each iteration, is made sufficiently small; although this approach was not recommended.

Flux descritization was chosen to be performed using the AUSM+ scheme; the default setting was the ROE-FS scheme. It was noted during trail simulations, the AUSM+ scheme gave improved resolution of the shock and contact-surface discontinuity than the default setting. Also the preferred option for evaluation of gradients is *least squares cell-based*. Dynamic mesh adaption based on solution data was used to improve flow field resolution which also improved the usage of the available computational resources.

The initial conditions for pressure and temperature to simulate experiment conditions are now described. The initial conditions are listed in table 5.1 and the atmospheric conditions were: P_{atm}=83400 kPa, T_{atm}=288 K.

Gauge pressure - driver section [bar]	Gauge pressure - driver section [kPa]	Absolute diaphragm pressure ratio
1.8	150120	3.2
3.6	300240	5.6
4.6	383640	6.5
5.6	467040	7.7

Table 5.1: Initial conditions in the driver section

5.3.4 Grid Independence Study

The two-dimensional Euler equations, for unsteady, compressible flow, were approximately solved in FLUENT, on a grid comprising of discrete cells or elements. The computational solution was therefore a function of the grid cell- or element-size. A successful grid would not influence the accuracy of the approximate solution i.e. the numerical errors associated with the grid are minimized or cannot be minimized any further implying the grid is *converged*. However, too small or too large an element size may negatively influence the numerical error. The appropriate cell size would not necessarily be infinitely small and depends on the physics being modelled. Also, the simulation was transient and a steady-state technique to ascertain grid convergence would not be suitable. Two techniques for transient flow were adopted to identify a successful meshing strategy.

One-dimensional flow

The first technique considered the analytic equations to describe flow properties in a shock tube. These equations remain valid where the instantaneous state of the flow in the shock tube

is uniform and one-dimensional. Before the onset of expansion wave diffraction, the flow field in the shock tube maintains its one-dimensional character and the analytic equations were used as a performance indicator to the numerical, euler solution. Static pressure was extracted along a horizontal line within the expansion wave, at a fixed time. The corresponding analytic result was calculated using the approximation scheme outlined in section 3.2.

The cell type considered for the verification study was uniform, structured, quadrilateral cells with equal *vertical* (y) and *horizontal* (x) lengths and without dynamic mesh adaption. The instantaneous pressure variation through a one-dimensional expansion wave, for various mesh topologies, is shown in figure 5.3. From this figure, it was concluded that the coarsest mesh, 1.0 x 1.0 mm was not suitable as the computational result over-predicted the pressure at early non-dimensional time. Thereafter, at later non-dimensional time, the variation of pressure through the expansion wave was observed to agree well with the finer meshes. The pressure curve for 0.6 x 0.6 mm evidently proved mesh independence since this result overlapped almost entirely with the finest mesh of 0.24 x 0.24 mm.

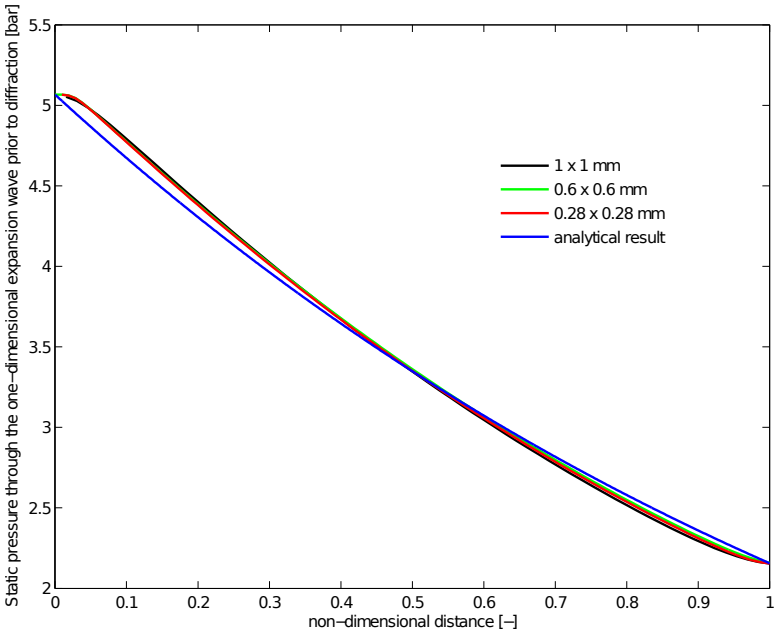


Figure 5.3: Plot of static pressure through the one-dimensional region of the expansion wave, at fixed time and shown for various mesh topologies.

At late non-dimensional time, it was observed that neither computational result for the pressure curves in figure 5.3 agreed to the analytical prediction. A plot similar to figure 5.3 with flow velocity as the independent variable is shown in figure 5.4 where the theory indicates a *linear* rise for the instantaneous flow velocity through the expansion wave. However, from the simulation, the end-points of the velocity and pressure plots were curved.

This curvature indicated an existence of smooth derivatives in the flow variables across the leading and trailing characteristics. The theory (Method of Characteristics), however, has these derivatives as discontinuous across these characteristic lines and assumes an infinite acceleration across the leading characteristic and similarly an infinite deceleration across the trailing characteristic. In the simulation, the finite cell size of the mesh leads to an approximation where the singularity arises in the theory; at the leading and trailing characteristics. This approximation resulted in the end points being somewhat curved and therefore not agreeing to the theory. It was anticipated, an infinitely small cell size of the mesh would generate a result as described by the Method of Characteristics.

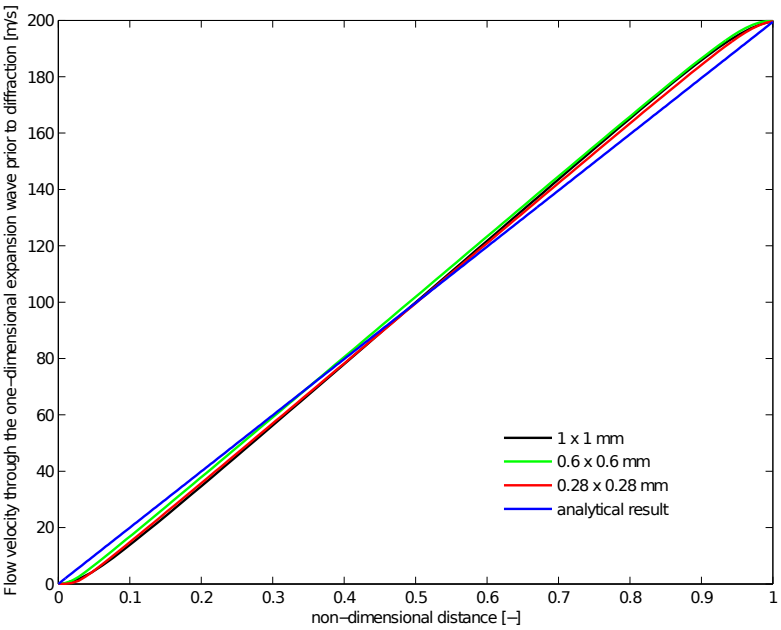


Figure 5.4: Verification plot for the 1 dimensional region established by considering the variation of gas velocity through the expansion wave.

To conclude, a 0.6 x 0.6 mm cell size was deemed converged to sufficiently model the one-dimensional region of the expansion wave whose result largely coincided with a finer cell size.

Two-dimensional flow

It was then required to establish the cell size for grid convergence in the diffracted (two -dimensional) region of the expansion wave, where the one-dimensional analytical equations no longer remain valid. The grid convergence technique used was derived from Ripley et al. [2006] where a data pick-up point in the diffracted region was selected, from which density was plotted as a function of non-dimensional time and various mesh topologies. This result appears in figure 5.5.

Rig dependent effects were not accounted for in this grid independence exercise since they extend beyond the scope of the present study. Examining figure 5.5, the two intermediate grids, corresponding to 0.6 x 0.6 mm and 0.34 x 0.34 mm, followed an almost similar path and significantly overlapped each other except for some deviation at early non-dimensional time. Physically, at early non-dimensional time, the (incident) expansion wave just propagated over the 90° corner and therefore diffracted. The developments of major flow features at early stages of diffraction were deemed unimportant. The flow field state at early non-dimensional time was, then considered as not significant.

The two outer grids of 1.0 x 1.0 mm (course grid) and 0.24 x 0.24 mm (fine grid), appeared to deviate from the path followed by the intermediate grids. This deviation was significant at early non-dimensional time and thereafter minimized as the curves collapsed upon an almost similar path. It was expected that the result for the coarsest grid would deviate significantly relative to the finer since a relatively course grid would amplify errors in a numerical solution. A similar statement may be offered for a too fine cell element size for the fine grid where error may arise through numerical truncation. For a qualitative study it was then possible to establish a computationally efficient mesh strategy based on these results.

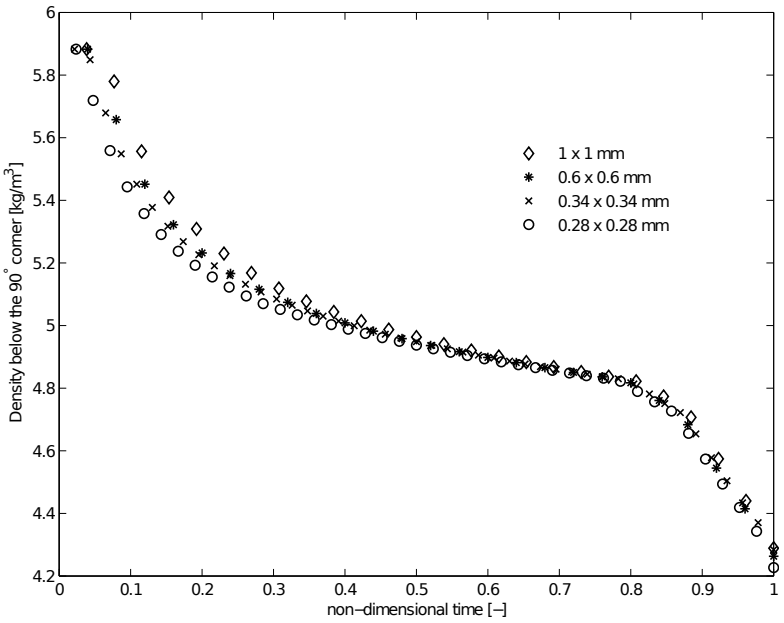


Figure 5.5: Verification plot for the 2 dimensional region taken below the 90° corner.

From figure 5.5, evidently the intermediate grids of 0.34 x 0.34 mm and 0.6 x 0.6 mm follow an almost similar path for non-dimensional time > 0.2. However the mesh application in FLUENT failed at an element size of 0.34 x 0.34 mm since the workstation had insufficient RAM memory. If dynamic mesh adaption was used on this finest cell size at a minimum cell refinement factor of two, the resulting mesh may be too fine causing an increase in the numerical error as observed for the element size of 0.28 x 0.28 mm.

Mesh data	**Units**	**Diaphragm to corner distance**				
	mm	0	10	40	70	83
Element type	-	Unstructured quadrilateral				
Element size	mm	0.6 x 0.6				
Dynamic mesh adaption	-	Level 2				
Skewness max.	-	0.471	0.676	0.686	0.552	0.054
Skewness average	-	3.12e-3	1.40e-3	1.33e-3	1.65e-3	1.50e-4
Number of elements	-	583299	588953	605821	622476	170700

Table 5.2: Summary of mesh data for the Euler solver

A solution was found by selecting the cell size of 0.6 x 0.6 mm with dynamic mesh adaption at a cell refinement factor of two, allowing a minimum cell size of 0.3 x 0.3 mm, on an unstructured grid. This strategy should meet convergence in both the one- and two-dimensional regions of the flow field. Table 5.2 shows a summary of mesh data for the grids used in the study where the value of D was varied. However for the grid independence study, the Element type was *structured* and no dynamic mesh adaption was used. These grids were coupled to an Euler solver. To account for boundary layer effects upon the vertical and horizontal walls of the test-piece, a slight adjustment was required by introducing an *inflation layer* upon the boundary walls of interest, which is covered in turbulence modelling.

5.3.5 Validation Study

This section established, through qualitative means, how agreeable the Euler results were, with that obtained from the experimentation, using the *experiment domain* which was introduced and discussed in subsection 5.3.1. This was qualitatively accomplished by matching, in a temporal fashion, select frames from the experiment and Euler results and observing the appearance of major flow features in each frame. This comparison is shown for three frames at P41 = 3.2 in figure 5.6 and at P41 = 6.5 in figure 5.7.

The major flow features which are evident in the experimental images of figure 5.6 are listed below. (The major flow features are formally introduced in chapter 6, section 6.3).

- A shear layer originating close to the apex of the test-piece.
- A separation bubble and a wake region immediately downstream from the bubble's rear. Note: The separation bubble had no distinct spiral pattern that is commonly associated with the free vortex observed in shock diffraction off a 90° step (Takayama and Inoue [1991]).

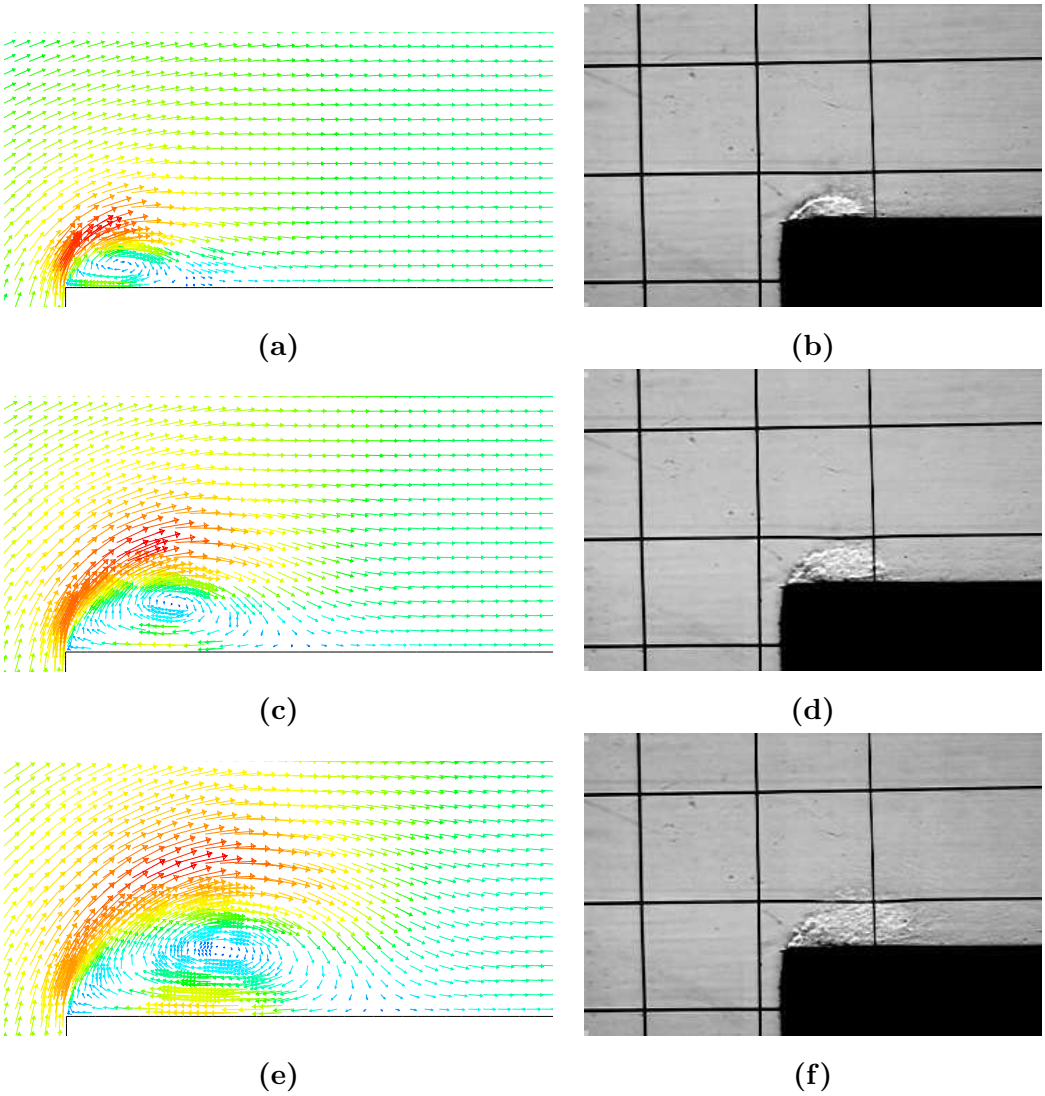


Figure 5.6: Qualitative comparison between the Euler solver and high-speed shadowgraph images at P41 = 3.2 (± 0.2 bar for experiment). Times from arrival of leading characteristic at the corner (μs): **(a, b)** 150, **(c, d)** 232, **(e, f)** 317.

- A rather turbulent circulatory flow seemed to develop within the separation bubble which was anticipated and confirmed through simulation.

The Euler results agree to some extent with the experiment where the shear layer was observed to originate at the 90° corner and a separation bubble formed on the horizontal wall. The temporal growth of the separation bubble, visually, appeared similar in shape between the experiment and simulation, where the shape was roughly elliptical.

However, the turbulent flow observed in the separation bubble was not resolved using the Euler solver nor was the 'wake' region that existed for a considerable length, immediately downstream of the bubble. The solver also indicated significant flow velocity in the region

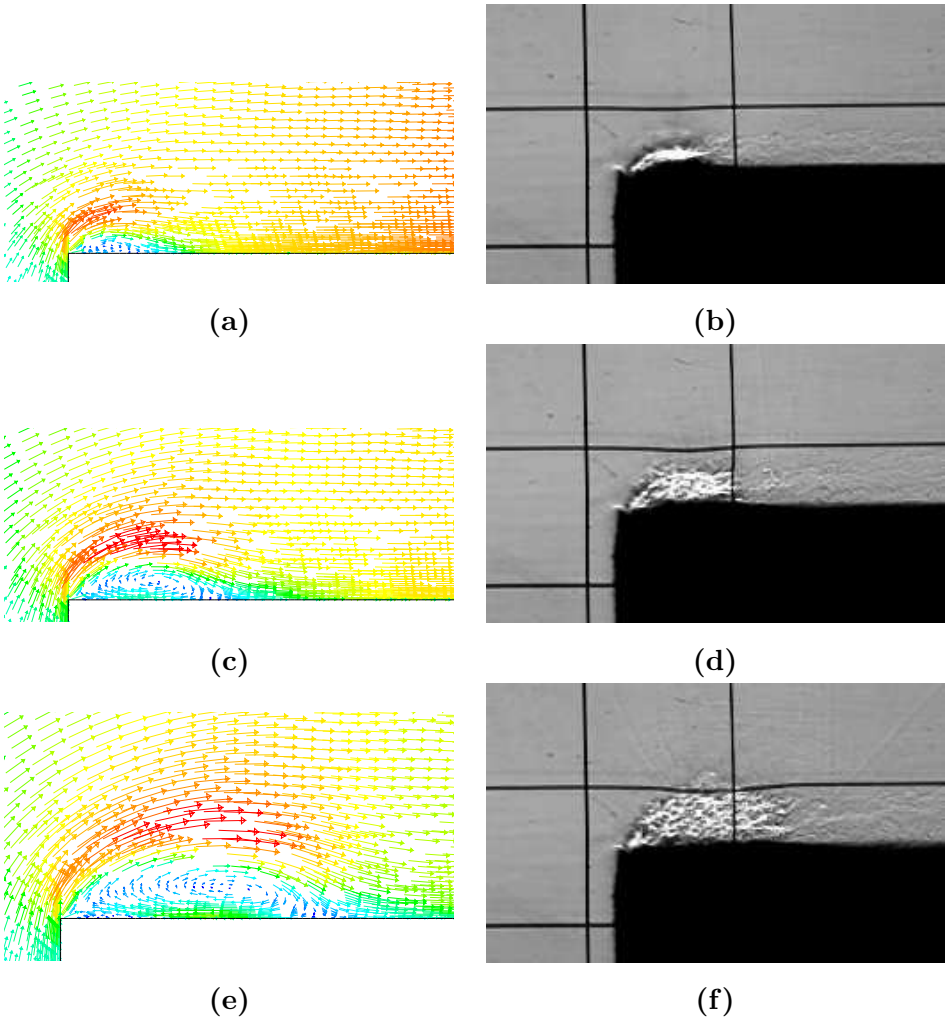


Figure 5.7: Qualitative comparison between the Euler solver and high-speed shadowgraph images at P41 = 6.5 (± 0.2 bar for experiment). Times from arrival of leading characteristic at the corner (μs): **(a, b)** 150, **(c, d)** 232, **(e, f)** 317.

close to the horizontal wall enclosed by the separation bubble. Since the separation bubble was observed to remain attached against the horizontal wall in the experiment images, a stagnation point must exist at the bubble's rear and close to the wall. The wall represents a solid surface where boundary layer effects occur that may render the Euler results unsuitable to investigate the growth and behaviour of the separation bubble. Evidently, there is a close interaction of the separation bubble with the horizontal wall.

Therefore, the Euler solver may be suitable for the study of the flow field away from the separation bubble however the need for a viscous simulation was clear requiring the selection of an appropriate turbulence model. This is now considered.

5.4 Turbulence Modelling

It has been established for a case of shock diffraction over a 90° corner that boundary layer effects upon the solid walls at the diffraction corner are non-negligible at short time and length scales (Law et al. [2012]) where these scales were applicable to the present study. It was established in the previous section a need arose to consider boundary layer effects since the bubble was attached to the horizontal wall, shown in figure 5.6.

The no-slip condition must exist on the horizontal wall (and is satisfied for non-moving boundaries in FLUENT), and implies that the tangential velocity of the moving fluid at the wall must be zero i.e. u_t=0. In particular, for a rapid rise in flow velocity near the wall, this would result in steep velocity gradients within the boundary layer along a normal direction, $\frac{\partial u}{\partial y}$. Also, the time and length scales for the experiments of the present study were short. However, evident in the experiment images in figure 5.6, turbulent flow was identified within the separation bubble. It was decided to obtain results using a turbulence model. The Navier-Stokes solution with appropriate turbulence modelling sought to address the aspects below where a coupled RANS solver was selected in FLUENT with air as an ideal gas.

- Did the fluid viscosity significantly affect for the evolution of the diffracted flow field? ,
- Did a laminar boundary layer assumption hold true based on small time and length scales?,
- Could the post-diffracted flow field be sufficiently analysed using an Euler solver?, and,
- To what extend did the RANS equations model the turbulence in the post-diffracted flow compared to experimentation.

The selected turbulence model was Menter's SST k-ω turbulence model. This model was selected for its versatility and potential to model turbulent boundary layer flow and free stream turbulence. Turbulent flow was identified within the separation bubble's core and the boundary layer flow at the horizontal wall within the bubble may be turbulent. Free-stream turbulence was present in the 'wake' region downstream from the separation bubble. This turbulence model blends a k-ϵ model for its free stream accuracy and k-ω to utilize its near wall capability at the boundary layer region.

5.4.1 Grid Generation and the RANS Solver

The implementation of the coupled RANS solver with a suitable turbulence model for closure necessitated special requirements for the mesh topology at locations were boundary layer

flow would develop. The mesh requirements for this turbulence model, including that for the Laminar solver will now be covered. The Euler grid developed in section 5.3 was modified and used for the turbulence modelling.

5.4.1.1 Menter's SST k-w Turbulence Model

This turbulence model required a mesh topology with sufficient cell resolution within the anticipated region of the boundary layer where FLUENT used a *near wall modeling* approach. The cell $y+$ value was used to judge the suitability of the grid at the boundary layer region for correct functioning of the turbulence model. This criterion indicated where the fist node of the cell should be located from the wall. Correct implementation of Menter's SST k-ω turbulence model in FLUENT V.13 required the first node from the wall to be positioned either within the viscous sub layer (low Reynolds number and viscous dominant) or just beyond the buffer layer (increasingly high Reynolds number and inertia dominant i.e. $5 \leq y+ \leq 30$.

For all simulations performed with Menter's SST k-ω turbulence model, the cell's $y+$ value at the first node was within the required range of values: $5 \leq y+ \leq 30$, (Versteeg and Malalasekera [1995]). Therefore the boundary layer was correctly modelled within the accuracy available. A velocity profile through the boundary layer, for flow upon the horizontal wall, is shown in figure 5.8. The grid used was the *rig domain* and the mesh topology data appears in table 5.3 which summarized mesh topology data for this turbulence model to achieve the above range in $y+$ for both the rig and extended domains.

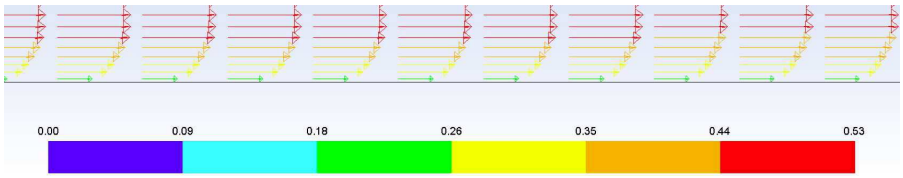


Figure 5.8: Variation of velocity through the boundary layer in a region of uniform flow and $\frac{\partial p}{\partial x} \approx 0$

The location upon the horizontal wall for the velocity profile was in a region of uniform flow and no significant adverse pressure gradient. This was evident from the constant profile shape along the length of the region considered. This location is illustrated in figure 5.9 for P41 = 3.2.

As a remark, the presence of an adverse pressure gradient would modify the stream wise variation of these velocity profiles. The location for these plots was in regions of expected

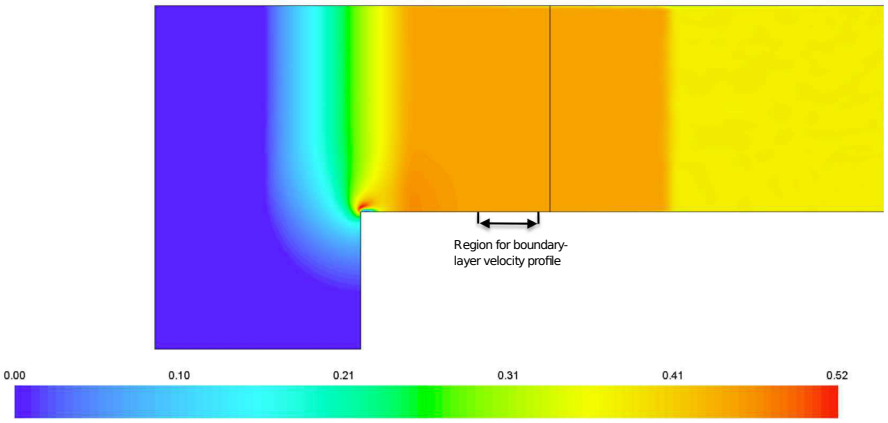


Figure 5.9: Region for the velocity profile plot through the boundary layer

Mesh data	**Units**	**Diaphragm to corner distance**				
	mm	0	10	40	70	83
Element type	-	Unstructured quadrilateral				
Element size	mm	0.6 x 0.6				
First layer height	mm	0.0015				0.045
Number of layers	-	20				30
Growth rate	%	1.15				1.1
Dynamic mesh adaption	-	Level 2				
Skewness max.	-	0.996	0.702	0.759	0.743	0.797
Skewness average	-	1.03e-1	1e-1	1.08e-1	1.02e-1	8.26e-2
Number of elements (unadapted)	-	324177	321836	327534	334538	122908

Table 5.3: Summary of mesh data for the Navier-Stokes solver

typical boundary layer development such as the vertical wall or at some downstream distance beyond the separation bubble.

The boundary development on the horizontal wall of the test-piece, as inferred from the experimental results, will require further investigation into its behaviour and development which is beyond the scope of the present study. Although FLUENT will indicate boundary layer development upon the horizontal wall and if the development of this boundary layer in the simulated environment is correct, it remains unknown if this aspect of the simulation does indeed represent reality.

The skewness metric, as described in table 5.3, was considered as a primary measure of mesh quality. An excellent meshed grid has a skewness value close to zero and ideally a value of ≤ 0.1, (Ansys [2009]). From this table, the average skewness for both domains is near or smaller than this ideal value. However the maximum skewness indicates poor mesh quality.

The poorly meshed elements occurred in vicinity of the diffraction corner due to its 90° geometry.

An image of the mesh topology (*extended-domain*) used for Menter's SST k-ω turbulence model is shown in figure 5.10 for a $D = 40mm$. A close-up view of the diffraction corner was included to the right of this image. This grid was representative of all grids used for this turbulence model and was therefore decided unnecessary to include all grids. The 90° geometry of the diffraction corner represented a singularity point in the meshing algorithm of FLUENT resulting in excessive skewness of mesh elements near the corner, as observed in this figure. This behaviour was expected and considered acceptable based on the physical geometry being modelled. It was concluded that the quality of the mesh topology as described in table 5.3 for the Navier-Stokes solver was excellent.

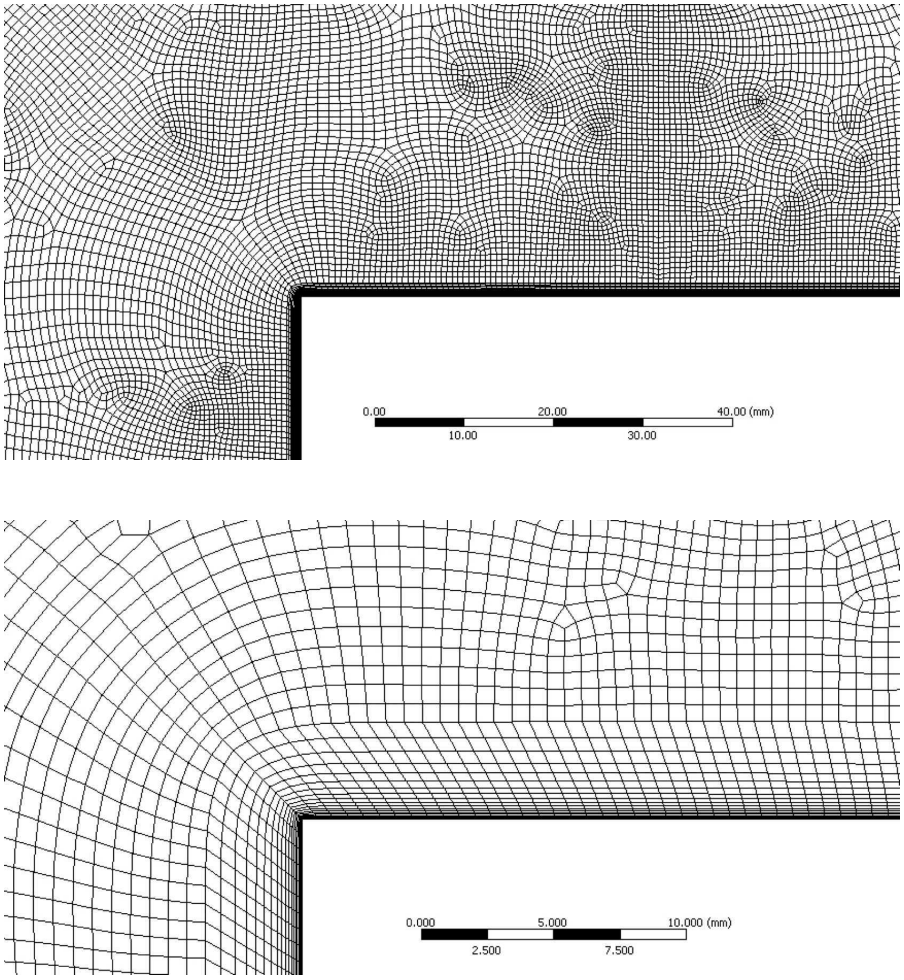


Figure 5.10: Grid topology for the Navier-Stokes solver for the *extended domain*.

The mesh topology for the rig domain differed slightly in comparison to that presented in table 5.3. To re-cap: the objective of the rig domain was to allow comparison of simulation data to experiment. For the turbulence modelling with this domain, the Navier-stokes results with Menter's SST k-ω turbulence model were compared against experimental results and

Mesh data	Units	Diaphragm to corner distance: 83 *mm*
Element type	-	Unstructured quadrilateral
Element size	mm	0.6 x 0.6
First layer height	mm	0.00075
Number of layers	-	30
Growth rate	%	1.15
Dynamic mesh adaption	-	Level 2
Skewness max.	-	0.607
Skewness average	-	2.62e-2
Number of elements (unadapted)	-	155444

Table 5.4: Summary of mesh data for the Navier-Stokes solver

the corresponding Euler cases. Compared to the extended-domain additional layers were included for the inflation layer and also a slightly larger cell size against the horizontal (and vertical) walls was found to be required. These changes allowed for the required $y+$ range to be met for correct implementation of this turbulence model in FLUENT.

5.4.1.2 Laminar Model

The objective of the laminar model was to investigate if turbulence was indeed a factor to consider since the time and length scales of the experiment were sufficiently small to assume turbulent boundary layers do not develop. The requirement to correctly implement the laminar solver in FLUENT was a fine near-wall mesh.

Similar to the discussion on the skewness metric for Menter's SST k-ω turbulence model, the average skewness was between 0 and 0.1. However, cell-element distortion was expected due to modelling of a 90° corner and this amplified the skewness metric as reported by the maximum value. Overall, the mesh topology for the laminar solver was deemed excellent. Figure 5.11 illustrates a close-up view of the mesh topology for the rig domain. The dark band along the horizontal wall of the test piece represents the fine boundary layer mesh.

A qualitative discussion comparing the results from Menter's SST k-ω turbulence, the laminar and Euler models, and the experimental outcomes is now considered in the next section.

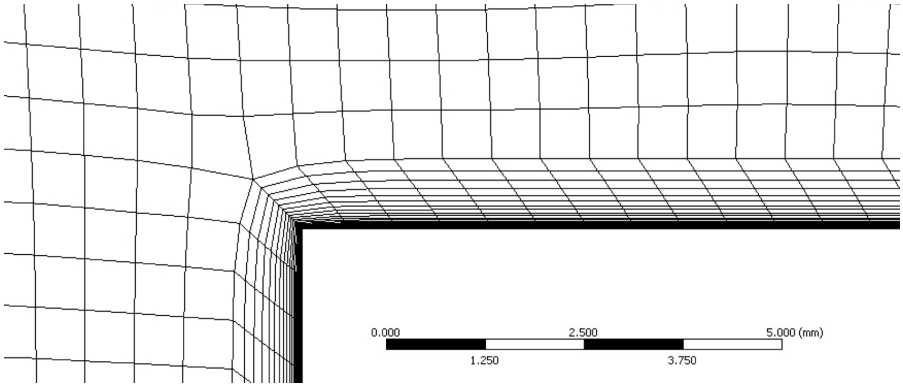


Figure 5.11: Grid topology at the diffraction corner for the Laminar solver for the *rig domain*.

5.5 Comparison of Results

A qualitative comparison between the Navier-Stokes solver with Menter's SST k-ω turbulence model and shadowgraph images taken with a high-speed camera, are shown in figure 5.12. From this figure it was evident the turbulence model did not resolve any turbulent structure experimentally observed within the separation bubble nor was the 'wake' region resolved. However, flow separation in the region upon the horizontal wall and near the 90° corner was resolved and identified in figure 5.12 (a). The shape of the separation bubble from the viscous results agreed closer to the experiment image than what was achieved using the Euler solver in figure 5.6.

Since the separation bubble remained attached to the horizontal wall, a stagnation point had to exists at the wall. The stagnation point has been formally introduced in chapter 6, section 6.5. We now consider the results from the Laminar solver by a plot of the stagnation points motion over time. Such curves were also generated for results from the Euler Navier-stokes solvers and experimentation. The curves for these simulation data are shown in figure 5.13 for P41 = 3.2 and 7.7.

From figure 5.13, the Euler results deviated from those of the viscous-solvers and considerably at P41 = 3.2. Clearly, the Euler solver was not in agreement with the viscous data. The viscous models agreed closely at late non-dimensional time for P41 = 3.2. This may indicate, at longer non-dimensional times and in absence of rig dependent effects, that a Laminar model may be suitable.

A plot of stagnation point motion with non-dimensional time for the experiment and Menter's SST k-ω turbulence model appears in figure 5.14; the result for the Laminar solver appears to aid comparison. From this plot, there was good agreement at late non-dimensional time between the viscous solvers and experiment data. However, the shadowgraph images in figure

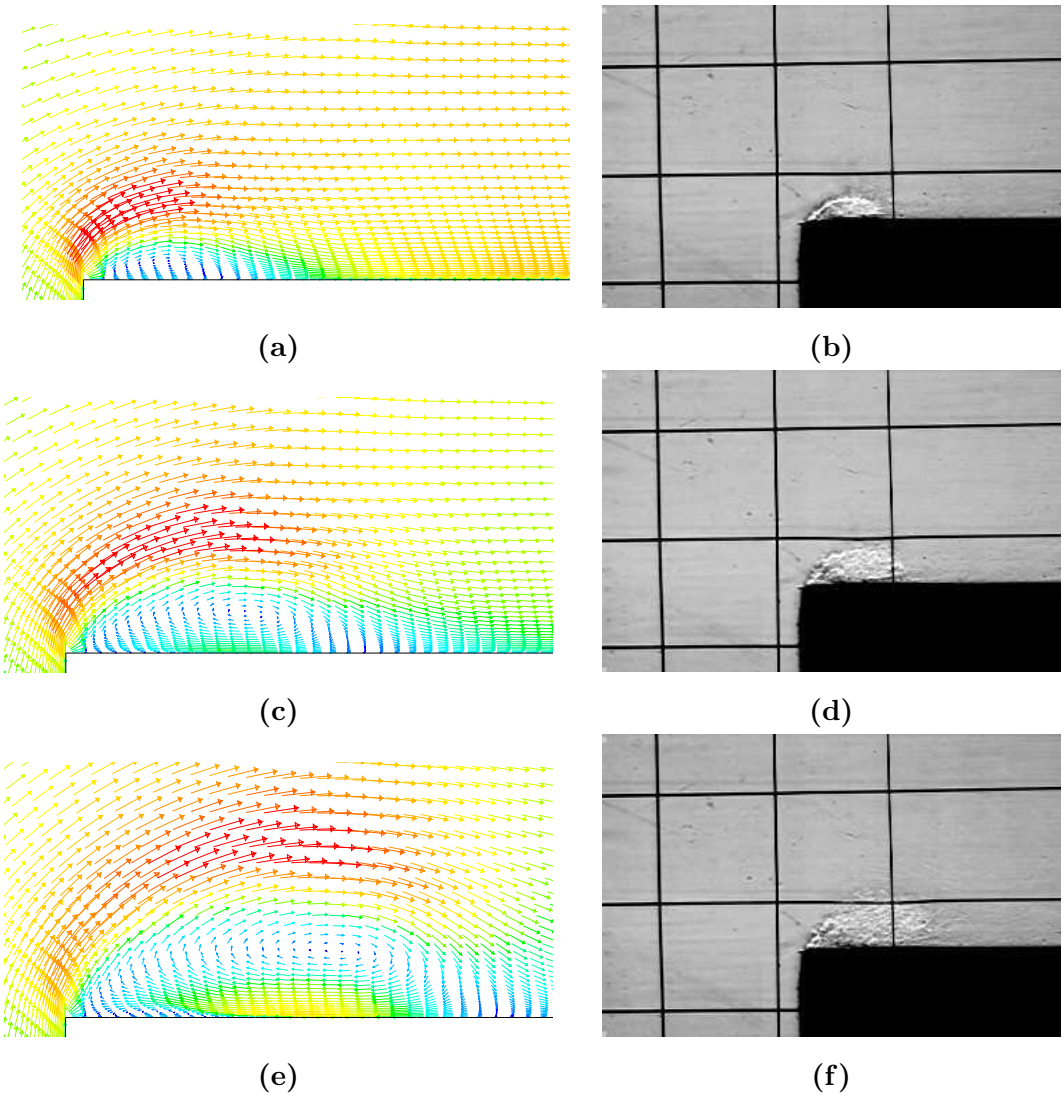


Figure 5.12: Qualitative comparison between Menter's SST k-ω turbulence model and high-speed shadowgraph images at P41 = 3.2 ($\pm$ 0.2 bar for experiment). Times from arrival of leading characteristic at the corner (μs): **(a, b)** 150, **(c, d)** 232, **(e, f)** 317.

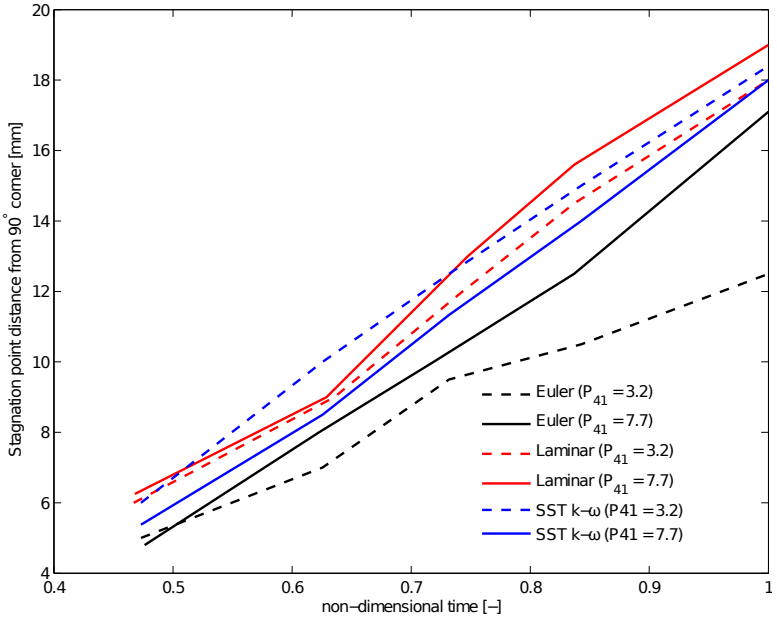


Figure 5.13: Plot of stagnation point distance from the 90° corner against non-dimensional time, for the various solvers, at P41 = 3.2 and 7.7.

5.12, clearly indicated turbulent eddies present within the separation bubble of various scales including a turbulent 'wake' region. Based on this evidence, it was decided to forgo the Laminar solver.

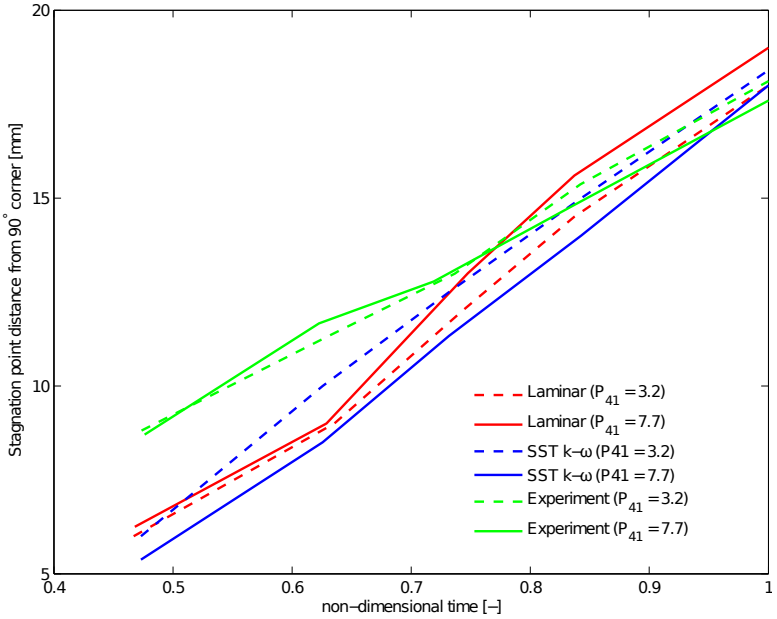


Figure 5.14: Plot of stagnation point distance from the 90° corner against non-dimensional time, for Menter's SST k-ω turbulence model, the Laminar solver, and experiment data, at P41 = 3.2 and 7.7.

Therefore, it was concluded that Menter's SST k-ω turbulence model provided the best computational result to model the diffraction of a, shock tube generated, two-dimensional expansion wave around a 90° corner.

5.6 Conclusion

The present study explored the variation of two independent parameters: P41 and D on the diffraction of a planar, one-dimensional expansion wave over a 90° corner, in a shock tube. ANSYS FLUENT V.13 was used to model this diffraction process. Two flow domains were developed, one represented the experiment domain for the validation exercise and the other was physically larger to delay the onset of rig dependent effects.

Experimental data obtained through shadowgraph imaging using high-speed and high-resolution camera's aided to validate the computational solution. This was achieved through qualitative comparison of results and considering the dynamic motion of the stagnation point against non-dimensional time.

The Euler solver was deemed insufficient to model the flow field at the 90° corner where the separation bubble developed close to the horizontal wall. A Laminar model was considered, however the experiment results clearly indicated turbulent eddies were present within the separation bubble and a strong wake region was visible immediately downstream from the bubble. It was concluded that a Navier-Stokes solver with Menter's SST k-ω turbulence model best modelled the diffraction of an expansion wave around a 90° corner.

6 Results and Discussion

6.1 Introduction

The majority of this chapter concentrates on results where the flow Mach number behind the trailing characteristic of the incident (one-dimensional) expansion wave was sub-sonic ($M_f < 1$). In Chapter 3, section 3.3.2.1, this was shown to occur for P41 < 10.4), in air, $\gamma = 1.4$. These results were obtained through a combination of experiment and simulation from which the primary (major) flow features are identified. This is followed by a detailed discussion for each primary flow feature with variation in the two independent parameters, D and P41. Lastly, simulation results for $M_f \geq 1$ are discussed.

Data of the flow field by diffraction of the incident expansion wave at the 90° corner was captured through high-speed and high-resolution cameras, and simulation. The reporting of this transient data required a *reference position* to establish the duration of the diffraction process. This position was taken at the instant when the leading characteristic of the incident expansion wave arrived at the 90° corner. This was possible for all simulation and high-speed imaging data. The following variable: t_f was ascribed for all high-speed and simulation data. A reference position could not directly be established for the high-resolution data which made use of a *time-delay* parameter. This distinction was necessary for reporting of data in this chapter and to establish the onset of rig-dependent effects which is discussed in Appendix C.

6.2 Summary of Test Cases

A summary of the experiment and simulation tests, whose results are discussed in this chapter, is provided. For the experiment tests, four values of P41 were considered and at a fixed value for D (83 mm); (P41 = 3.2, 5.6, 6.5 and 7.7). These tests was captured using shadowgraph and schlieren flow visualization techniques.

6.3 Major Flow Features

Through selected key shadowgraph images, the major flow features that were identified for the diffraction of the incident expansion wave around a 90° corner are discussed, and captured using the high resolution camera. These images appear in figure 6.1 for $D = 83$ mm and for P41 = 3.2 and 7.7.

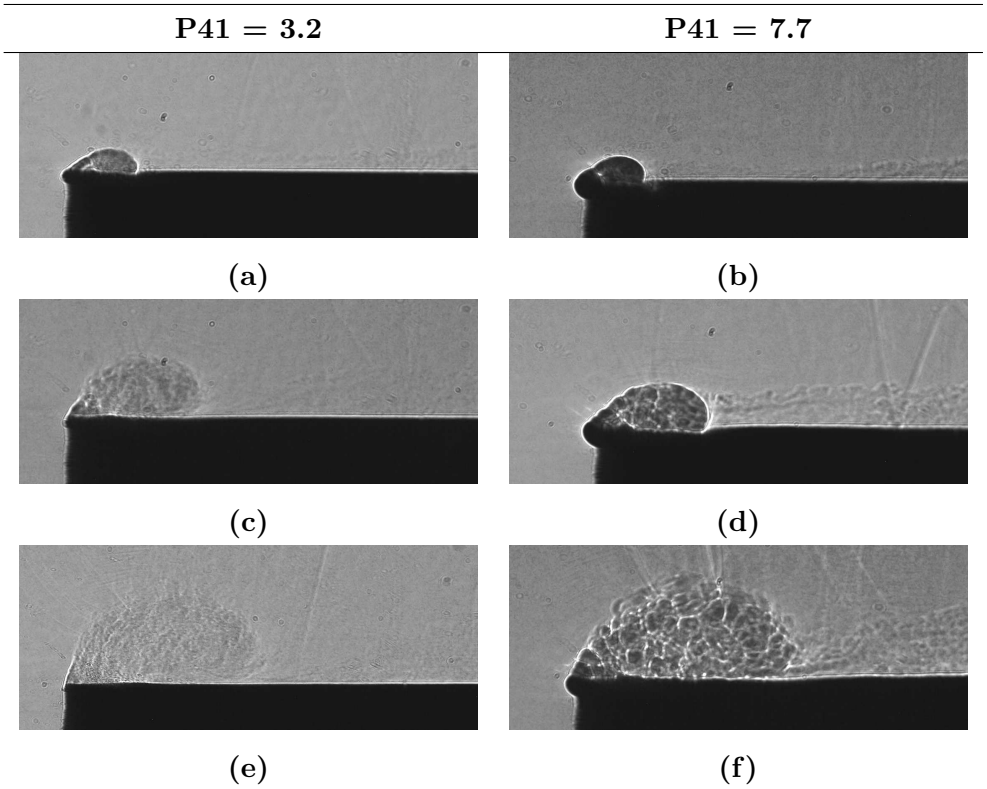
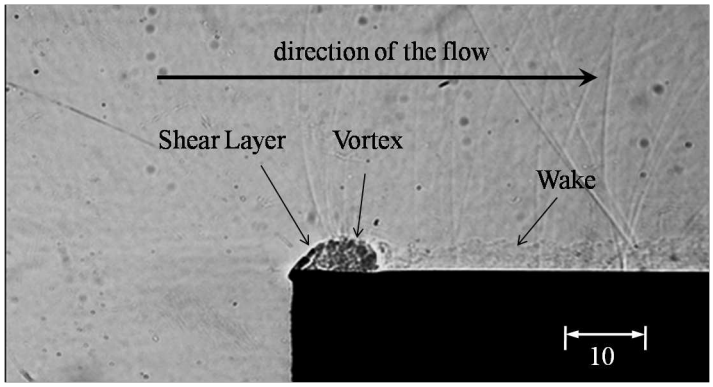


Figure 6.1: Selected, high-speed shadowgraph images to sequentially illustrate the flow field at the diffraction corner for P41 = 3.2 and 7.7. Time-delay values (μs): **(a, b)**: 200, **(c, d)**: 400, **(e, f)**: 600.

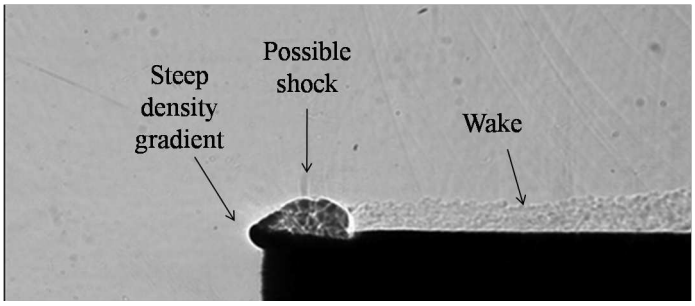
The major flow features are labelled in figure 6.2. In this figure, the arrow-head indicates the direction of flow, which was taken as positive to the right. The flow features identified through simulation appear in figure 6.3 where results were selected from $t_f = 150$ μs.

From the above experiment and simulation results, the following major flow features are identified for the diffraction of an expansion wave around a 90° corner:

- A shear layer originating at the diffraction corner,
- A separation bubble attached to the horizontal wall and enclosing circulatory fluid (vortex),
- An assumed turbulent vortex core within the separation bubble,



(a)



(b)

Figure 6.2: High speed shadowgraph images for P41 = 3.2 (**a**), 7.7 (**b**) at a time delay of 300 μs

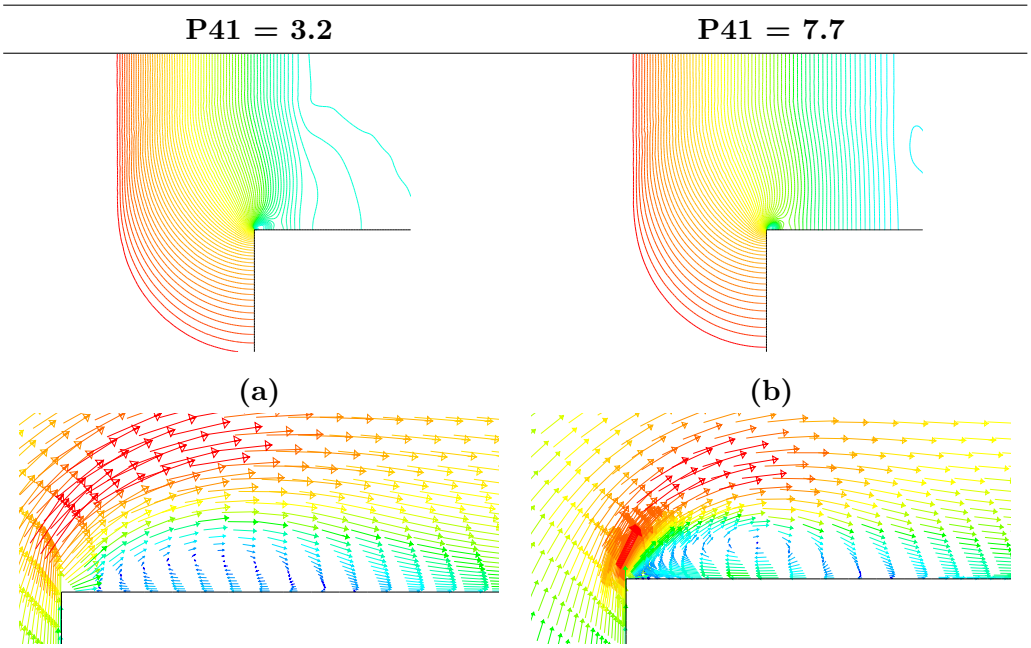


Figure 6.3: Pressure contours and velocity vector plots using Menters SST k-ω turbulence model, for P41 = 3.2 and 7.7, at t_f = 150 μs.

- A shock positioned just above the separation bubble at P41 = 7.7 and at a time-delay of 300μs,
- A region of flow immediately downstream of the separation bubble of unknown origin or internal structure and termed the *wake region*,
- Flow separation within the bubble and near the diffraction corner along the horizontal wall which is visible in figure 6.1 (a), and,
- A reflected perturbation, faintly identified for $D = 83$ mm in figure 6.3 (a) generated at the 90° corner by the diffraction of the one-dimensional expansion wave.

In figure 6.1, for P41 = 7.7 and at 200 and 400 μs time delay, a distinct bulge appeared at the diffraction corner and was significantly less pronounced for P41 = 3.2. This effect could have arisen due to the deflection angle of incident light rays, upon the region where the bulge occurred, where the deflection angle exceeded the measuring range of the optic system. The presence of this bulge was not representative of a defect in the geometry of the 90° corner.

The shadowgraph images were found to depict a series of transverse waves propagating in an upstream direction. It was believed that these transverse waves arose from the rupture of the diaphragm bursting process and appeared as families of upward and downward facing cylindrical waves. Since these transverse waves are cylindrical, their strength should weaken over time where their influence on the flow-field at the diffraction corner may be insignificant.

Turbulent flow features identified in the experiment were found unresolved in the simulation and, similarly, flow features identified in the simulation such as the reflected perturbation was not captured with the flow visualization set-up (schlieren and shadowgraph) which may require increased sensitivity. Vector plots of velocity magnitude shown in figure 6.3, indicated gross circulatory fluid motion within the primary separation bubble which confirmed the presence of vortex motion within the bubble.

In figure 6.3, a reflected perturbation was evident for P41 = 3.2 where the one-dimensional expansion wave was almost, fully diffracted. In the right image, for P41 = 7.7, the trailing characteristic of the one-dimensional expansion wave was yet to diffract over the corner and the reflected perturbation was fully contained with in this wave.

6.4 The Reflected and Diffracted Waves

The diffraction of a single element of the expansion wave, at the 90° corner, was found to generate a perturbation signal. This signal would propagate radially outward and was identified as a reflected compression wave, within the two-dimensional expansion region. For shock diffraction with a subsonic post-shock condition, a reflected expansion wave would propagate radially outward into a region of steady flow (region 3); the reflected expansion wave is circular in profile and propagates away from the diffracted shock (Skews [1967]). However, the reflected compression wave propagates into regions of steady (beyond the trailing characteristic) and unsteady flow, this will depend on the *width* of the incident one-dimensional expansion wave prior to diffraction.

In Chapter 3, it was shown that the diaphragm pressure ratio (P41), and propagation time of the incident expansion wave prior to diffraction would influence the wave's width. In the present study, for a fixed values of P41 and T21, the wave's propagation time was indirectly goverened by the distance between the diaphragm location and the diffraction corner (D). Clearly, the expansion wave's width would have some influence on the diffraction process. The reader is referred to section 3.3.3 for a discussion on this aspect.

It should be noted, that the incident expansion wave has a finite width prior to diffraction (for $D > 0$). However this does not imply a finite diffraction time. The diffraction of the incident expansion wave around the 90° corner was found to generate a series of perturbations identified as reflected compression waves. For P41 < 10.4, the reflected compression waves propagate radially outward into the flow and would modify the trailing characteristic of the incident expansion wave; this can be observed in figure 6.5. The exact physics to describe how this trailing characteristic was modified, at present, remains unknown. Contrast to a shock wave which has negligible thickness and where its diffraction over an obstacle such as a 90° convex corner can be assumed instantaneous.

A gross overview of the regions identified by the diffraction of the incident expansion wave is shown in figure 6.4, by contour plots of pressure for P41 = 6 and for $D = 0$ mm. The identified regions were: 1) the region of the incident (one-dimensional) expansion wave not yet affected by the outward propagation of the perturbation signal generated at the corner, 2) The diffracted (curved) portion of the expansion wave, and 3) The perturbation signal generated at the 90° corner by diffraction of the expansion wave.

Figure 6.5, illustrates a relatively wide-width incident expansion wave for $D = 70$ mm, with identical initial conditions for $D = 0$ mm in figure 6.4. These regions are discussed in greater detail.

The case for $D = 0$ mm was particularly interesting since the incident expansion wave did not propagate over the diffraction corner. Although, this wave developed curvature upon the vertical wall due to a change in the wall profile and the flow cross-section.

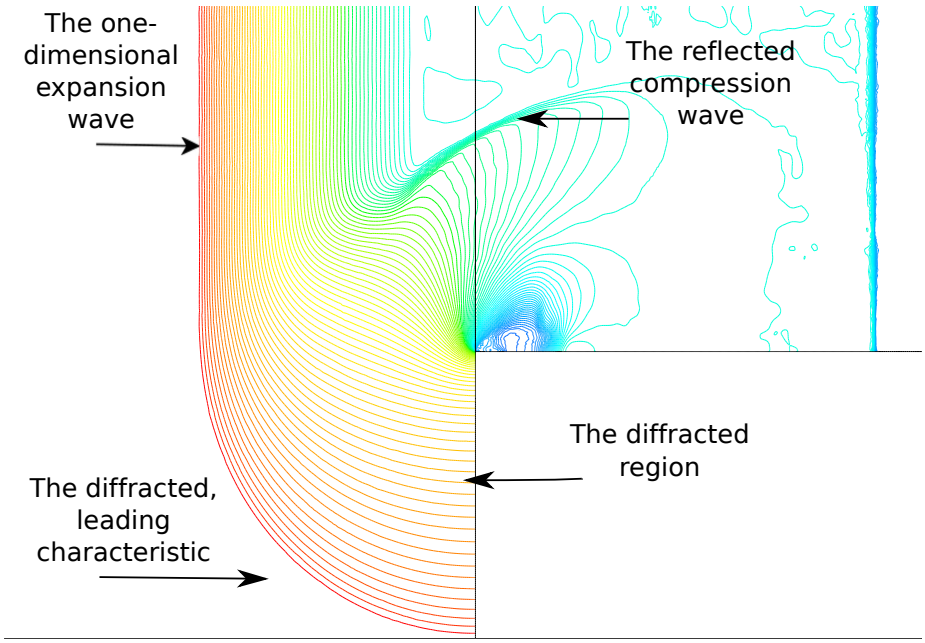


Figure 6.4: Annotated contour plot of pressure for P41 = 6 at $t_f = 250$ μs and $D = 0$ mm

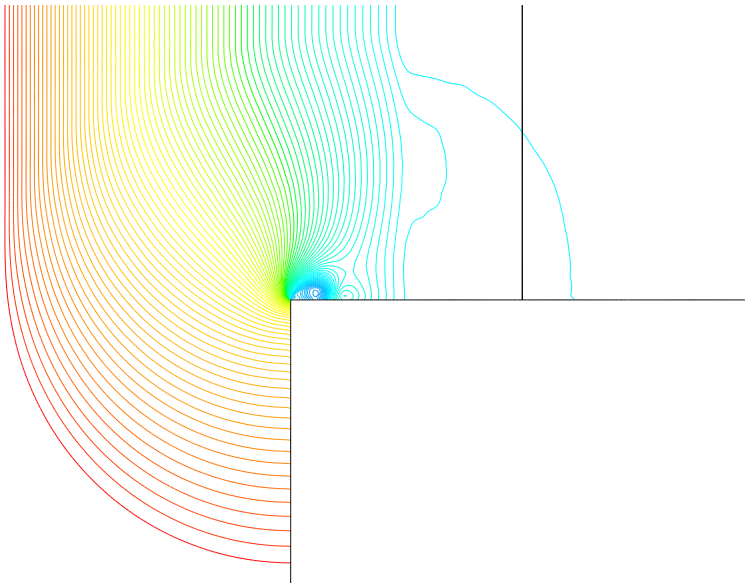


Figure 6.5: Contour plot of pressure for P41 = 6 at $t_f = 250$ μs and $D = 70$ mm

6.4.1 The Diffracted Region

The leading characteristic of the incident one-dimensional expansion wave which has diffracted in figures 6.4 and 6.5, for $D = 0$ and 70 mm respectively, developed a circular-arced profile

similar to a case of shock diffraction off a 90° backward-facing step although in the latter case the profile is not circular. The diffracted waves were observed to expand cylindrically in two-dimensional space, modfiying the pressure gradient behind them.

The diffraction of the expansion wave occurred by the propagation of the one-dimensional expansion wave around the 90° corner. The incident expansion wave underwent a further expansion due to a change in flow cross-sectional area, after diffraction around the 90° corner. Therefore, the diffracted region was expected to be weaker than the one-dimensional wave.

The boundaries which define the two-dimensional expansion wave are proposed with reference to figure 6.4. These boundaries are: 1) The diffracted leading and following characteristics and 2) the reflected compression wave (a weak, cylindrical shock wave for $D = 0$ mm) where the reflected compression wave propagates radially outwards into the one-dimensional flow.

The diffracted region of the expansion wave below the 90° corner was expected to contain the *reflected compression wave*. In figure 6.4, the reflected compression wave has coalesced into a cylindrical shock wave for the region between the trailing characteristic and the contact surface. The nature of how this reflected compression wave would modify the behaviour of the two-dimensional region below the 90° corner, at present, remains unknown.

As seen in figure, 6.4, the separation bubble is contained within the two-dimensional expansion wave where the bubble's curvature significantly influences the nearby flow field. For purpose of discussion, it is found convenient to distinguish between these two expansion regions and are:

- The two-dimensional region characterized by the curvature of the leading characteristics from the diffraction of the one-dimensional expansion wave.
- The two-dimensional region, which developed downstream of the 90° corner and above the separation bubble. This expansion region was required to match flow conditions in the region beyond the reflected compression wave front.

6.4.2 The Reflected Compression Wave

The classification of the perturbation signal generated at the 90° corner by the diffraction of a one-dimensional expansion wave is now considered by reference to figures 6.6 and 6.7. Figure 6.7 shows a pressure profile taken along a vertical line for three instants of time, at fixed values of: $D = 40$ mm and P41 = 3, where the selection of these results was arbitrary. The origin of this vertical line coincided with the stagnation point of the separation bubble

and inidicated by a red, vertical line in figure 6.6 and therefore, to maintain consistency, the pressure profiles were obtained at a fixed location with respect to the separation bubble.

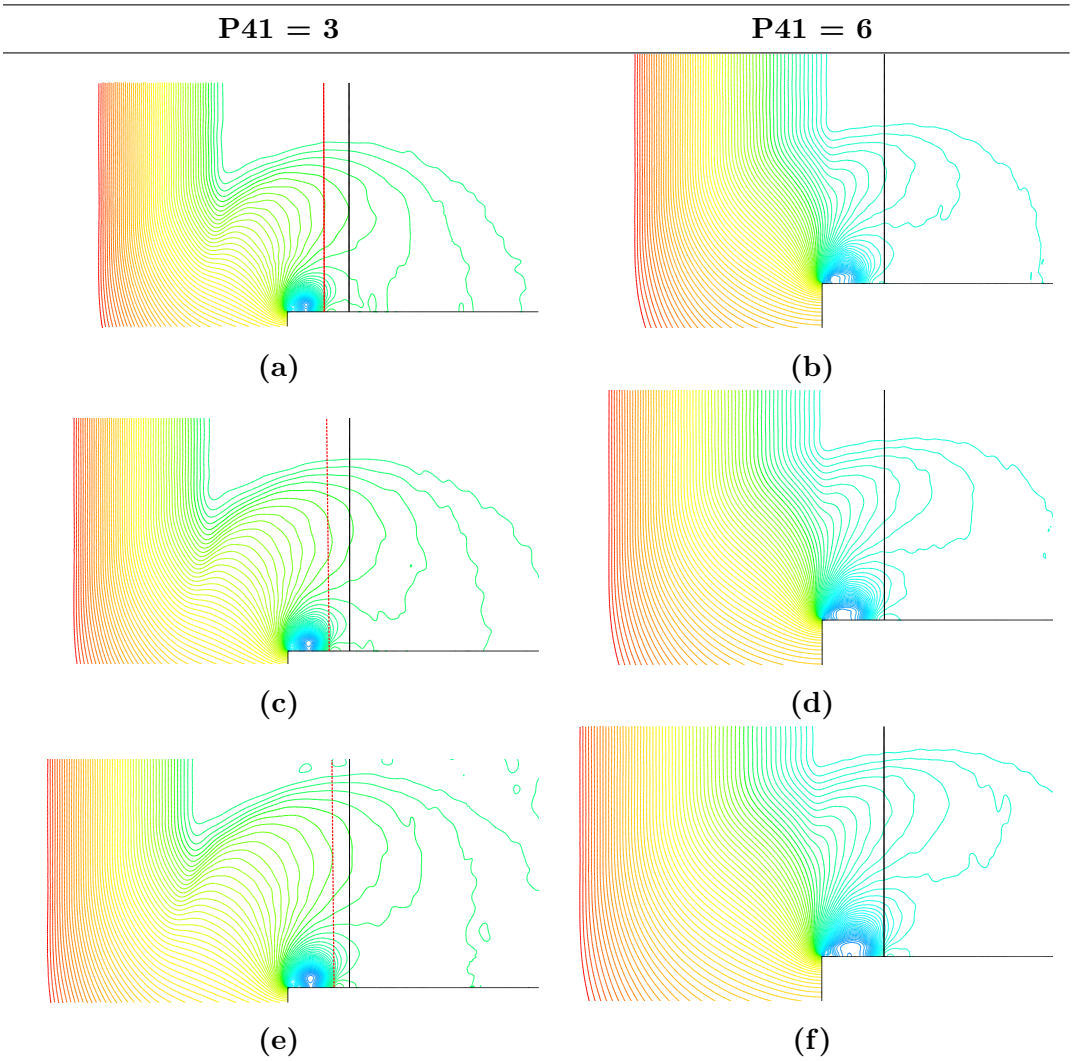


Figure 6.6: Contours of pressure for P41 = 3 and 6, $D = 40$ mm. Times, t_f (μs) **(a,b)**: 350, **(c,d)**: 400, **(e,f)**: 450.

The simulation images in figure 6.6 showed how the spatial movement of the perturbation propagated outward in a radial fashion with time. The accompanying graph appears in figure 6.7 and indicates the pressure rise across the perturbation signal at a fixed height position in the flow domain. The perturbation signal was in the process of propagating into the one-dimensional region and was shown for three instantaneous positions.

Consider the diffraction of a one-dimensional expansion wave in figure 6.4, where a plot of pressure along the direction of any characteristic in the one-dimensional region would be constant and is reflected by the horizontal line in figure 6.7. For 350 μs, the horizontal pressure curve attained an increasing magnitude until a peak and thereafter a reduction of pressure occurred. This pattern was observed at the later times of 400 and 450 μs, in figure

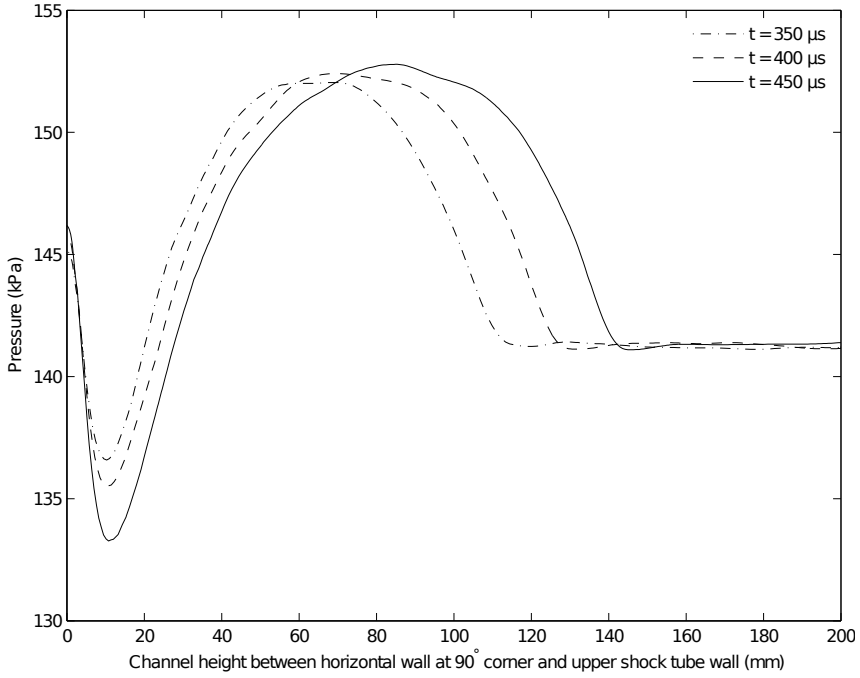


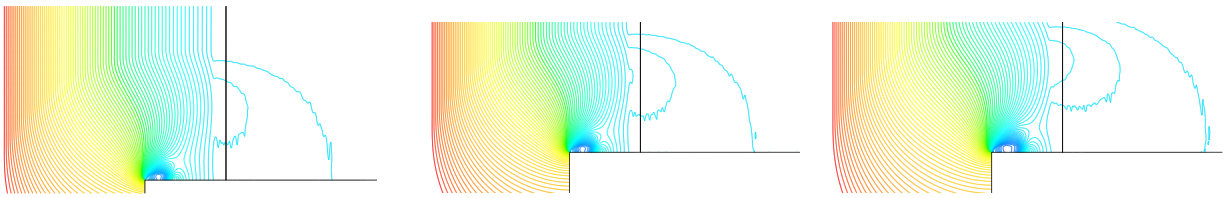
Figure 6.7: Pressure profile along shock tube channel height for P41 = 3, $D = 40$ mm and at three instances of time (μs). The channel height of 0 mm refers to the horizontal wall position of the test corner and the origin of each pressure curve coincided with the stagantion point of the primary separation bubble (on the horizontal wall).

6.7. Also, the change in pressure occurred closer towards the upper-wall of the flow domain, at increasing time. Therefore, this graph confirms that 1) the perturbation signal is a reflected compression wave that propagates outward into the one-dimensional flow in region 3, and 2) the reflected perturbation is followed by an expansion region.

An increase in the value of the independent parameters, D and P41, would generate a considerably broader incident expansion wave. This wave would require a longer duration for the reflected compression waves to propagate into the steady downstream flow. This occurred notably for P41 = 9 and $D = 70$ mm, illustrated by figure 6.8 below. However, this was not observed when variation in D was considered at the values of 0 and 10 mm, where it was found, that the reflected compression waves would steepen into a cylindrical shock wave.

6.4.3 The Steepening of The Reflected Compression Wave

The conditions for the steepening of the reflected compression waves are now explored through variation of D and P41.



(a) **(b)** **(c)**

Figure 6.8: Contours of pressure for P41 = 9, D = 70 mm. Times, t_f (μs) **(a)**: 350, **(b)**: 400, **(c)**: 450)

Figure 6.9 shows the temporal behaviour of the reflected compression waves for P41 = 3 with $D = 0$ and 10 mm. In this figure, the incident expansion wave undergoes complete diffraction at early time (by 50 μs) and was followed by the rapid formation of a cylindrical shock wave by coalescence of the reflected compression waves. A similar result was obtained for P41 = 6 and 9 with $D = 0$ and 10 mm.

For P41 = 3, a difference was noted for the cylindrical shock wave's development between $D = 0$ and 10 mm and $D = 40$ and 70 mm. This is related to the width of the expansion wave prior to diffraction. For $D = 10$ mm a narrow-width expansion wave was generated where the gradients of flow properties within the wave were steep. Values of $D = 40$ were too 'drawn out', as observed in the pressure contour plots of figure 6.6, where the gradients of flow properties within the wave are weaker.

Consider the variation of D and P41 on the development of the cylindrical shock wave, as presented in figure 6.10, for constant time of 400 μs and P41 = 3 and 6. From this figure, for P41 = 3 and 6, evidently the variation of D influenced the coalescence of the reflected compression waves into a cylindrical shock wave. This readily occurred for $D = 10$ mm where its pressure profile, shown in figure 6.11, was almost as discontinuous as a weak shock wave. The pressure profiles for $D = 40$ and 70 mm were similar to a typical one-dimensional, finite compression wave. Also, it was interesting to observe, for a fixed instant in time and P41, the instantaneous position of the leading characteristic of the simple compression wave was almost independent of D; this can be inferred from the contour plots of pressure in figure 6.9.

The pressure plots in figure 6.9 indicated sharper coalescence of the reflected compression waves in the region near the trailing characteristic of the incident expansion wave, than further downstream. This may have occurred due to the relative velocity between the mean flow and the expanding cylindrical shock wave. The mean flow (above the diffraction corner) has a significant downstream component, in the positive x- direction, whereas the cylindrical shock propagates radially outward; partly upstream and downstream.

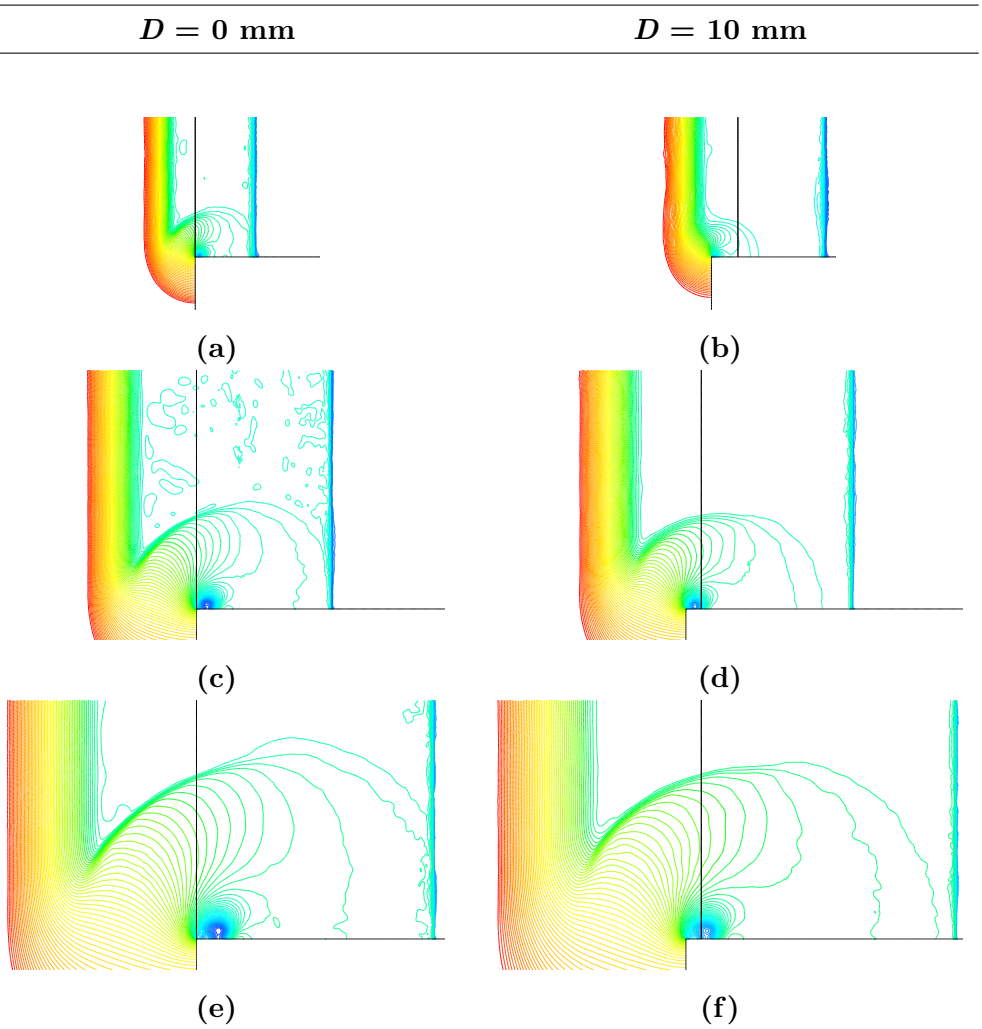


Figure 6.9: Instantaneous contours of pressure for P41 = 3, $D = 0$ and 10 mm. Times, t_f (μs) **(a,b)**: 50, **(c,d)**: 200, **(e,f)**: 350

It is concluded, that the simple compression waves generated by the diffraction of a one-dimensional expansion wave, coalesces into a cylindrical shock wave for small values of D and is independent of P41. This result was in absence of wave reflection by the reflected compression waves (or the cylindrical shock wave formed by coalescence of these reflected waves) upon the upper wall.

A combination of large values of P41 (6 and 9) and D (40 and 70 mm) would generate a broad expansion wave prior to diffraction.This would delay the formation of a cylindrical shock wave. For all results, a requirement was that P41 $<$ 10.4 i.e. subsonic flow within the one-dimensional expansion wave.

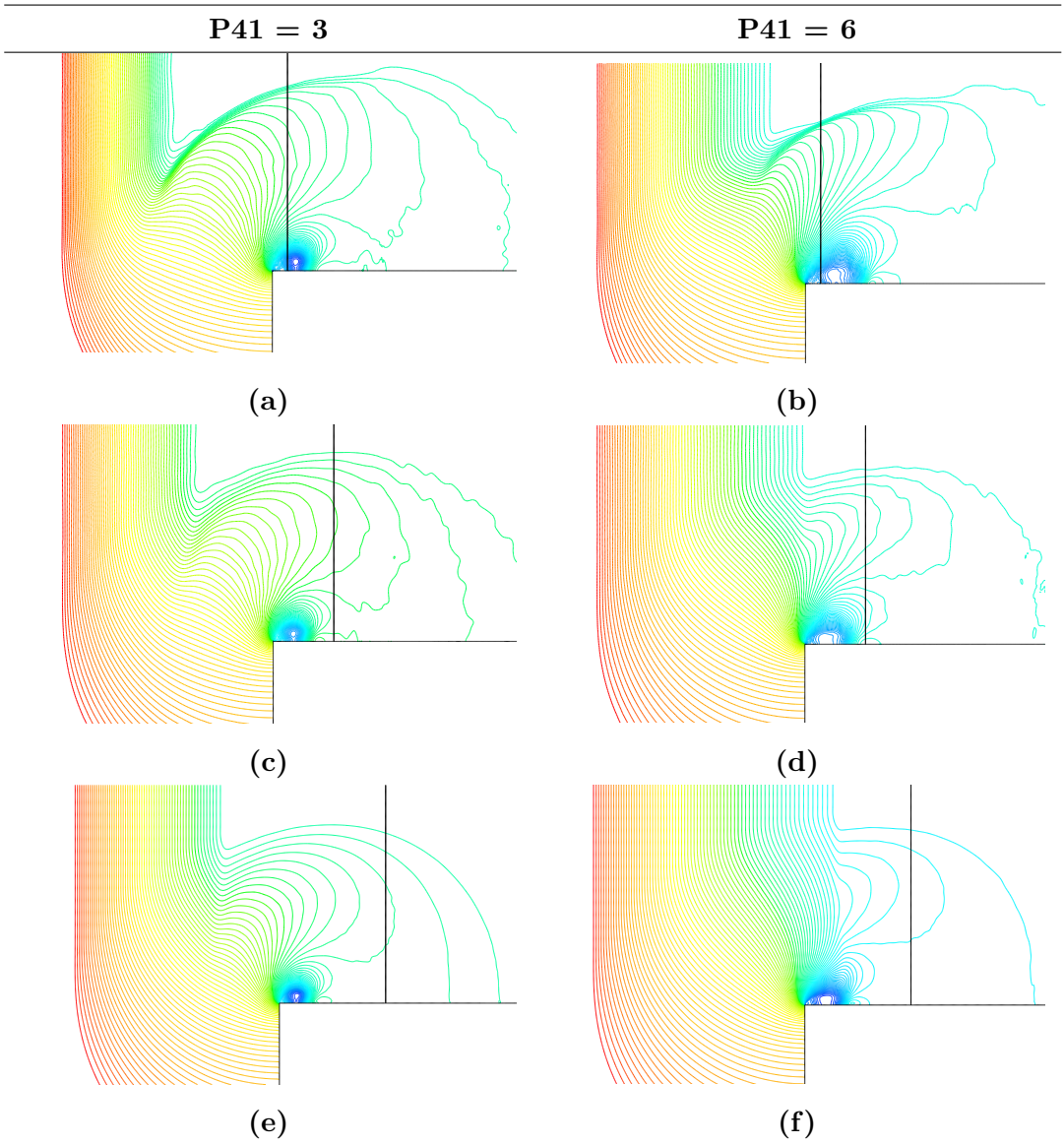
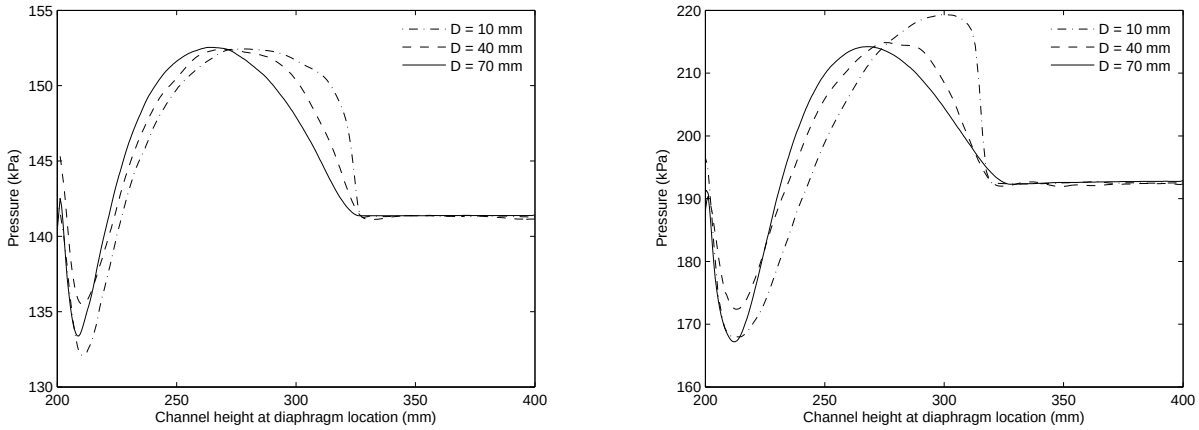


Figure 6.10: Instantaneous pressure profile, along the shock tube channel height, for P41 = 3 and 6. Time, t_f (μs) 400. D (mm): **(a,b)**: 10, **(c,d)**: 40, **(e,f)**: 70.

6.5 The Separation Bubble

The formation of the separation bubble at early time-delay is illustrated through shadowgraph images in figure 6.12, for P41 = 3.2. In this figure, for 50 and 100 μs time-delay, the flow aleady separated at the apex of the corner. At 150 μs time-delay, a vortex clearly developed with a shear layer extending downstream into the flow. The shear layer was evident of flow separation at the diffraction corner as the fluid momentum upon the vertical wall could not negotiate the diffraction corner. This layer was observed to reattach at some finite distance downstream from the diffraction corner, and formed the outer periphery of the separation bubble. The re-attachment streamline was assumed to end at a stagnation point on the

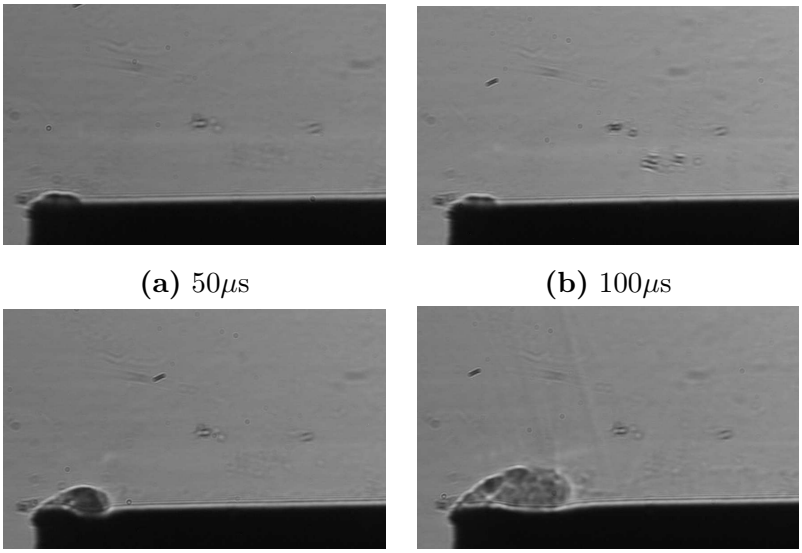
P41 = 3	P41 = 6



(a) **(b)**

Figure 6.11: Instantaneous pressure profile along shock tube channel height for P41 = 3 and 6. Time, t_f (μs) 400. D (mm) = 10, 40, and 70.

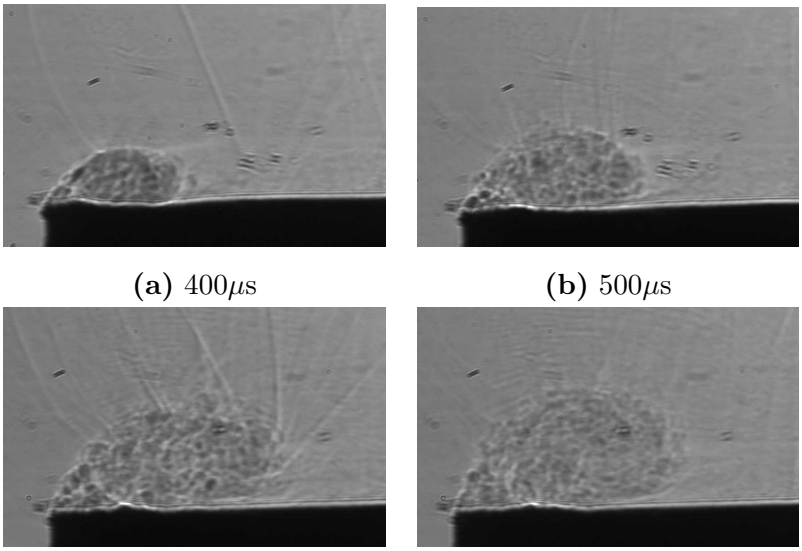
horizontal wall and is discussed later in this section. The shear layer formed the outer periphery of the separation bubble and evidently indicated flow separation. At 300 μs time-delay, the bubble remains attached to the horizontal wall and is of a larger, physical size. In section 6.3, the separation bubble was observed to rise slightly away from the horizontal wall and its internal structure appeared highly diffuse as shown in figure 6.13 for a time-delay $>$ 400 μs. This may occur due to rig dependent effects caused by wall reflections that is beyond the scope of the present study.



(a) 50μs **(b)** 100μs

(c) 150μs **(d)** 300μs

Figure 6.12: Shadowgraph images (high resolution) for P41 = 3.2, demonstrating formation of the separation bubble at early times.



(a) 400μs **(b)** 500μs

(c) 600μs **(d)** 700μs

Figure 6.13: Shadowgraph images (high resolution) for P41 = 3.2, demonstrating formation of the separation bubble at late time and rig dependent effects

In section 6.3, high resolution shadowgraph images were presented for P41 = 3.2 and 7.7. In these figures the shear layer and turbulent structure of the separation bubble were identified. Shadowgraph images for these two values of P41, are shown in figure 6.14 for a wider range of time delay-values and in absence of the separation bubble's breakdown. This figure illustrates the bubble's growth over time where, as expected, the growth was significantly larger for P41 = 7.7 than 3.2. Also, at P41 = 7.7, vortex shedding and a faint transonic shock was visible just above the shear layer for time-delay values at 300 and 350 μs, frames (g) and (h) respectively.

For P41 = 3.2 flow separation was identified upon the horizontal wall at time-delay values of 200 and 250 μs which corresponded to frames (a) and (b) in figure 6.14. Flow separation was not easily identified at higher values of P41 due to relatively steep density gradients within the separation bubble as observed for P41 = 7.7 in frames (e-h). Intuitively, a viscous vortex should exist between the origin of the shear layer and the point of flow separation upon the horizontal wall. Time-delay values covering the effects of rig dependency for P41 = 3.2 and 7.7 that appear in figure 6.14, are included in Appendix C, section C.1.2.2.

In figure 6.14 (f), tiny shocklets identified where the shear layer just separated at the diffraction corner. These shocklets, identified as short, white lines emanated a finite distance into the flow field from ridges in the shear layer. These ridges arose by a wavy-like structure upon the shear layer indication of an instability. Shocklets were not observed in the simulation data, since the shear layer profile was resolved as a smoothly contoured surface with no ridges or bumps.

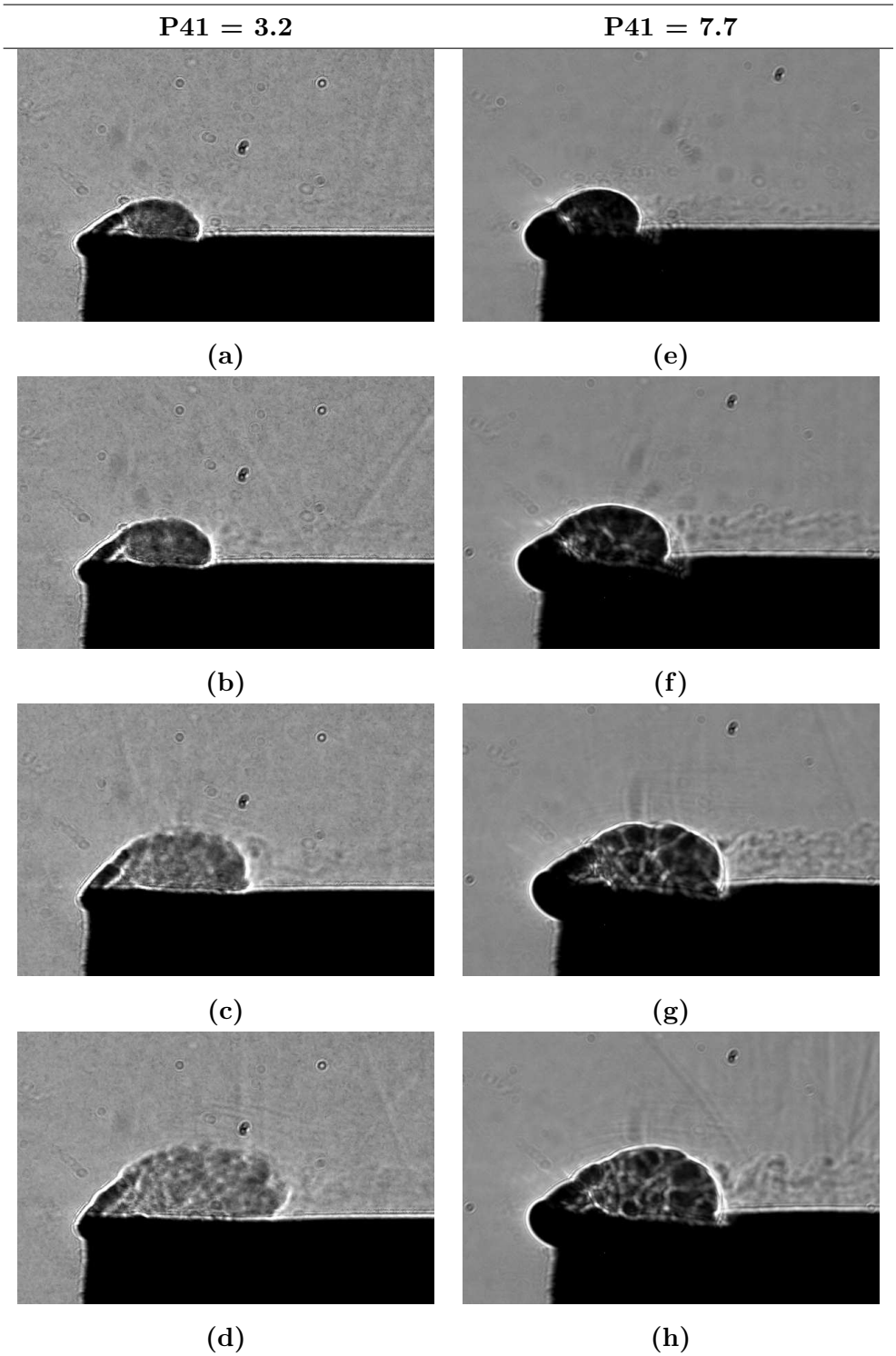


Figure 6.14: Shadowgraph images (high resolution) for P41 = 3.2 and 7.7 to demonstrate features of the separation bubble prior to rig dependent effects. Time-delay values (μs): **(a,e)** 200, **(b,f)** 250, **(c,g)** 300, **(d,h)** 350.

It could not be ascertained if the shocklets was a localized effect on the shear layer or spanned the depth of the test-section. The localized effect may occur if the transverse direction (between the viewing windows) of the separation bubble developed variable, cross-sectional geometry. This variation would occur due to various perturbation sources which were identified

as, but not limited to: manufacturing imperfection of the 90° corner test-piece, transverse waves interacting with the near-corner flow structure or slight vibrations from the diaphragm bursting process. Oblique imaging may be required to visualize if any variation exists in the depth direction of the separation bubble, at the diffraction corner and is an area for further investigation.

6.5.1 The Viscous Vortex and the Near-Corner Flow Structure

The boundary layer flow, up the vertical wall of the 90° corner was observed to separate near the apex at 150 μs time-delay, in figure 6.12. In shock diffraction over a 90° backward facing step, the separation of the boundary layer at the diffraction corner would roll-up into a viscous vortex, experimentally shown by Skews [1967] and computationally resolved by Hillier [1991] and others. In the current case, the separation of the boundary layer against the vertical wall was not visualized in the experimentation and some-what resolved with the simulation (Navier-stokes solver with Menters SST k-ω solver). Consider simulation results that mimicked the experimentation as shown in figure 6.15, for a vector plot of velocity magnitude at P41 = 3.2 and 7.7.

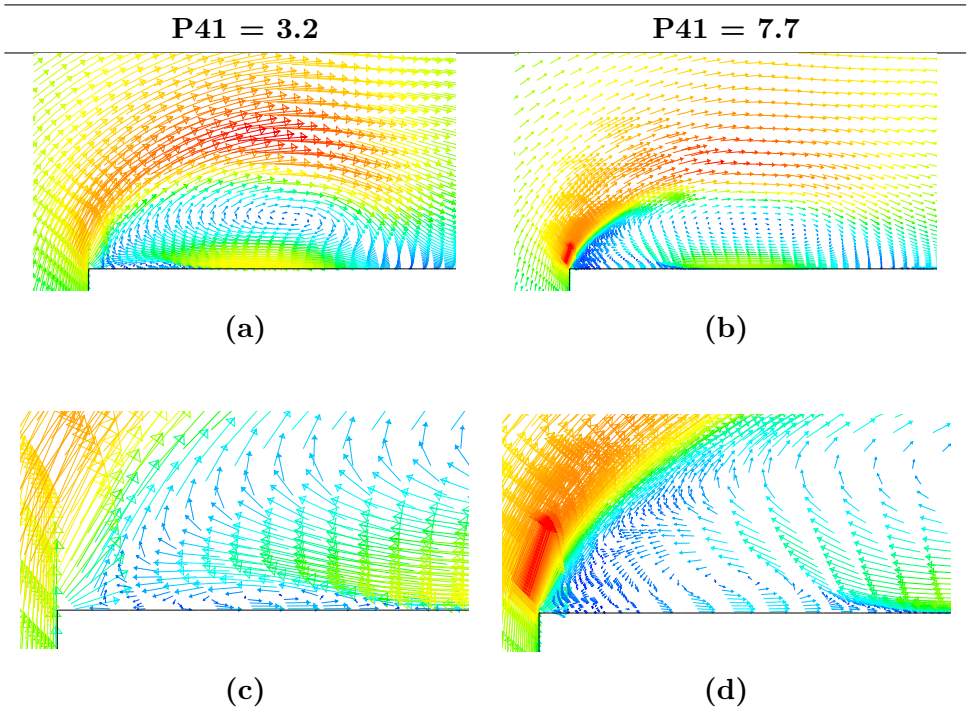


Figure 6.15: Velocity vector plot illustrating the flow structure near the diffraction corner using Menters SST k-ω solver for P41 = 3.2 and 7.7 at 320 μs. Zoomed-in images are inlcuded in the bottom row. (D = 83 mm).

In figure 6.15, frame (a) for P41 = 3.2, the simulation predicted the existence of a *secondary separation bubble* containing circulatory flow (secondary vortex). This secondary separation

bubble was embedded within the primary separation bubble and developed near to the apex of the corner. This was experimentally identified for P41 = 3.2 in figure 6.14, at time-delay values of 200 and 250 μs. Frame (b), of figure 6.15, zoomed in at diffraction corner illustrated a number of mini-vortices observed close to the diffraction corner. However, in this figure for P41 = 7.7 and frame's (c) and (d), the simulation resolved the secondary separation bubble whereas mini-vortices where found not resolved. Perhaps, a higher mesh resolution near the diffraction corner, would resolve the viscous vortex and mini-vortices and/or employing a simulation code to adequately resolve the turbulence scales that was experimentally observed.

Euler simulations for the same P41 values and geometry as in figure 6.15 did not resolve any flow separation leading to the development of a secondary separation bubble upon the horizontal wall nor any mini vortex structures near the diffraction corner within the primary separation bubble. It was then surmised that the secondary separation bubble and mini vortex structures identified with the Navier-stokes solver, are due to viscous effects of the flow near the diffraction corner. We now consider simulation results for the the near-wall flow at the diffraction corner for early time.

At early time, shown in figure 6.16, it was observed that flow separation upon the horizontal wall was only resolved for P41 = 7.7 and was confined to a region close to the diffraction corner and the mini-vortex structures were not well-resolved for P41 = 3.2 and 7.7. A possible reason may be that the separated flow exists close to the wall at early time and would require a finer boundary layer mesh to resolve this feature using a Navier-stokes solver. The absence of the mini-vortex structures in the simulation results of this figure figure, at both values of P41, may indicate its development is dependent on the extent of flow separation upon the horizontal wall. Also, the turbulent circulatory flow with in the primary separation bubble, identified experimentally in the shadowgraph images of figure 6.14, may cause rapid dissipation of these mini vortex structures. A simulation code may not adequately resolve the turbulent flow structures identified experimentally without resort to LES (Large Eddy Simulation) or DNS) Direct Numerical Simulation) which would be impractical at present due to time and computational resources. Perhaps, performing the experimentation with a lower initial density to reduce the flow Reynolds number may yield a clearer identification of the possible existence of the these mini-vortex structures. A large scale experimental study would result in an increased length-scale and therefore a higher Reynolds number which may not be suitable in an attempt to visualize these mini vortices.

The shadowgraph images in figure 6.14, gave an indication of high density gradients at the diffraction corner which may mask the presence of the separated boundary layer flow from the vertical wall. These shadowgraph images also showed the presence of a turbulent flow field within the primary separation bubble which may promote diffusion of the separated boundary layer flow near the diffraction corner. From the simulation results in figure 6.15 (b), the mini

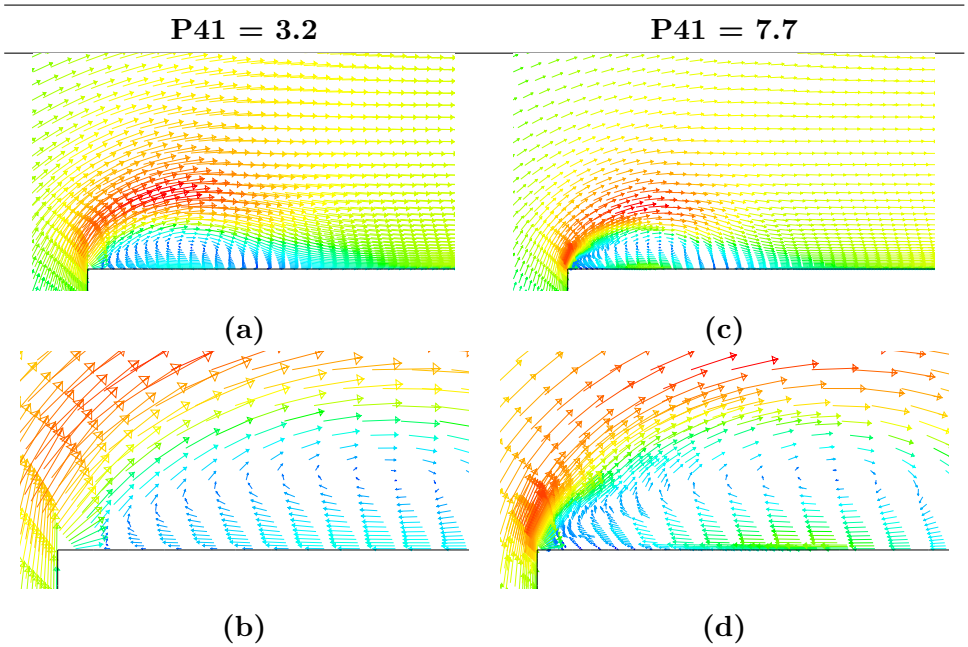


Figure 6.16: Velocity vector plot illustrating the flow structure near the diffraction corner using Menters SST k-ω solver for P41 = 3.2 and 7.7 at 200 μs. Zoomed-in images are inlcuded in the bottom row. $D = 83$ mm.

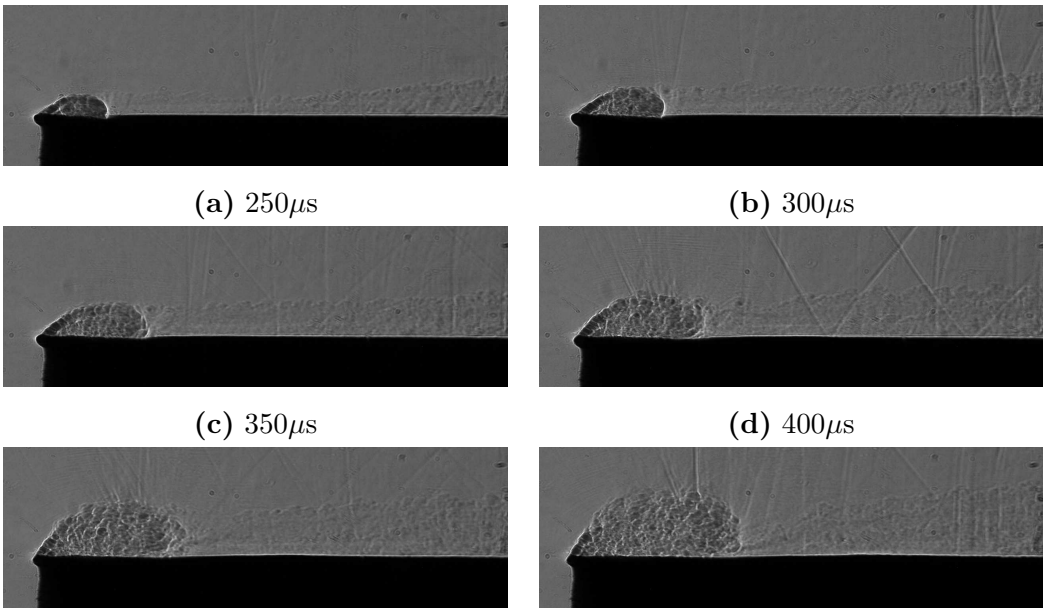
vortices maybe attributed to the structure observed in the shadowgraph images and may have led to a turbulent flow field within the primary separation bubble.

We believe the boundary layer flow upon the vertical wall should separate and would interact, in some fashion, with the near-corner flow, contained within the primary separation bubble. However the nature of this separation could not be identified.

6.5.2 Shear Layer Instability

The shear layer and 'wake' region was identified in section 6.3 using shadowgraph images for P41 = 3.2 and 7.7. Figure 6.14 in section 6.5, illustrated the flow field near the diffraction corner for time-delay values before the onset of rig-dependent effects. In this figure, it was observed for $t_f \leq 350$ μs time-delay, that the shear layer maintained a definite and smoothly curved profile over the upper periphery of the separation bubble which should continue until the stagnation point. The same result was obtained using schlieren imaging with a horizontal knife-edge at 350 μs time-delay in figure 6.18. This smooth profile was present upto a certain instant of time after which the shear layer developed an instability and which was similar to that observed in shock diffraction and experimentally discussed in Skews et al. [2012]. Also, in the shadowgraph images some structure on the shear layer was visible for P41 = 3.2 whereas higher clarity of this structure was achieved for P41 = 6.5 which appears in figure

6.17. The shear layer instability and 'wake' region was not identified nor resolved in the simulations (Navier-stokes solver with Menter's SST k-ω solver).



(a) 250μs **(b)** 300μs

(c) 350μs **(d)** 400μs

(e) 450μs **(f)** 500μs

Figure 6.17: Shadowgraph images for P41 = 6.5 emphasizing the wake region and vortex shedding. ($D = 83$ mm).

In figure 6.17, at 300 μs time-delay, some structure was observed to develop in the shear layer prior to which the shear layer had a continuous smooth profile. Also, the separation bubble was firmly affixed to the horizontal wall where the profile of the shear layer at the rear of the separation bubble and up to the stagnation point was smooth, despite the presence of shear layer instability on the upper periphery of the bubble. The shear layer instability was further evident at 350 and 400 μs time-delay where the rear portion of the separation bubble was somewhat diffused at the latter time-delay. By 450-500 μs time-delay, the definition of the shear layer and the smooth contoured surface of the separation bubble appeared highly diffused. Based on the analysis to establish the onset of rig-dependent effects in the high-resolution shadowgraph images, the diffused periphery of the separation bubble was attributed to the arrival of reflected waves at the diffraction corner for 450 μs. This strongly indicates that the shear layer instability can not be attributed to rig-dependency (which arose by wall-reflections) while the rear portion of the separation bubble maintained a smooth contour.

6.5.3 Vortex Shedding

In addition to the shear layer instability, vortex shedding and a wake region are evident in figure 6.17. However, at P41 = 3.2, in figure 6.14, the visibility of the shed vortices and wake

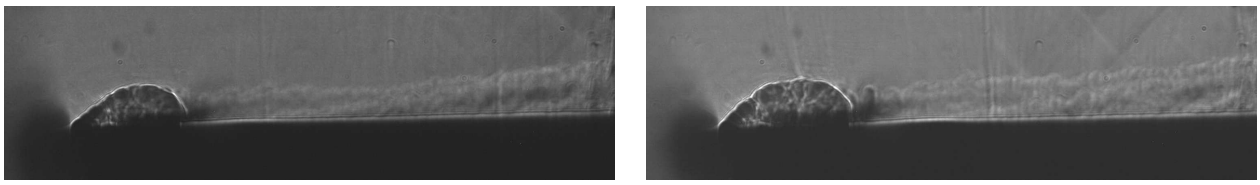
are faint relative to P41 = 6.5. This may be due to lower density gradients over the periphery of the separation bubble associated at P41 = 3.2.

The vortex shedding was evident, for P41 = 6.5, at 300 μs time-delay in figure 6.17 (b) and seemed to coincide with shear layer instability. At this time-delay, a distinct pattern of three vortices were observed to convect downstream. At later time-delay, these shed vortices would dissipate in the turbulent downstream wake. At 250 μs time-delay, no distinct pattern of vortices was observed in this figure where the shear layer appeared fairly stable. Shed vortices may be present at time-delay $>$ 300 μs where the shed vortices may be too weak and thus not easily visualized. In this figure, it was observed that the outer-flow immediately beyond the periphery of the separation bubble would continue downstream and interact with the wake flow where a wavy structure appeared as the boundary.

Consider figure 6.14 (h), where, for P41 = 7.7, the shed vortices are clearly visible for 300 and 350 μs time-delay with some structure present in the shear layer. The shed vortices seemed to originate from the shear layer at the rear-end of the separation bubble and slightly downward from the bubble's upper periphery.

6.5.4 The Wake Region

In all the shadowgraph images presented thus far, a wake region was evident immediately downstream of the separation bubble. It was found, through schlieren imaging with a horizontal knife-edge, that certain flow structures were better resolved than the shadowgraph results. These schlieren results are shown in figure 6.18 for P41 = 6.5 and time-delay values of 300 and 350 μs.



(a) **(b)**

Figure 6.18: Schlieren imaging with a horizontal knife-edge highlighting structure in the wake region and shear layer for P41 = 6.5 and time-delay (μs): 300 **(a)**, 350 **(b)**, D = 83 mm.

In figure 6.18, the wake region seemed to comprise of two distinct layers. The lower *first layer* was observed to develop linearly on the horizontal wall at a finite distance downstream of the separation bubble and appeared embedded within the *second layer*. Shed vortices are visible in figure 6.18 (b) just off the upper rear-end of the separation bubble. These shed vortices were identified in the shadowgraph result for figure 6.17 (c). From the shadowgraph

results, it is postulated that the shed vortices arose from the instability of the shear layer and, that another part of the shear layer continues toward the stagnation point. The shear layer at the stagnation point would feed the primary vortex in the separation bubble and partly continue downstream. Therefore, the first layer could be due to the turbulent boundary layer continuing downstream whereas the second layer could be due to the shear layer emerging off the upper rear-end of the separation bubble.

6.5.5 Characterizing the Separation Bubble

The separation bubble (primary) was characterized by the formation of a shear layer at the diffraction corner and its re-attachment downstream on the horizontal wall. As discussed in section 6.5, the shear layer formed the separation bubble's outer periphery and, enclosed a region of circulatory fluid that was identified as the primary vortex, a secondary separation bubble with its secondary vortex and a number of mini-vortices near the diffraction corner. However the nature of the viscous vortex could not be established.

The stagnation point was found to be a convenient geometrical variable to characterize the growth of the primary separation bubble with variation of the independent parameters D and P41, in both, temporal and spatial terms. It was somewhat less clear to consider the *height* or *width* of the separation bubble as the geometrical variable, since their location was not adequately certain in the experiment or simulation results. The definition of the stagnation point was given in section 6.3.

A particular trend was observed in terms of the bubbles growth with respect to the stagnation point. The results obtained were then organised as follows:

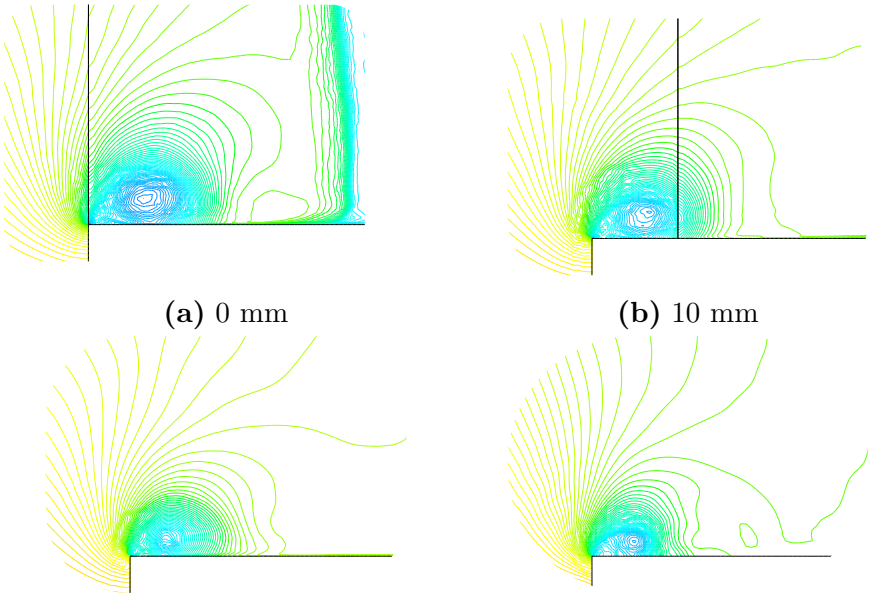
- Considering the effect of various values of D with fixed, discrete values of P41 where the bubble's growth was observed for changes in D.
- Considering the effect of various values of P41 with fixed, discrete values of D where the bubble's growth was observed for changes in P41. This was accomplished by observing the movement of the stagnation point upon the horizontal wall.

Comparison of results for various values of D with fixed, discrete values of P41

Results were considered for P41 = 3, 6 and 9; shown respectively in figures 6.19, 6.20, and 6.21. The results shown are for an instantaneous position at 200 μs, which were similar at other times in absence of rig dependent effects.

Consider the frames for P41 = 3, in figure 6.19. The largest bubble shape was obtained for $D = 0$ mm, frame (a), where the separation bubble developed in absence of a diffracted incident expansion wave. In the latter frames, for $D = 10$, 40, and 70 mm, the bubble shape progressively reduced in size. Therefore, the presence of a finite width incident expansion wave at the corner evidently influences the physical size of the separation bubble. This result was observed for P41 = 6 and 9, which can be noted in their respective figures.

For a fixed time (t_f), the general trend noted was a reduction in the physical size of the separation bubble for an increase in the distance between the diaphragm location and the 90° corner.



(a) 0 mm **(b)** 10 mm

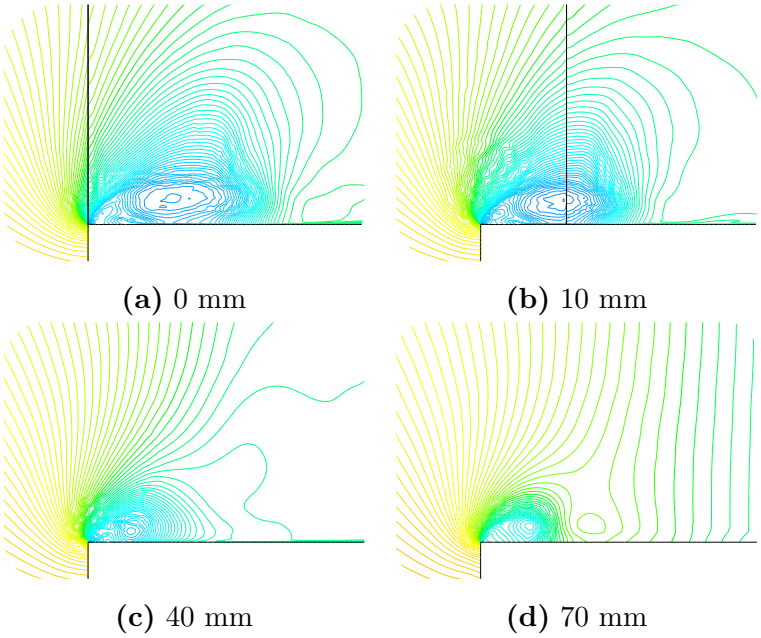
(c) 40 mm **(d)** 70 mm

Figure 6.19: Density contours for P41 = 3 and time, $t_f = 200$ μs.

The shape of the separation bubble appeared roughly circular for P41 = 3 and increasingly elliptic for P41 = 6 and 9. The bubble's shape, is believed, to have a strong influence on the acceleration of the flow near the, upper, contoured surface. However, the flow field near the bubble upper surface is two-dimensional and unsteady. The flow physics to explore this statement is an area for further research.

Comparison of results for fixed, discrete values of D, with various values of P41

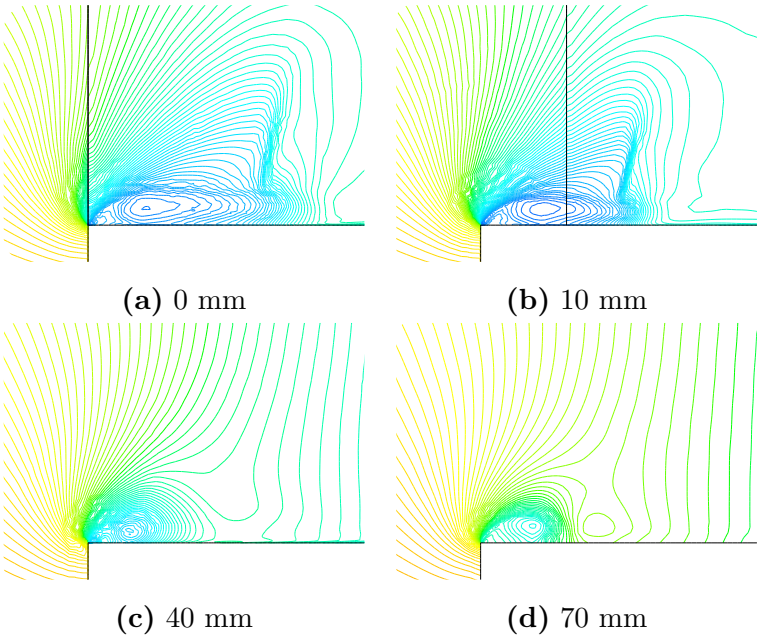
We now consider the growth rate of the separation bubble with P41, which was parametrized by the position of the the diaphragm from the 90° corner. The maximum time (t_f) considered was ≈ 320 μs. These plots are shown individually for $D = 10$, 40, and 70 mm, in the following figures:



(a) 0 mm **(b)** 10 mm

(c) 40 mm **(d)** 70 mm

Figure 6.20: Density contours for P41 = 6 and time, t_f = 200 μs.



(a) 0 mm **(b)** 10 mm

(c) 40 mm **(d)** 70 mm

Figure 6.21: Density contours for P41 = 9 and time, t_f = 200 μs.

The line plots, in figures 6.22, 6.23, and 6.24 illustrates the movement of the stagnation point on the horizontal wall. From these figures it was observed, in absence of rig-dependent effects, that the growth rate of the separation bubble is approximately linear and with a positive gradient.

For D = 10 mm, in figure 6.22, the curves for P41 = 6 and 9 appeared similar in slope, however, the slope was significantly less steep for P41 = 3. At larger values of D (40 and 70

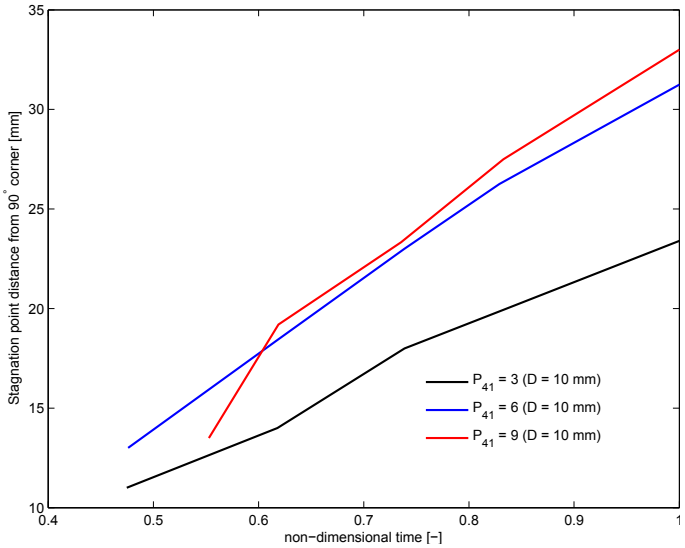


Figure 6.22: Horizontal movement of the stagnation point from the 90° corner for P41 = 3, 6, 9 and $D = 10$ mm.

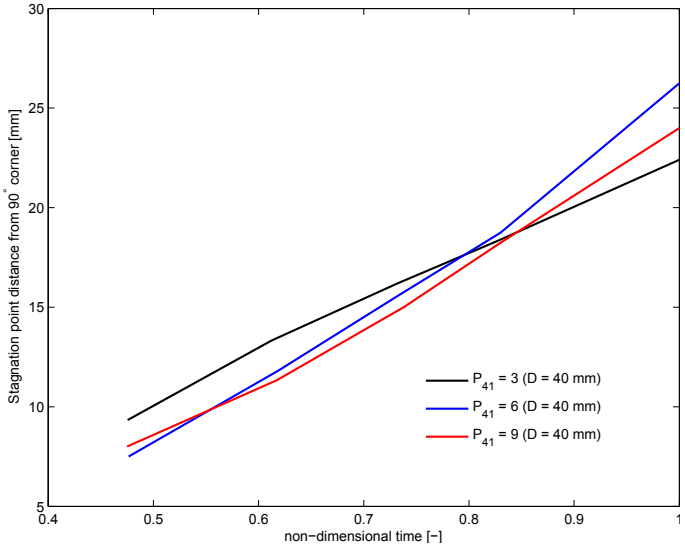


Figure 6.23: Horizontal movement of the stagnation point from the 90° corner for P41 = 3, 6, 9 and $D = 40$ mm

mm) in figures 6.23 and 6.24, respectively, the slope of the curves collapsed onto a similar path.

It was concluded that, for *increasing* values of D, the growth rate of the separation bubble based on the horizontal movement of the stagnation point would *progressively* become independent of P41.

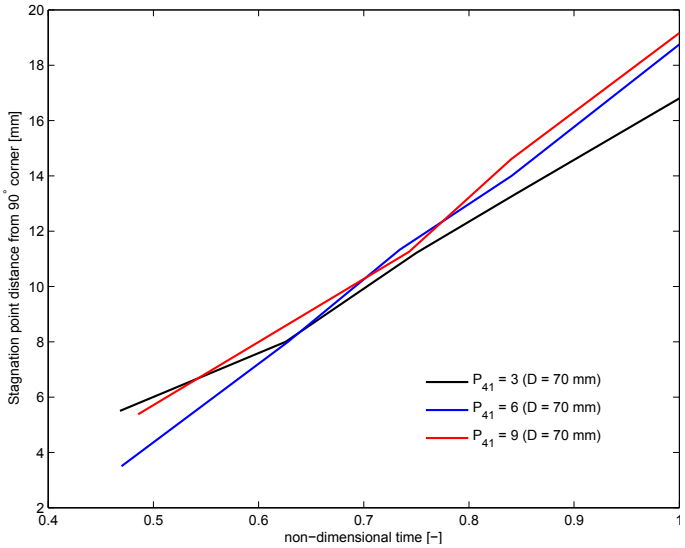


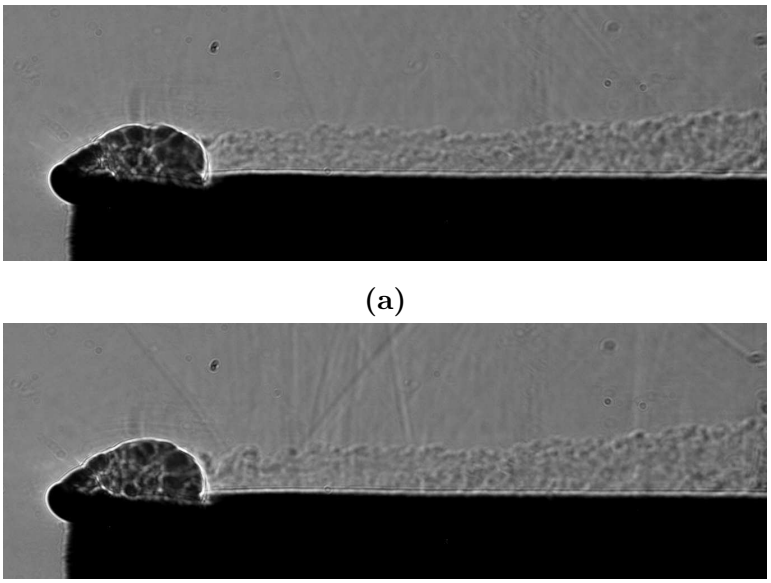
Figure 6.24: Horizontal movement of the stagnation point from the 90° corner for P41 = 3, 6, 9 and $D = 70$ mm

6.6 The Oblique and Re-Compression Shock

The influence of the separation bubble's curvature on the nearby flow field, was established in section 6.5 and is now further explored in terms of the shock. The bubble's curvature caused acceleration of the nearby, oncoming flow which led to a reduction of pressure, (including temperature, and density) above the separation bubble. This flow acceleration was due to the two-dimensional expansion region above the separation bubble as identified and discussed in section 6.4. A shock was found, through experiment and simulation, under certain conditions, to develop at the rear-end of the separation bubble. Prior to the shocks development, a compression may exist. It was believed that this shock was required to match, immediate, downstream flow conditions.

Experimentally, the high-resolution shadowgraph images for P41 = 7.7, first presented in section 6.5, gave a strong indication of the existence of this shock, identified at time-delay's of 300 and 350 μs. These two shadowgraph images are repeated here for convenience, in figure 6.25. From section 6.3, rig dependent effects that arose from wall reflections was characterized by a significant large scale breakdown of the separation bubble. This was not evident at these two time-delay values since the growth of the separation bubble, as observed in figure 6.14, was slight. This shock was not identified for P41 < 7.7 in the experimentation using both shadowgraph and schlieren imaging. The high-speed imaging did not resolve this shock perhaps due to the low resolution (0.125 MP and 60 000 FPS). Through simulation, discussed in section 6.6.4, this shock was identified as an *oblique shock* and the simulation

results are presented for time-delay values up to 600 μs and in absence of rig dependent effects.



(a)

(b)

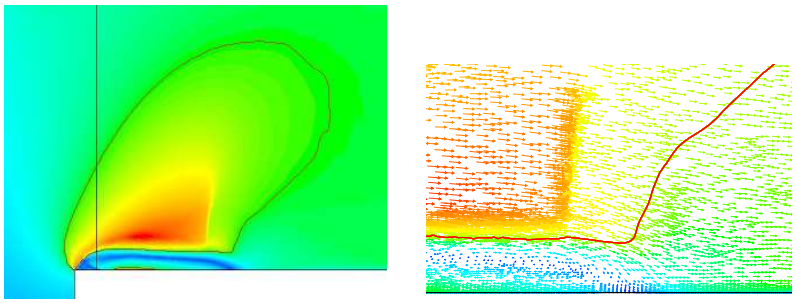
Figure 6.25: Shadowgraph images to highlight the strong indication of the shock positioned towards the rear of above the separation bubble; identified for P41 = 7.7 and time-delay (μs): 300 (**a**) and 350 (**b**)

6.6.1 Identification of the Oblique Shock

The nature of the shock whose existence was identified experimentally in figure 6.25, was established by considering the angle of the flow relative to this shock. Figure 6.26, illustrates a simulation image of this shock where the solid red line traced a boundary of Mach 1 which enclosed a region of supersonic flow and termed the *supersonic region*.

From figure 6.26, frame (a) it was evident that the post shock flow was not subsonic since the flow, immediately downstream of the shock, was contained within the supersonic region. Another reason considered the flow direction indicated by the velocity vectors in frame (b), a zoomed-in image of the flood-plot in frame (a). Here, the post shock flow direction was at some finite angle to the shock; contrast to the upstream flow being almost normal to the shock. The angled orientation of the shock relative to the flow direction was fairly discernible for P41 = 9. Also, there was speculation that some curvature exists towards the base of the shock which was observed at P41 > 9, faintly observable in frame (b). This base curvature was visible for the results presented in section 6.7.

It was concluded that the shock was of an oblique type and forward-facing to the oncoming flow. Also, in this figure, it can be seen that the velocity vectors of the primary vortex near the upper periphery of the separation bubble appeared not to be located within the supersonic region. These velocity vectors are located just below the lower boundary of the supersonic region.



(a) **(b)**

Figure 6.26: Vector plot of velocity magnitude to classify the type of shock. The selected conditions found to favourably produce this shock are: P41 = 9, D = 10 mm, and t_f = 600 μs.

6.6.2 Evolution of the Supersonic Region

The general evolution of the flow field at the diffraction corner, with emphasis on the supersonic region, the oblique shock, and the compression fan is now considered for P41 = 3, 6, and 9 and at relevant values of D. The section on Characterizing the Separation Bubble in section 6.5.5 only considered the shape and growth of the bubble as functions of P41 and D.

Simulation Results for P41 = 3

Figure 6.27 illustrates contours of Mach number for D = 0 and 40 mm, for 100-300 μs. At these early times, a supersonic region, above the separation bubble was evident at D = 0 mm, for figure 6.27 (c) at 300 μs.In this figure at these early times, no supersonic region was observed at D = 40 mm, eviden by the Mach number values given for t_f = 300 μs.

The evolution of the flow field with respect to the supersonic region was then considered at later times: 400−600 μs and shown in figure 6.28. From this figure, the supersonic region and the bubble grew larger with time and seemed somewhat similar in shape and size. This was observed to occur at all values of D, where 0 and 40 mm was selected for the results at P41 = 3. There appeared a supersonic region within the separation bubble at these later times and is discussed in section 6.6.5. At these times in this figure, the flow separation upon

the horizontal wall is clear including a second separation bubble. This was considered in the Near Corner Flow Structure in section 6.5.1.

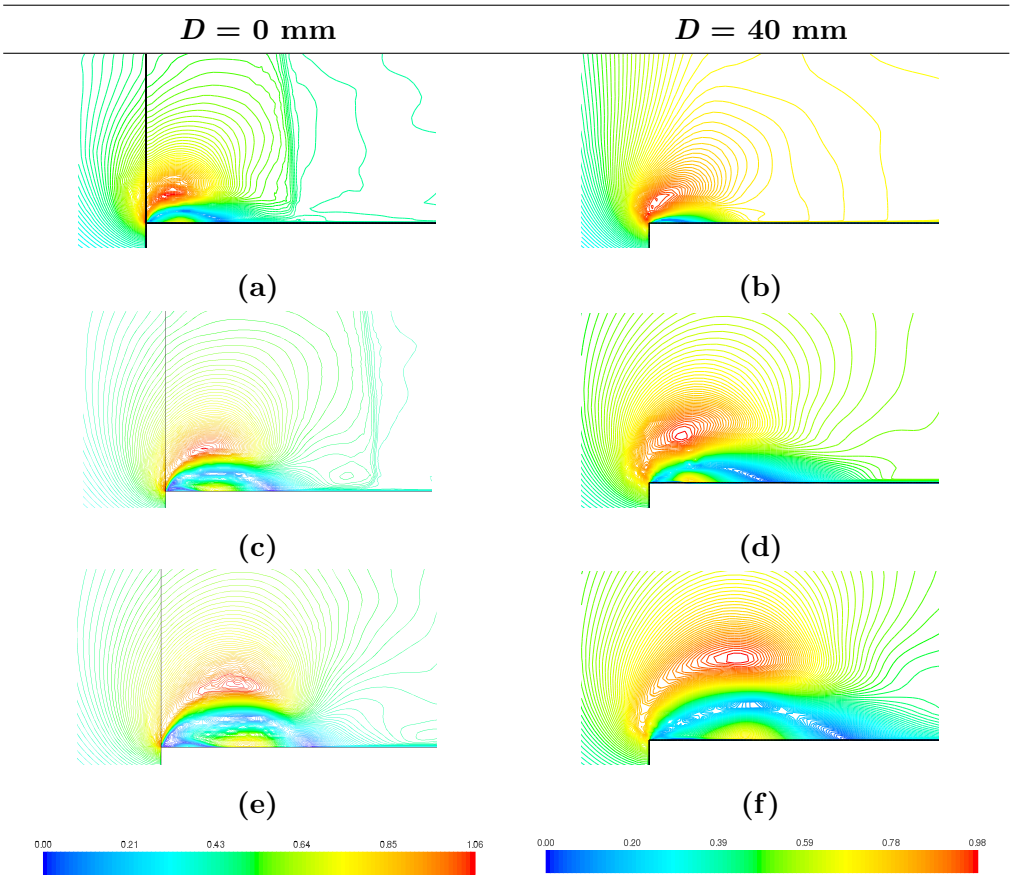


Figure 6.27: Mach number contours for P41 = 3 and D = 0 and 40 mm. Simulation times, t_f (μs): **(a, b)** 100, **(c, d)** 200, **(e, f)** 300.

Simulation Results for P41 = 6 and 9

Results are now considered, for P41 = 6 and 9, and D at 10 and 40 mm, for up-to 300 μs. Simulation results for D= 10 mm are shown in figure 6.29 and for D = 40 mm, in figure 6.30.

The supersonic region was observed to develop at early times (100 μs) for P41 = 6 and 9, and for D = 10 mm. This result appeared in frames (a) and (c) respectively, in figure 6.29. However, at D = 40 mm, the supersonic region developed at a slightly later time of 200 μs, shown in figure 6.30 (b).

The trend observed was: the supersonic region developed earlier for D = 0 or 10 mm, than D = 40 or 70 mm. For fixed values of P41, the effect of increasing D, was to delay the development of the supersonic region.

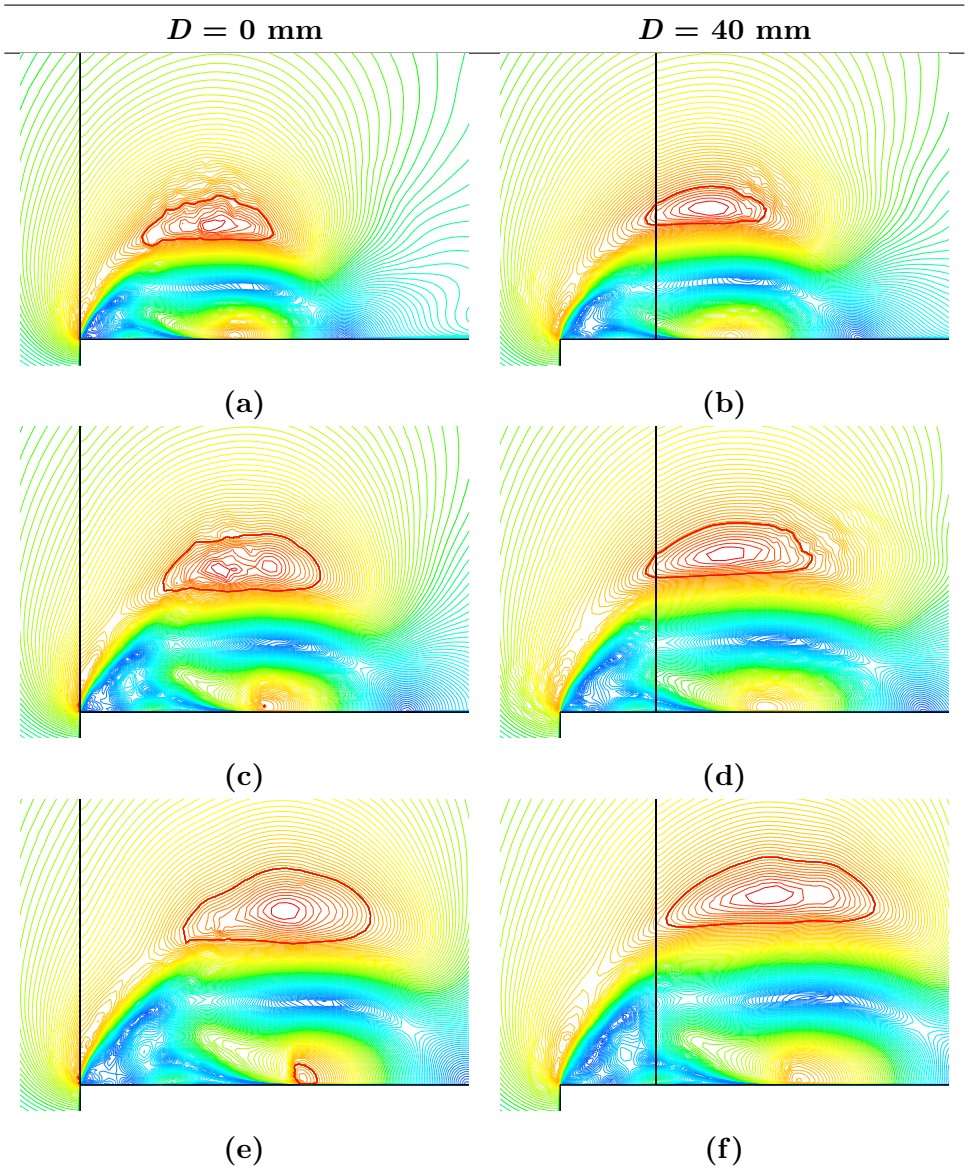


Figure 6.28: Mach number contours for P41 = 3 and D = 0 and 40 mm. Simulation times (μs): **(a, b)** 400, **(c, d)** 500, **(e, f)** 600.

The supersonic region was seen to consist of a compression fan and an oblique shock where the shock was evident for frame's (e) and (f) in figure 6.29; for P41 = 9 and D = 10 mm. Both of these flow features extended a finite height into the unsteady flow field above the upper periphery of the separation bubble.

The results in this section, for the development of the supersonic region as a function of P41 and D, did not apply to the development of the oblique shock as a function of these two independent parameters, which is discussed later in sub-section 6.6.4.

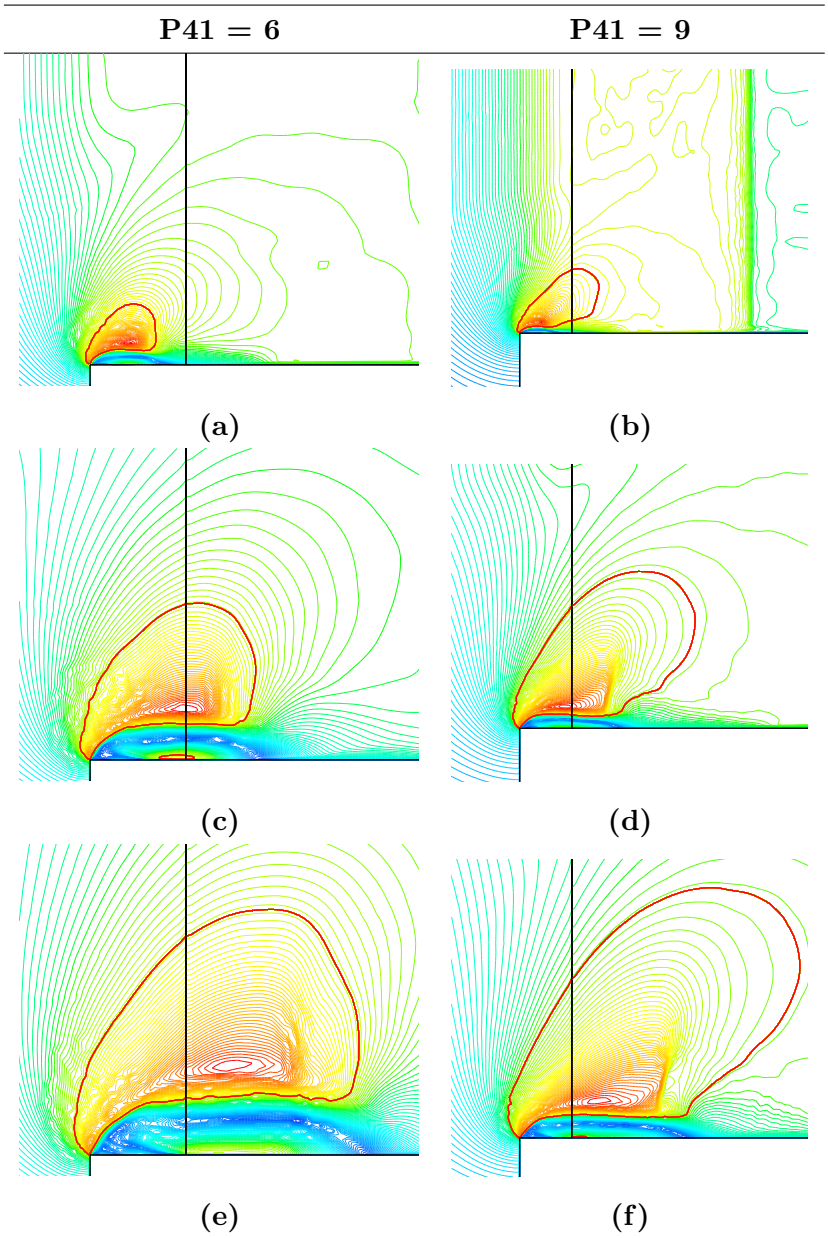


Figure 6.29: Mach number contours for P41 = 6 and 9 for D = 10 mm. Simulation times (μs): **(a, b)** 100, **(c, d)** 200, **(e, f)** 300. Results for P41 = 9 are slightly zoomed-in.

6.6.3 Shock-Free Transition from Super- to Sub-Sonic Flow

Through simulation results, it was observed that the change in flow properties (velocity magnitude and temperature), in the region near the upper periphery of the (primary) separation bubble led to the attainment of supersonic flow. The absolute Mach number for the flow in this region varied from weak transonic to strong supersonic speeds.

Figure 6.31 illustrates contours of Mach number for P41 = 3 at various values of D, for t_f = 600 μs. Clearly, the flow near the upper periphery of the separation bubble expanded

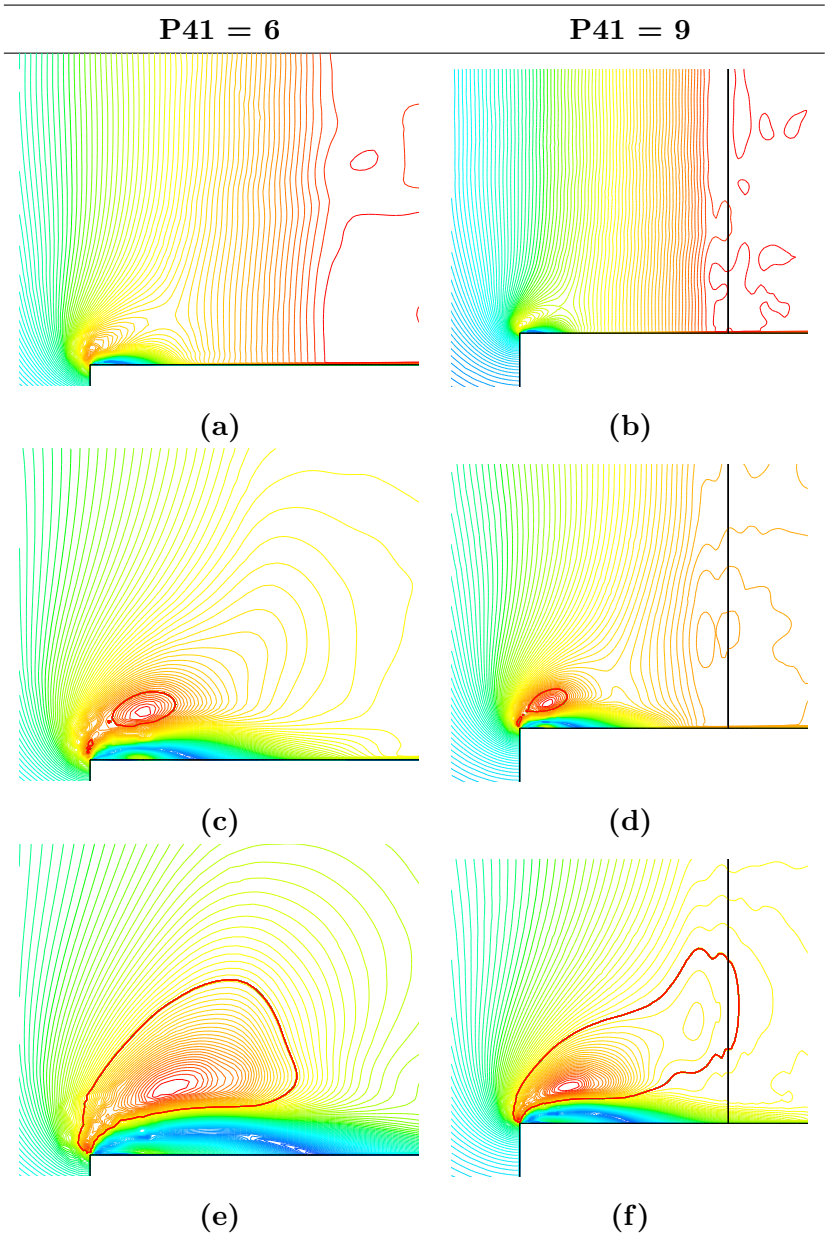
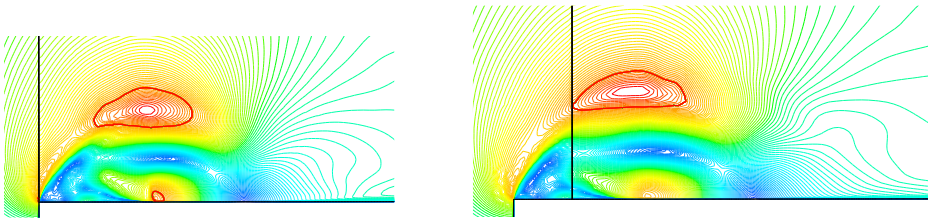
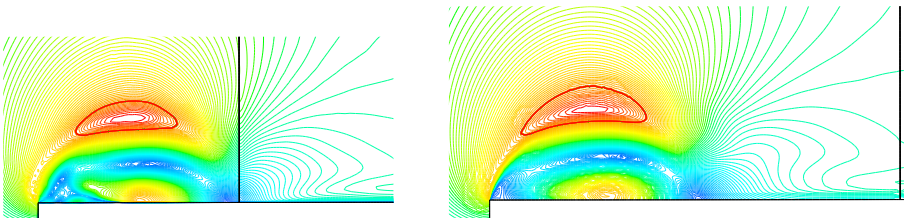


Figure 6.30: Mach number contours for P41 = 6 and 9 for $D = 40$ mm. Simulation times (μs): **(a, b)** 100, **(c, d)** 200, **(e, f)** 300. Results for P41 = 9, are slightly zoomed-in.

supersonically and then decelerated back to sub-sonic speeds in absence of a shock. This phenomenon was observed for a case of shock diffraction over a 90° corner by Kleine et al. [2003]. The roughly circular shape of the separation bubble may have effected a suitable absolute Mach number gradient within the sonic-region for the flow to undergo pressure recovery in absence of a shock. However, other reasons for no shock development may exist given that the flow field, which contains the supersonic-region is unsteady and two-dimensional, therefore the absolute Mach number gradient is not expected to provide the only reason for the shocks absence despite supersonic-to-subsonic flow.



(a) 0 mm **(b)** 10 mm



(c) 40 mm **(d)** 70 mm

Figure 6.31: Mach number contours for P41 = 3 and t_f = 600 μs. D (mm) : **(a)** 0, **(b)** 10, **(c)** 40, and **(d)** 70.

6.6.4 Behaviour of the Oblique shock

We now consider the gross instantaneous behaviour of the oblique shock by variation of the independent parameters: D and P41. Simulation results of Mach number contours for P41 = 6 and 9, are shown in figures 6.32 and 6.33 respectively, for a fixed time (t_f = 600 μs) and at various values of D.

For P41 = 6 and D = 0, 10, and 40 mm, in figure 6.32, no oblique shock was present rather a compression fan was found to develop towards the rear-end of the separation bubble. This compression fan would, at a later stage, coalesce into a shock. In this figure, at D = 70 mm, the oblique shock was evident at the base of the separation bubble extending a finite height into the supersonic region and then terminating as a compression fan.

There was insufficient information available to ascertain why no shock develops or what the critical criteria are for the development of the oblique shock, with reference to figures 6.32 and 6.33 respectively. From section 6.6.2, for the values of P41 considered in the present study, it was shown the supersonic region would exist in absence of an oblique shock. This was explored further in section 6.6.3 for P41 = 3, where no shock developed within the supersonic region yet such a region was present. In section 6.5.5, it was shown the shape of the separation bubble to differ between P41 = 3 and P41 = 6 and 9. Therefore, the

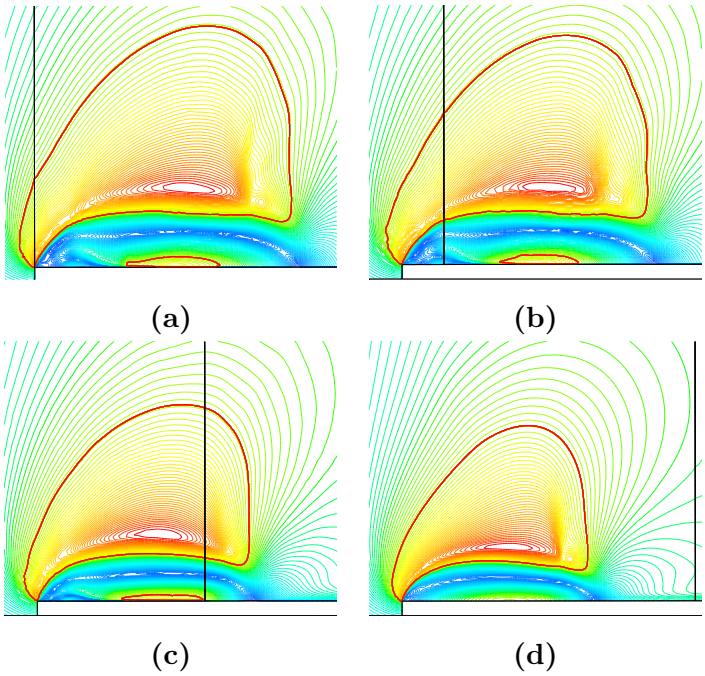


Figure 6.32: Contour plots of Mach number for P41 = 6 and t_f = 600 μs. D (mm) : **(a)** 0, **(b)** 10, **(c)** 40 and **(d)** 70.

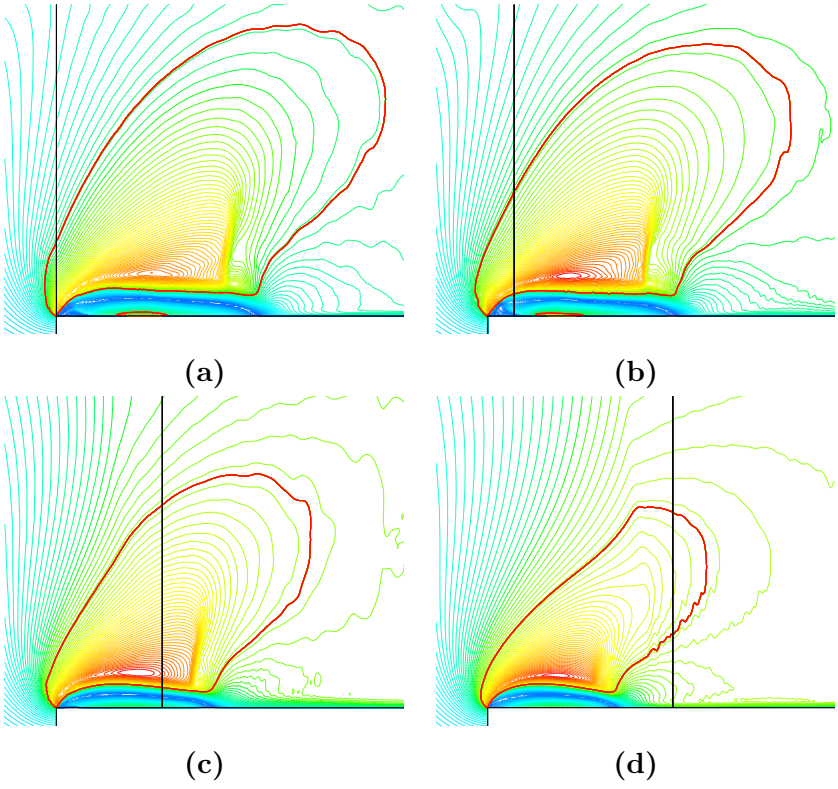


Figure 6.33: Contour plots of Mach number with supersonic region, for P41 = 9 and t_f = 600 μs. D (mm) = **(a)** 0, **(b)** 10, **(c)** 40, **(d)** 70.

shape of the separation bubble may influence the formation of this oblique shock. Other possible reasons may be, to consider the Mach number gradient in the vertical and horizontal

directions and the unsteady flow field within the super sonic region, and the shape of the separation bubble.

6.6.5 The Re-Compression Shock

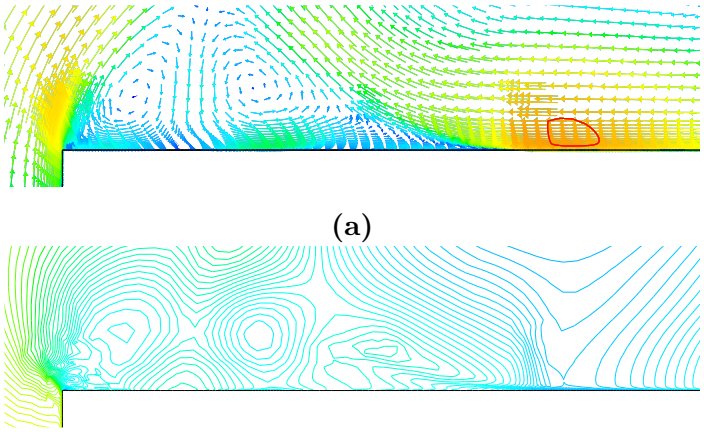
In figure 6.31 (a), a supersonic region was observed within the primary separation bubble and against the horizontal wall. The supersonic region, in this figure, was terminated by a shock, termed a *re-compression shock*. This shock was similar to that observed in a case of shock diffraction over a backward facing step. The re-compression shock was observed to occur for $D = 0$ mm and at P41 = 3, only.

The supersonic flow on the horizontal wall was required to follow the circulatory path of the primary vortex and therefore, was required to separate. This flow separation occurred on the horizontal wall and away from the 90° corner and for P41 = 3, this was clearly observed in figure 6.31 (a-c) and was not observed for $D = 70$ mm. To achieve this flow separation on the horizontal wall, the re-compression shock would decelerate the flow from super- to subsonic speeds. At P41 = 6 and 9, in figures 6.32 and 6.33 the visibility of flow separation on the horizontal wall was less clear, perhaps due to the shape of the separation bubble.

Vector plots of velocity magnitude are shown in figures 6.34 and 6.35 to illustrate the fluid motion at the supersonic region for P41 = 3 and 6 respectively. The no-slip condition must prevail at the horizontal wall boundary, however supersonic conditions are rapidly obtained just above this wall boundary, observed in the zoomed-images. This would imply very high gradients of velocity *normal* to the wall where the supersonic region appeared. (These images correspond to figures 6.31 (a) and 6.31 (b), respectively). It would be interesting to establish the wall shear stress or experimentally prove this behaviour by considering the following conditions: P41 = 6, the diaphragm positioned close to the diffraction corner ($D < 40$ mm) and long experiment test-times ($t_f > 600$ μs).

From the density contour plots in figures 6.34 and 6.35, the boundary layer on the horizontal wall boundary clearly separated. This resulted in the formation of a secondary shear layer, but was found not to re-attach at a point along the horizontal wall boundary near the diffraction corner. Rather, this separated flow partly continued along the path of the primary vortex and partly fed into a number of driven vortices close to the diffraction corner. The near-corner flow structure, including the presence of the driven vortices was explored in greater detail in section 6.5.1.

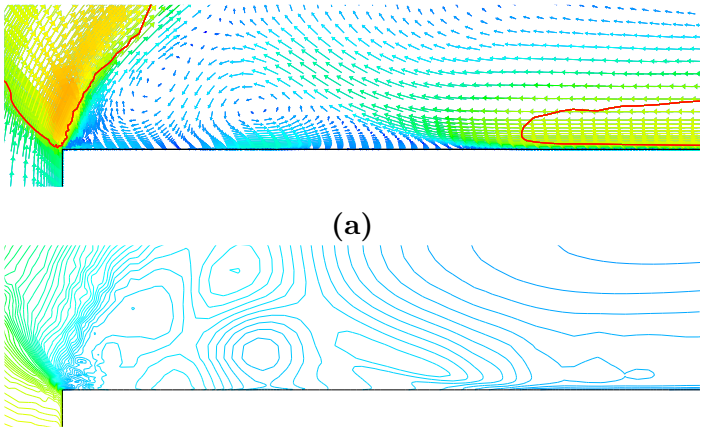
It is interesting to note the size of the supersonic region near the horizontal wall and within the primary separation bubble, which appeared larger for P41 = 6 than P41 = 9. Also, the



(a)

(b)

Figure 6.34: Contour plots of, **(a)** Mach number and, **(b)** density to illustrate the re-compression shock. P41 = 3, t_f = 600 μs and D = 40 mm.



(a)

(b)

Figure 6.35: Contour plots of, **(a)** Mach number and, **(b)** density to illustrate the re-compression shock. P41 = 6, t_f = 600 μs and D = 40 mm.

shape of this supersonic region was somewhat elliptic and absent of a shock at these higher values of P41. This was, maybe, due to the shape of the primary separation bubble being elliptic, a consequence of P41. Boundary layer separation, on the horizontal wall and near the diffraction corner seemed to develop a less-steep, curved profile compared to P41 = 3 This type of profile may have caused deceleration of the supersonic flow to occur in absence of a re-compression shock.

6.7 Sonic and Supersonic Flow Conditions

We now consider the diffraction of a one-dimensional incident expansion wave over a 90° corner where the downstream flow Mach number beyond the trailing characteristic is sonic or supersonic ($M_f \geq 1$). From chapter 3, section 3.3.2.1, the minimum diaphragm pressure ratio required, for a planar, one-dimensional expansion wave to accelerate a gas particle to sonic speed ($M_f = 1$) was established at P41 = 10.4, in an air-filled shock tube ($\gamma = 1.4$). For P41 > 10.4, *supersonic following flow* would be achieved beyond the trailing characteristic. Three values of P41 were considered and were: 12, 15, and 18. Results are reported for P41 = 12 and 15 whereas results for P41 = 18 was similar and appears in Appendix D.

6.7.1 Euler Solver

For P41 > 10.4, an excellent, qualitative comparison was drawn between the Navier-Stokes solver with Menters SST k-ω turbulence model and Euler solutions. The region of the flow field concerned was immediately away from the separation bubble and wall boundaries. This comparison appears in figure 6.36 for P41 = 15 and for $D = 0$, 10 and 40 mm, at $t_f = 300$ μs.

From figure 6.36, it was evident that the shape of the oblique shock for $D = 0$ and 10 mm (frames (a) and (b) respectively), is similar between the Euler and Navier-stokes solver. However, no clear shock was formed for $D = 40$ mm in frames (e) and (f) where the shock structure for the viscous case at $D = 40$ mm (frame f), appeared rather diffuse. The shape of the supersonic region, for all values of D in this figure, appeared similar for the Euler and Navier-Stokes solutions.

The gross shape of the separation bubble, for both solvers, was elongated, thin and attached to the horizontal wall especially for $D = 0$ and 10 mm. This was expected as, concluded in section 6.5: for increasing values of P41 and fixed D, this would lead to an increasingly elliptic separation bubble that remained attached to the horizontal wall in absence of rig dependent effects; this result was for P41 < 10.4. Some difference in the bubble shape between these two solvers was observed, as indicated in the previous paragraph, which may be attributed to a displacement thickness effected by the boundary layer on the horizontal wall for the viscous solver.

For $D = 0$ mm, both solvers resolved the reflected compression waves generated by perturbation signals from the 90° corner by diffraction of the incident expansion wave. These reflected

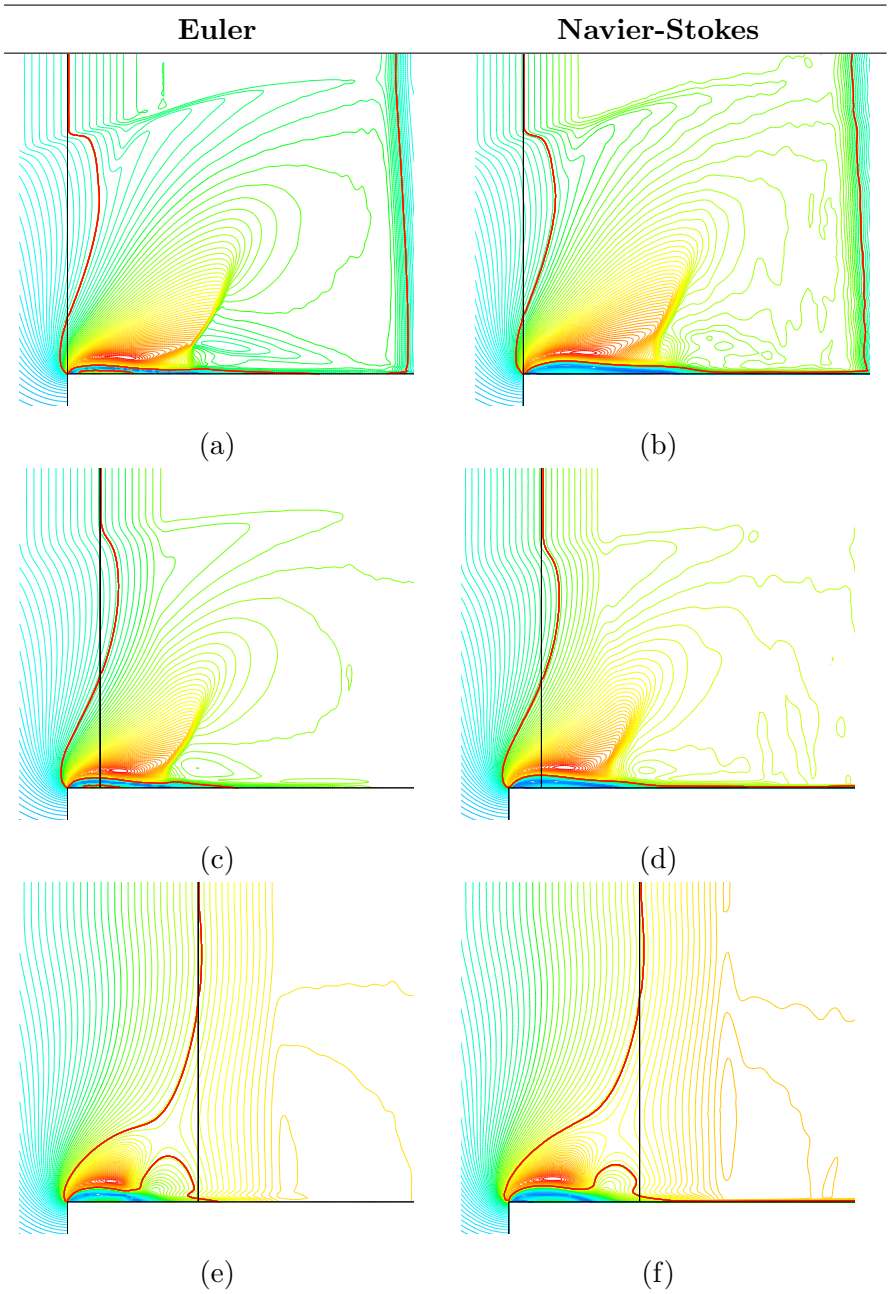


Figure 6.36: Comparison between Euler (Left column) and Navier-stokes (Right column) solutions by Mach number contours for P41 = 15 and $t_f = 300$ μs. D (mm): (**a**, **b**) 0, (**c**, **d**) 10, and (**e**, **f**) 40.

waves was observed to readily coalesce into a cylindrical shock wave. Clearly, this flow feature can be modelled by an inviscid (Euler) analysis.

It is proposed that experimental data would be required for P41 $>$ 10.4 to confirm the obtained simulation results, especially with regards the separation bubble where, purely an extensive simulation analysis may not be advised. It was hypothesised that the observed shock structure should develop in an experiment for P41 = 15 in air ($\gamma = 1.4$) and likewise

for P41 = 12 and 18. Therefore, the Euler solver was favoured due to reduced computational time and was considered sufficiently accurate for a gross, qualitative analysis of the external flow field, from just beyond the separation bubble.

6.7.2 Flow Features for P41 > 10.4

The gross flow field for the diffraction of the incident (one-dimensional) expansion wave over a 90° corner for P41 $\geq$ 10.4 was similar to that for the subsonic cases, $M_f < 1$; achieved for P41 < 10.4. The gross flow field contained the oblique shock, a slip-line, a supersonic region, and a reflected compression wave. The oblique shock and the slip-line can be observed in figure 6.37 whereas the remaining flow features appear in figure 6.38.

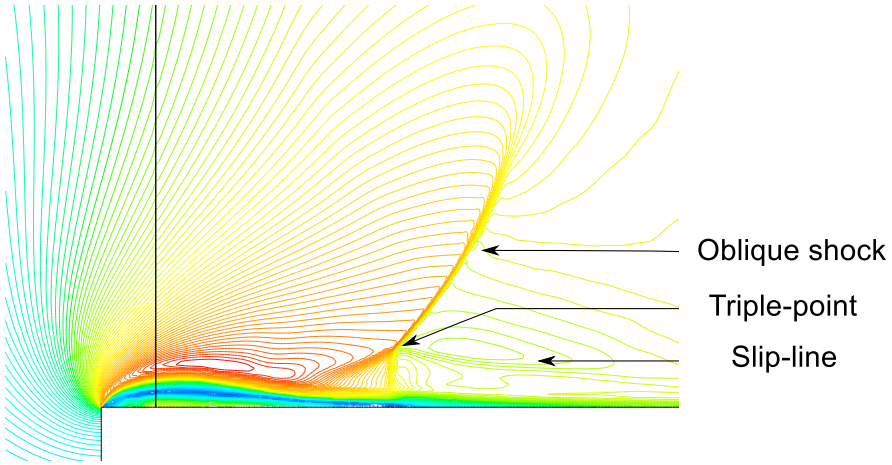


Figure 6.37: Contour plot of Mach number to illustrate flow features towards the separation bubble for supersonic following flow. P41 = 15, D = 10 mm and t_f = 500 μs.

The instantaneous diffraction of the expansion wave is illustrated in figures 6.39 and 6.40 for a left-running expansion wave where the diaphragm position formed a part-boundary for the supersonic region. This region was identified by a trace of Mach 1 flow, therefore, the characteristic at the diaphragm location can be considered as the *sonic characteristic* at which point the flow velocity and local sound speed are equal. For P41 = 10.42 in air (γ = 1.4), the sonic characteristic would coincide with the trailing characteristic of the incident (one-dimensional) expansion wave.

A primary difference between P41 $\geq$ 10.4 and P41 < 10.4 is the propagation of the incident expansion wave. In the Preliminary chapter 3, section 3.3.2.1, the motion of a one-dimensional expansion wave for P41 $\geq$ 1, was considered for a quiescent gas of uniform properties in a shock tube. The important aspect was: the trailing characteristic would propagate upstream unless P41 = 10.4, then the trailing characteristic would remain stationary. In particular, for

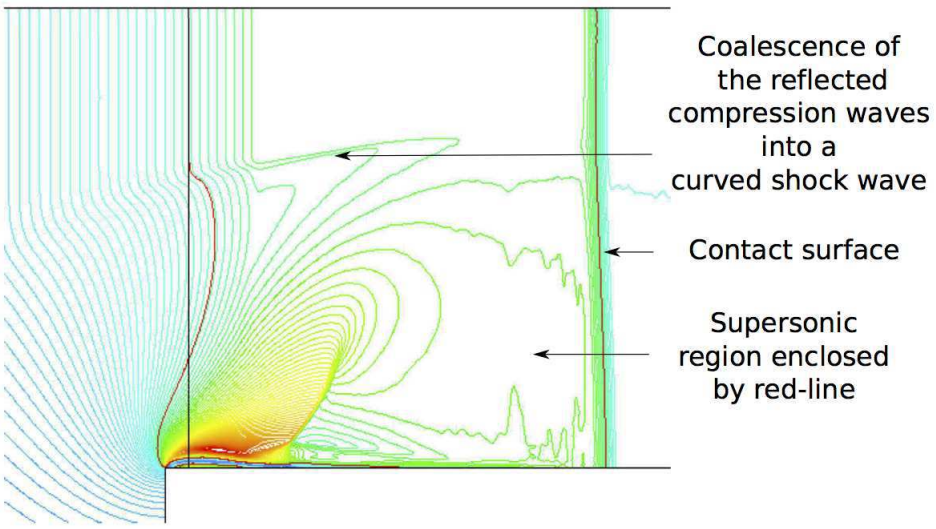


Figure 6.38: Contour plot of Mach number to illustrate flow features away from the separation bubble for supersonic following flow. P41 = 15, D = 10 mm and t_f = 500 μs.

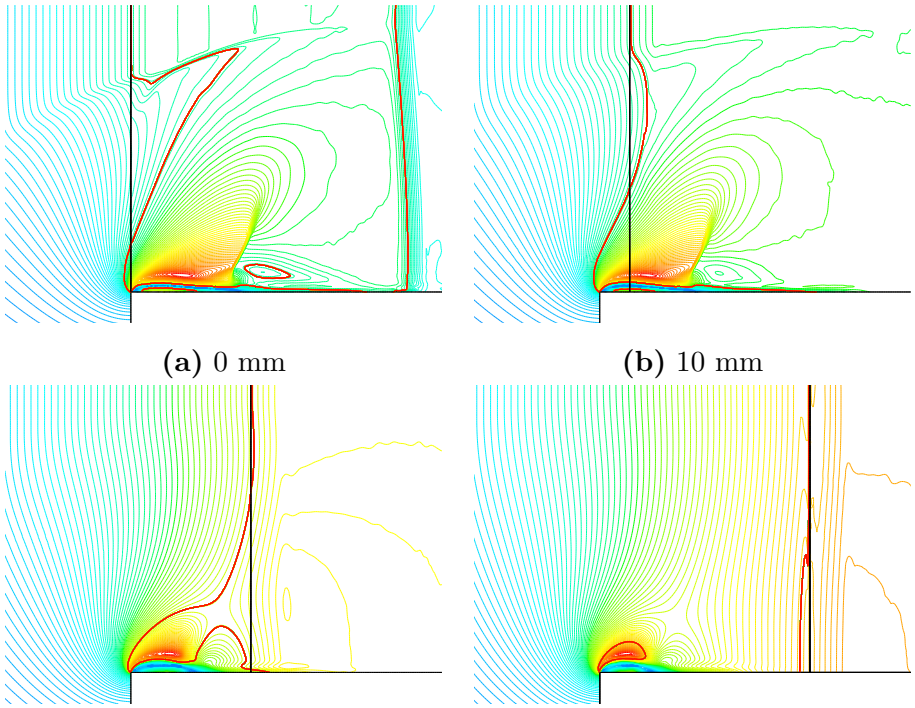
P41 > 10.4, the portion of the expansion propagating upstream would lie between the sonic and trailing characteristics.

6.7.3 Analysis of the External Flow Field

The behaviour of the gross flow features were explored for P41 = 12 and 15, at four values of D (0, 10, 40 and 70 mm), and are shown in figures 6.39 and 6.40. These figures are for 300 μs, a similar set of images are shown, at later time of 600 μs, in figures 6.41 and 6.42. With reference to these figures, the gross flow features considered: oblique shock, the supersonic region, and the reflected compression waves are discussed separately.

6.7.3.1 The Oblique Shock

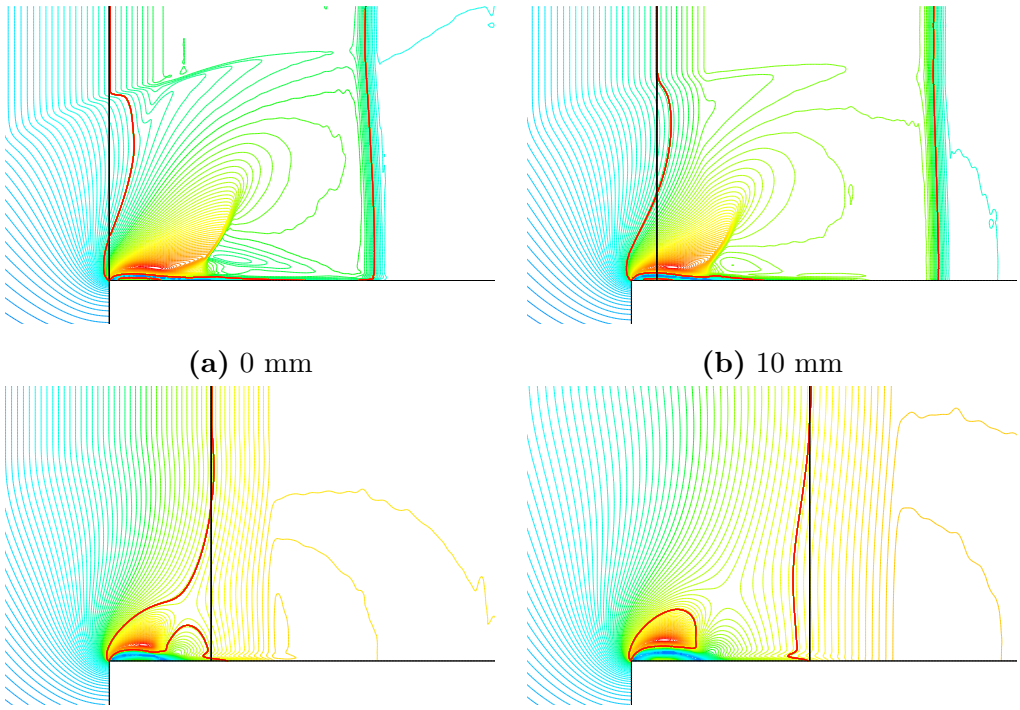
The oblique shock, identified in section 6.6 for P41 < 10.4, is evident in figures 6.39 and 6.40. However, the shock structure is different in that a triple point developed near the separation bubble and the oblique shock had excessive curvature. The shock was oblique, since the flow immediately downstream of the shock was within the supersonic region i.e. the flow had not shocked-down to a subsonic Mach number as would occur for a normal shock. From these figures, the oblique shock and triple point was observed to develop at small D (0 and 10 mm) and for t_f = 300 μs.



(a) 0 mm **(b)** 10 mm

(c) 40 mm **(d)** 70 mm

Figure 6.39: Contour plots of Mach number to emphasize the shock structure with variation in D. P41 = 12 and t_f = 300 μs.



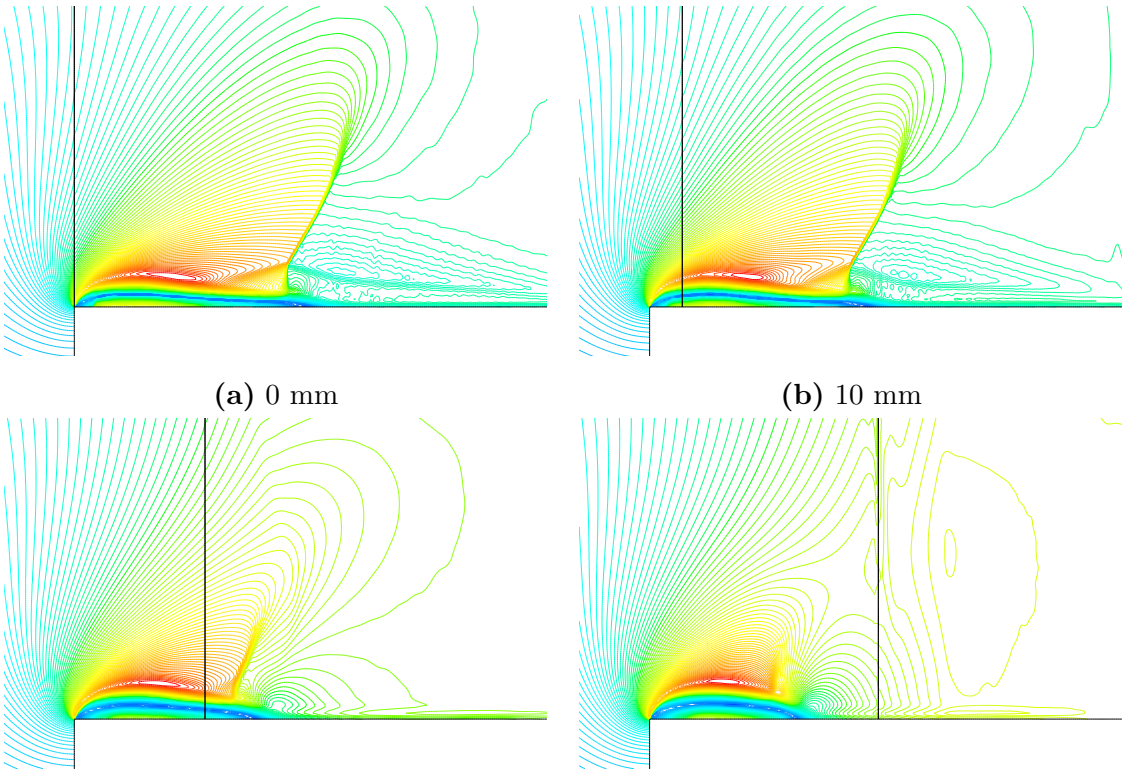
(a) 0 mm **(b)** 10 mm

(c) 40 mm **(d)** 70 mm

Figure 6.40: Contour plots of Mach number, to emphasize the shock structure, with variation in D. P41 = 15 and t_f = 300 μs.

The shock structure at a later time, shown in figures 6.41 and 6.42 indicated the oblique shock formed at $D = 40$ mm and was at early stages of development for $D = 70$ mm. However, no triple point was established at this later time of 600 μs.

To conclude, the effect of increasing D was to delay the formation of the oblique shock and triple point. This result was independent of P41 > 10.4. A possible reason may be attributed to the shape of the separation bubble which, for increasing D, the bubble shape was observed to be less elliptic. This effect would change the profile of the upper surface of the separation bubble where a favourable bubble shape developed sooner for small D (0 and 10 mm) and at later times for larger D (40 and 70 mm).



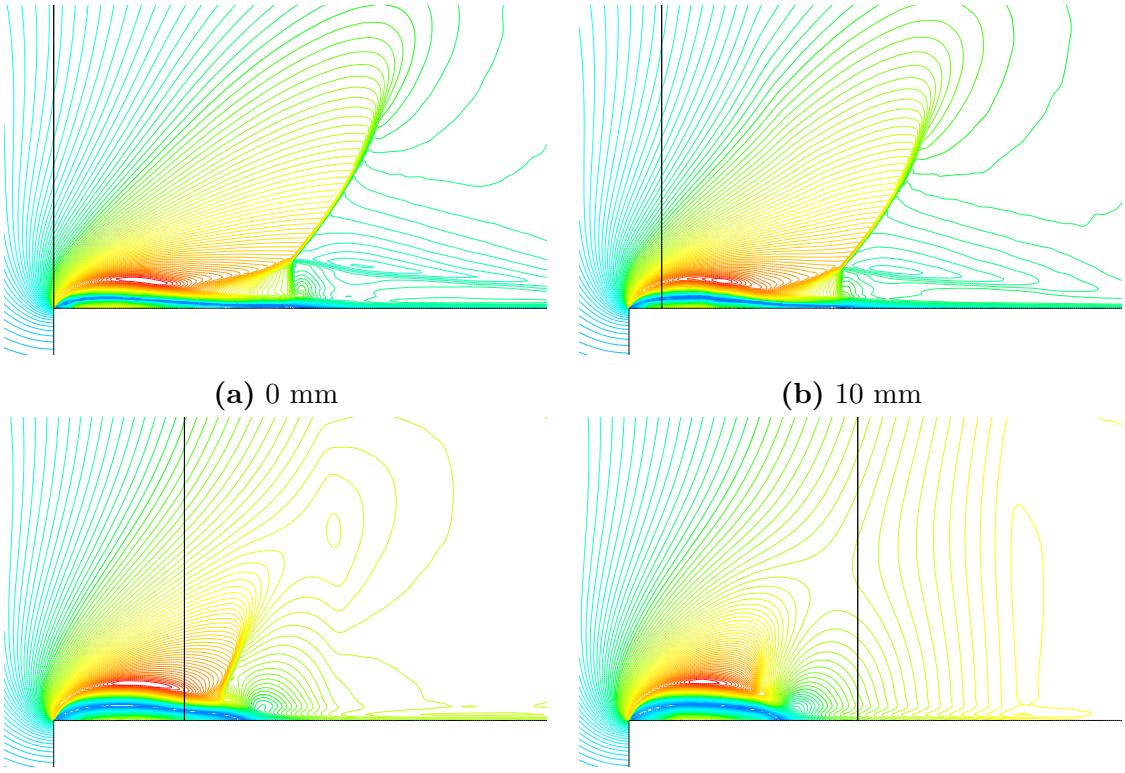
(a) 0 mm **(b)** 10 mm

(c) 40 mm **(d)** 70 mm

Figure 6.41: Contour plots of Mach number, to emphasize the shock structure, with variation in D. P41 = 12 and $t_f = 600$ μs.

6.7.3.2 The Supersonic Region

In figures 6.39 and 6.40, the supersonic region was defined between the sonic characteristic located within the incident expansion wave and the contact surface. As expected, the sonic characteristic remained stationery at the origin of the incident expansion wave where the origin coincided with the diaphragm location. The curved portion of the sonic characteristic was modified by outward propagation of the reflected compression wave. Except for $D = 70$



(a) 0 mm **(b)** 10 mm

(c) 40 mm **(d)** 70 mm

Figure 6.42: Contour plots of Mach number, to emphasize the shock structure, with variation in D. P41 = 15 and t_f = 600 μs.

mm where the diaphragm was relatively far removed from the 90° corner, the oblique shock, the separation bubble and the cylindrical shock wave were contained within the supersonic region.

The elliptical subsonic region for D = 0mm, in figures 6.39 and 6.40, could be an anomoly of the Euler solver as such result was not obtained with the viscous solver shown in figure 6.36. However, no comment could ascribed to the dome-shaped region located for D = 40 mm in figures 6.39 and 6.40 which was was found to develop for the viscous solver in figure 6.36.

6.7.3.3 The Reflected Compression Waves

It was noted for small D, (0 and 10 mm) that the reflected compression wave generated at the 90° corner by diffraction of the incident expansion wave soon coalesced into a cylindrical shock wave. This result can be observed in frames (a) and (b) of figures 6.39 and 6.40, respectively. This result was similar for that obtained for P41 < 10.4, discussed in chapter 6, section 6.4.

The outward propagation of this reflected wave including the cylindrical shock wave was not radial as concluded for P41 $<$ 10.4. The coalescence of the reflected waves was observed to occur where the waves direction of travel was predominantly along the positive vertical direction relative to the mean shock tube flow (horizontal). This result was expected since the mean flow Mach number was supersonic and therefore the sonic pulses of the reflected wave would not propagate downstream.

7 Conclusions

The primary objective of this work was to explore, through shock tube experimentation and simulation, the fundamental behaviour of expansion wave diffraction around a 90° corner. The experiment embodied shadowgraph and schlieren results. For the simulation, it was found that a Navier-stokes solver, with Menters SST k-ω turbulence model best matched the experiment findings. However, the Laminar solver closely matched the turbulence model, however, evident in all experiment results was large-scale turbulent structure within and downstream of, the primary separation bubble.

Tests were conducted for P41 = (3, 6, and 9) and for D = (0, 10, 40, and 70 mm). These values of P41 represented subsonic following flow, i.e. subsonic flow between the trailing characteristic and contact surface. Section 7.5, summarised important points for supersonic following flow, where tests were performed for P41 = 12, 15, and 18 for the four values of D as previously mentioned.

Pertinent findings of the study are presented in this Chapter where all results reported are in absence of rig-dependent effects which would occur due to arrival of reflected waves near the 90° corner. All values of *time* reported in this Chapter were measured for when flow was initiated at the 90 ° corner, as discussed in section 6.3.

The organization of this Chapter is topic based, where each topic refers to a particular section within Chapter 6, Results and Discussion.

7.1 Summary of Results for the Major Flow Features

- The major flow features, identified between the high-resolution shadowgraph images and Navier-stokes simulation data using Menters SST k-ω solver are listed below.
  - A shear layer originating close to the apex of the 90° corner,
  - A primary separation bubble with a turbulent vortex core,

- A reflected compression wave generated at the 90° corner by the diffraction of expansion wave elements,
- Coalescence of the reflected compression waves into a weak, cylindrical shock wave,
- An oblique shock positioned towards the rear-end of the separation bubble,
- A re-compression shock located within the primary separation bubble and on the horizontal wall, and
- A secondary separation bubble and mini vortices located within the primary separation bubble and towards the 90 ° corner.

7.2 Summary of Results for the Reflected and Diffracted Waves

- The diffraction of an incident, one-dimensional expansion wave was found to develop a number of distinct regions which were characterized by certain flow elements. These are:
  - The diffracted portion of the expansion wave below the 90° corner which was identified by the curved profile; circular for the leading characteristic and somewhat elliptic for following diffracted waves. It was found, that the diffracted portion of the expansion wave was weaker than the incident one-dimensional wave. Therefore, above and downstream of the 90° corner, a two-dimensional expansion region developed to match flow conditions that prevailed in the steady region between the trailing characteristic and contact surface.
  - A perturbation signal generated at the 90° corner by diffracted expansion waves. This perturbation signal would propagate radially outward and coalesce into a cylindrical shock wave for small values of D, independent of P41.
  - The region of the incident, one-dimensional expansion wave not yet affected by the outwardly propagating perturbation signal generated at the corner.
- The perturbation signal was identified as a *compression wave* front followed by a two-dimensional expansion region.
- This compression wave front would rapidly coalesce into a weak cylindrical shock wave for a narrow-width incident one-dimensional expansion wave. This occurred for $D = 0$ and 10 mm, independent of P41.
- For P41 > 10.4 in air ($\gamma = 1.4$), the mean downstream (horizontal) flow would attain supersonic speed and the reflected compression wave was found not to coalesce along the mean flow direction. Rather, the reflected compression wave propagated and coalesced

into a cylindrical shock wave in the vertical direction, where the vertical flow Mach number was approximately zero.

- From the simulation results, it was observed that the incident, one-dimensional expansion wave attained complete diffraction for low values of the independent parameters: P41 = 3 and $D = 0$ or 10 mm. These parameters were found to influence the development of the cylindrical shock wave and growth rate of the separation bubble.

7.3 Summary of Results for the Separation Bubble

- A separation bubble formed, due to flow separation at the 90° corner and its subsequent downstream re-attachment on the horizontal wall boundary. The separated flow at the corner formed a distinct shear layer. The separation bubble was referred to as the *primary* separation bubble.
- The primary separation bubble was characterized as follows:
  - For P41 = 3, the bubble shape was roughly circular, whereas at P41 = 6 and 9, the bubble became increasingly elliptical.
  - For fixed values of P41, a reduction in the distance between the diaphragm position (D) and the 90° corner, resulted in an increasing bubble shape. The largest bubble shape was obtained at P41 = 3 and $D = 0$ mm.
  - For increasing values of P41, at fixed D, the shape of the separation bubble would become increasingly elliptic (>> *length* to *height* ratio). The bubble would remain attached to the horizontal wall boundary in absence of rig dependent effects.
- The primary separation bubble was found to consist of:
  - A turbulent vortex core,
  - From the simulation, at P41 = 3, the flow was observed to separate on the horizontal wall boundary and near towards the 90° corner. This flow separation was also identified experimentally in the high-resolution shadowgraph images for P41 = 3.2.
  - Just after the flow separated on the horizontal wall boundary, a *secondary* separation bubble within the primary bubble was observed to develop, inculding a number of mini vortices identified close to the 90° corner.
- A stagnation point was located towards the rear-end of the primary separation bubble. At this point, a portion of the flow from the shear layer would continue downstream and portion would be absorbed into the circulatory flow of the separation bubble. Two

mechanisms were identified for the downstream propagation of fluid from the shear layer:

  - The first mechanism was through an instability within the shear layer . Clear structure of this instability was observed in the high-resolution shadowgraph images. These shed-vortices were found to convect downstream and were emitted at some periodic frequency.
  - The second mechanism concerned the downstream flow direction near the stagnation point. It was believed that, this would emerge off the upper periphery of the primary separation bubble and gave rise to the development of a complex wake pattern identified immediately from the rear-end of the separation bubble. However, the flow from the first mechanism would add to the wake pattern which was evident in all experiment results.

- Through schlieren imaging with a horizontal knife-edge, the wake pattern was observed to consist of two, distinct layers. The *first layer* originated at some point, just beyond the stagnation point on the horizontal wall boundary. This layer grew linearly with distance and interacted, in some fashion, with the *second layer*. The second layer, was believed to originate due to vortex shedding and the downstream flow emerging off the rear-end of the separation bubble.

7.4 Summary of Results for the Oblique and Re-compression Shock

- A supersonic region was identified above the separation bubble, for all values of P41 and D. This supersonic region would develop sooner for a combination of small D (0 and 10 mm) and large P41 (≥ 6).
- Embedded within the supersonic region, an oblique shock was observed to develop under certain conditions of P41 and D. These conditions were:
  - No oblique shock developed for P41 = 3 and this result was independent of D.
  - For P41 = 6, the oblique shock was observed to develop for a drawn-out incident expansion wave.A sufficiently drawn-out wave was obtained for $D = 70$ mm.
  - For P41 = 9, the oblique shock was observed to develop at smaller values of D (0, 10, and 40 mm).
- It was shown for P41 = 3, that the flow near the upper periphery of the separation bubble expanded supersonically and was then decelerated back to sub-sonic speed, in

absence of a shock. This result was found to occur for P41 = 6 and 9, prior to oblique shock formation.

- A *second* supersonic region was identified within the primary separation bubble for values of D up-to 40 mm. For a fixed value of P41, the instantaneous size of this supersonic region was found to reduce in length and height for increasing D. This trend was well observed at large values of time (> 600 μs).
- At P41 = 3, this second supersonic region was terminated by a re-compression shock which occurred for $D = 0$ mm only. This was observed for values of time > 600 μs.

7.5 Summary of Results for Sonic and Supersonic Flow Conditions

- For a shock tube generated expansion wave with air ($\gamma = 1.4$), sonic or supersonic flow would exist between the trailing characteristic and contact surface for P41 $\geq$ 10.4.
- The resulting flow features of interest were: the oblique shock, the supersonic region, and the reflected compression waves.
- An Euler solver was found sufficiently accurate for a gross, qualitative analysis of the external flow field from just beyond the separation bubble.
- The separation bubble was confined to a narrow region above the horizontal wall boundary where strong boundary layer effects were anticipated. In absence of experimental data, this flow feature, for P41 $>$ 10.4 was not studied.
- The oblique shock was seated above the rear-end of the separation bubble and was observed to develop a triple point. Excessive curvature of the oblique shock was noted for increasing P41 beyond 10.4.
- For a fixed time of sufficient duration (> 300 μs), the effect of increasing D, was to delay the formation of the oblique shock and the triple point. This result was independent of P41; for P41 $>$ 10.4.
- The supersonic region enclosed a large region of flow bounded by the *sonic characteristic* of the one-dimensional expansion wave and the contact surface; this result was observed for D = (0, 10, and 40 mm). The reflected compression wave generated at the 90° corner by diffraction of the one-dimensional expansion wave was found to modify the sonic characteristic.

- The outward propagation of this reflected wave including the cylindrical shock wave was not radial as concluded for P41 < 10.4. The coalescence of the reflected waves was observed to occur where the waves direction of travel was approximately perpendicular to the mean flow direction.

7.6 Comparison With Shock Wave Diffraction Over a 90° Corner

A brief comparison with shock diffraction over a 90° corner is outlined in table 7.6.

Shock wave	**Expansion wave**
Reflected expansion wave generated by diffraction of a shock wave	Reflected compression wave generated by diffraction of the expansion wave which may coalesce into a weak, cylindrical shock wave.
The shear layer wraps up into a spiral (primary) vortex	The shear layer does not wrap-up into a spiral vortex but rather, the primary vortex is enclosed within a separation bubble. The shear layer forms the outer boundary of this bubble.
The primary vortex develops away from the solid, downstream boundary-wall.	The separation bubble develops against a boundary-wall

8 Recommendations

This chapter presents important recommendations with the objective to further explore expansion wave diffraction. Areas of the study that were highlighted for further research are also discussed.

8.1 Experiment and Simulation

- It would be advantageous to explore, on a larger scale then the present study, the diffraction of the (one-dimensional) expansion waves around a 90° corner. This can be achieved by the design, manufacture and commissioning of a shock tube specially developed to research expansion wave interaction with solid objects.
- To explore the diffraction of the expansion wave over various corner geometries. This can, at later stages, be extended to compound and curved geometries.
- To explore the usage of different driver gas molecular weights which would influence the sound speed of the medium and therefore the propagation of the expansion wave. An alternative may explore various gas temperatures to effect a change in sound speed, however, this may not be advisable due to maintaining a constant and uniform gas temperature in the shock tube.
- Definite structure was observed within the separation bubble and the shear layer. The present study highlighted a complex flow field within the bubble consisting of: a main vortex, mini vortices, a viscous vortex, a secondary separation bubble, and turbulence. It would be required to further confirm these observations experimentally.
- To explore simulation techniques which would resolve the turbulence identified in the shadowgraph images where turbulence was identified within the separation bubble and in the wake region, immediately downstream of the bubble.
- Provide means to add instrumentation upon the horizontal and vertical surface's of the 90° corner to obtain pressure data, or experimentally establish the movement of the

stagnation point for the primary separation bubble. This data may be compared to simulation results as a robust validation technique.

8.2 Further Research

The following were identified as potential areas, within the present study, for further research:

- The fluid behaviour near the stagnation point was found to occur at the wall where boundary layer effects cannot be ignored. Although the Navier-stokes simulation did resolve the boundary layer, experimental studies for this aspect would be preferred. The experimentation can then serve as a validation tool for further simulation studies. Proposed techniques for this aspect may consider PIV or surface pressure measurements along the horizontal wall.

- The oblique shock was identified for certain combinations of P41 and D which otherwise, the shock would be absent in a supersonic region. There was not sufficient information available to ascertain why no shock developed or what the critical criteria were for the development of the oblique shock. It should be noted that the flow field where the oblique shock developed and near the upper periphery of the separation bubble was unsteady, perhaps non-isentropic, and two-dimensional. The shock bubble position was dynamic, although their behaviour may be pseudo-stationery.

- The remark, that the oblique shock and bubble maybe pseudo-stationery, can be extended to the entire flow field generated by the diffraction of the expansion wave at a 90° corner. However, some flow features such as the oblique shock and coalescence of the reflected compression waves into a a cylindrical shock wave occur either later in time or their formation would depend on the choice of P41 and D. Rather, consider the separation bubble instead. Should a plot of x/t and y/t, result in a constant shape for the separation bubble (including that of the other flow features), this would indicate the diffraction process is pseudo-stationery, in absence of rig-dependent effects.

- Shocklets were observed to develop along the curvature of the shear layer, at a region close to the 90° corner. This may have occurred due to transverse variation in the cross-sectional shape of the separation bubble. Some reasons which may lead to such transverse variation were identified as: manufacturing imperfection of the 90° corner test-piece, transverse waves interacting with the near-corner flow structure or slight vibrations from the diaphragm bursting process, although other reasons may exist. It would be worthwhile to investigate the presence and extent of transverse variation in the bubbles shape through oblique imaging techniques.

- The flow structure within the primary separation bubble and near the 90° corner was identified to consist of: a secondary separation bubble, a secondary shear layer and mini vortices. Shadowgraph imaging indicated significantly steep density gradients at the vicinity of the 90° corner. Although not clearly resolved in experiment and simulation, we believe the boundary layer flow the vertical wall should separate and would interact, in some fashion, with the near-corner flow (contained within the primary separation bubble). The nature of this separation could not be identified.

- Experimental data would be required for P41 $>$ 10.4 to confirm the obtained simulation results, especially with regards the separation bubble where, purely an extensive simulation analysis may not be advised. This is proposed, since, the separation bubble was right against the horizontal wall where boundary layer effects are assumed to be largely significant.

References

Anderson, J (2003) "Modern compressible flow with historical perspective." chap. 7. McGraw-Hill New York.

Ansys (2009) "Ansys fluent 12.0 theory guide." .

Brown, K, Brown, T, Lemay, H, and Bursten, B (1996) Chemistry: The Central Science. Prentice Hall.

Budynas, RG and Nisbett, JK (2008) "Shigley's Mechanical Engineering Design." chap. 8. McGraw-Hill.

Glass, II and Patterson, G (1953) A theoretical and experimental study of the shock tube. Tech. rep., University of Toronto Institute of Aerophysics Report No. 2.

Hillier, R (1991) "Computation of shock wave diffraction at a ninety degrees convex edge." Shock Waves vol. 1, no. 2, pp. 89–98. doi: 10.1007/BF01414904. URL `http://link.springer.com/10.1007/BF01414904`.

Kleine, H, Ritzerield, E, and Gtonig, H (2003) "Shock wave diffraction at a ninety degree corner." Computational Fluid Dynamics Journal pp. 142–158.

Law, C, Muritala, A, and Skews, B (2012) "Unsteady separation behind a shock wave diffracting over curved walls." Shock Waves In press.

Mathews, L and Howard, J (1956) "On the vortices produced in shock diffraction." Journal of Applied Physics vol. 27, pp. 223–231.

Ripley, R, Lien, FS, and Yovanovich, M (2006) "Numerical simulation of shock diffraction on unstructured meshes." Computers & Fluids vol. 35, no. 10, pp. 1420–1431. doi: 10.1016/j.compfluid.2005.05.001. URL `http://linkinghub.elsevier.com/retrieve/pii/S0045793005000794`.

Rudinger, G (1955) Wave Diagrams for Nonsteady Flow in Ducts. Van Nostrand.

Shapiro, M (2002) Introduction to Thermal Systems Engineering: Thermodynamics, Fluid Mechanics, and Heat Transfer. Wiley, 1st edn.

Skews, B, Law, C, Muritala, A, and Bode, S (2012) "Shear layer behavior resulting from shock wave diffraction." Experiments in Fluids vol. 52, no. 2, pp. 417–424. doi: 10.1007/s00348-011-1233-9. URL http://link.springer.com/10.1007/s00348-011-1233-9.

Skews, BW (1961) The construction and calibration of a gas shock tube. Master's, University of Witwatersrand.

Skews, BW (1967) "The perturbed region behind a diffracting shock wave." Journal of Fluid Mechanics vol. 29, pp. 705–719.

Takayama, K and Inoue, O (1991) "Shock wave diffraction over a 90 degree sharp corner." Shock Waves pp. 301–312.

Versteeg, H and Malalasekera, W (1995) An introduction to computational fluid dynamics: the finite volume method. Addison Wesley Longman, Boston.

Wright, J (1961) Methuen's Monographs on Physical Subjects: Shock Tubes. London: Methuen & Co LTD New York: John Wiley & Sons Inc.

Appendix A Appendix A: Details of the Verification Check for the Shock Tube Relation

Results from the verification-check, were obtained from Skews [1967] and presented in table A.1. The required input data for the code was the gas type and inital shock tube conditions obtained through measurement from experimentation for pressure and temperature, specified for the driver and driven sections. The output of the code (for the solution of the shock tube relation) was found to agree within reasonable accuracy for the experimentally measured quantity: shock wave velocity (W_1).

The approximated solution from the developed code was then tested with analytically determined results, also obtained from Skews [1967], shown in table A.2. It was found that the analytical data matched the approximated solution better than a comparison with the experimentally acquired data. This was expected since, the experiment data would include elements not accounted for in the analytical development of the shock tube relation which assumes air as an ideal gas and isentropic, one-dimensional flow.

input data		Shock velocity-published.	Shock velocity-calculated.	% error
P41	$T_1 = T_4$ [K]	W_1 [m.s^{-1}]*pub.*	W_1 [m.s^{-1}]*calc.*	
1.83	295.5	390.058	392.194	0.54
2.67	295.5	417.963	424.745	1.62
3.52	295.5	442.427	449.895	1.68
5.97	295.5	487.566	500.903	2.73
9.43	294.5	532.841	547.861	2.81
13.26	294.5	565.176	584.356	3.39

Table A.1: Experimental data to verify the numerical code for the shock tube relation.

P41	M_2-published	M_2-calculated	% error	M_3-published	M_3-calculated	% error
4.34	**0.4798**	0.4719	1.64	**0.5831**	0.5851	0.34
11.39	**0.7209**	0.7269	0.83	**1.047**	1.0492	0.21
24.27	**0.8915**	0.8961	0.52	**1.467**	1.4678	0.05
46.08	**1.015**	1.0188	0.37	**1.864**	1.8658	0.05

Table A.2: Analytical data to verify the numerical code for the shock tube relation.

Appendix B Appendix B: Details of the Equipment and Instrumentation

Specifications are provided for the equipment and instrumentation used in the present study for the experimentation.

B.1 Pressure Sensor and Signal Conditioner

Table B.1, describes calibration constants and manufacturer details. For further studies, equation B.1 is suggested to transform the voltage output in to a pressure reading.

Port	A	B	C	D
Channel	2	3	4	1
Model	PCB Piezotronics 113A21			
S/N	6710	7342	5477	5925
Sensitivity [mV/kPa]	0.7266	4.1944	3.3358	4.5976

Table B.1: Calibration and model data for pressure transducers

$$P_{abs} = \frac{V \times 1000}{k} + P_{atm} \tag{B.1}$$

where k in equation B.1 is the sensitivity constant of the respective pressure transducer in mV/kPa. The units for pressure(P_{abs}) in this equation are kPa and voltage(V) in mV.

The signal conditioner was manufactured by PCB Piezotronics, Model IC^R Signal Conditioner, Model No. 482A22, S/N 6394.

B.2 Oscilloscope

Function: Provide a TTL trigger signal to initiate data capture for the camera unit. Details given in table B.2.

Manufacturer	Yokogawa
Model	DL 1540 Digital Oscilloscope
Sampling rate	8bit 200Ms/s 150 MHz
Model No.	70150
Serial No.	25WY0267F

Table B.2: Model data for the trigger-out oscilloscope

Function: Data capture from outputs of the signal conditioner. Details given in table B.3.

Manufacturer	Isotech
Model	IDS 8064 Digital Oscilloscope
Sampling rate	Maximum 1G Samples/s 60MHz
Model No.	8064
Serial No.	028D076G1

Table B.3: Model data for the trigger-out oscilloscope

B.3 Time Delay Unit and Trigger Box

The trigger box was an in-house manufactured device, which, for an input signal (unspecified), provided a falling edge signal in the range 12-170 mV. No other details were furnished.

The time-delay unit was used to offset and in-put signal by a specified time; the details given in B.4.

Manufacturer	Electro DI
Model	Time delay unit (programmable)
Trigger level	Max. (3.0 V), Min. (0.0 V)
Time-delay range.	50 - 99 998 μs

Table B.4: Model data for the time-delay unit

B.4 High Resolution and High-Speed Camera's

The primary data aquisition units were the high resolution and high speed camera's (digital). The high - resolution camera was a standard DSLR Nikon D40 10 MP. An in-house manufactured electric-arc xeon light source was used. Flash duration was 1 μs.

Details for the high-speed camera is given in table B.5. The light source was photography grade flash by Canon. Flash duration was $\approx$ 50 μs and Model type: Speedlite 430EX ||.

Manufacturer	Photron
Model	FASTCAM SA5
Model No.	775K − C1
Serial No.	362429074

Table B.5: Model data for the high-speed digital camera

Appendix C Appendix C: Establishing the Onset of Rig-Dependent Effects

C.1 Rig-Dependent Effects

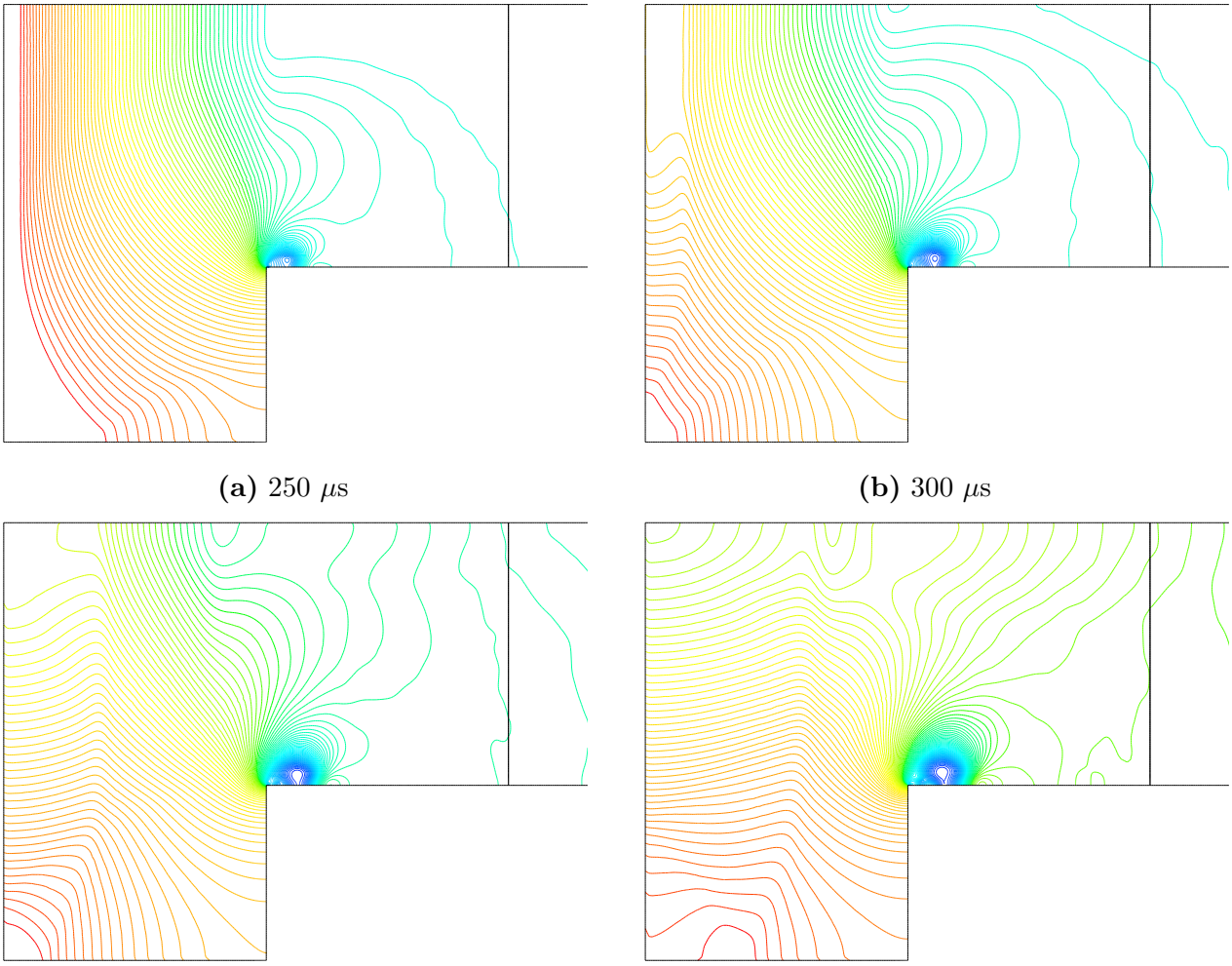
Considering the set of experimental data acquired through experiment and simulation, it was required to establish when secondary flow structures would develop at the 90° corner. These secondary flow structures occur due to reflected waves propagating towards the corner and interacting with a the flow field of interest. This effect, is purely due to the physical size of the experiment domain and referred to as rig-dependent effects. Once secondary flow structures were observed to develop at the 90° corner, the results thereafter were no longer suitable to the studies objectives where the focus was on the primary flow features.

It would be advantageous to have some strong indication of when rig-dependent effects would occur in the experiment. This is now considered where the simulation data (modelled with the *rig-dimain*, served as a guide-line.

A summary of the discussion to follow, for convenience, is provided here: There was a strong indication that rig-dependent effects would occur beyond a measured time of 400 μs in the high-speed image and the corresponding simulation data. For the high resolution images, rig-dependent effects would occur beyond 400 μs time-delay.

C.1.1 Simulation and High-Speed Imaging

It was stated in section 6.3, that the experiment times for the simulation and high-speed imaging data could be measured from a reference position taken at the 90° corner. Therefore, this allowed comparisons to be drawn between these two data sets where the simulation data served as a guide to indicate the time when secondary flow features developed at the corner.



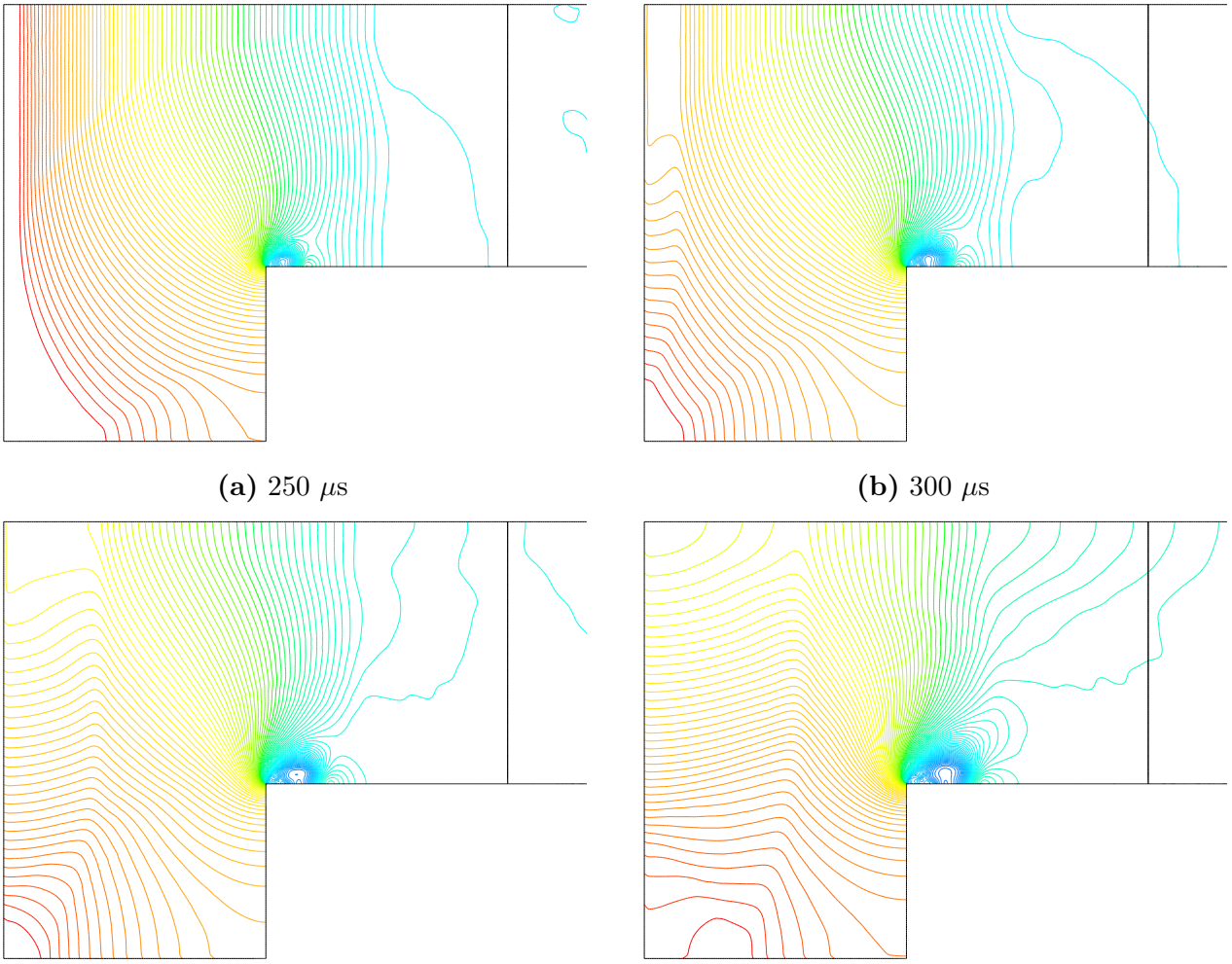
(a) 250 μs **(b)** 300 μs

(c) 350 μs **(d)** 400 μs

Figure C.1: Contours of pressure for P41 = 3.2 at various times, measured from the 90° corner.

C.1.1.1 Simulation Data

Selected images to identify the onset of rig dependency at the 90° corner are shown in figures C.1 and C.2, for P41 = 3.2 and 7.7 respectively. The wave-types of interest are: 1) the leading diffracted wave, 2) the reflected compression wave, and 3) the one-dimensional expansion wave not yet influenced by the reflected compression wave. These wave-types are formally discussed in section 6.4. The pertinent point required is: the reflection of the leading diffracted wave, upon the lower wall boundary, was the first wave-type to arrive at the 90° corner, and therefore initiate the development of secondary flow structures. For a quiescent gas, at a constant and uniform temperature in the driver section of the shock tube, this result is a function of the vertical wall distance below the 90° corner.



(a) 250 μs

(b) 300 μs

(c) 350 μs

(d) 400 μs

Figure C.2: Contours of pressure for P41 = 7.7 at various times, measured from the 90° corner.

In figures C.1 and C.2, the position of these three wave structures are indicated in frame (a) and thereafter focus was upon the position of the leading edge diffracted wave. The arrival of the leading edge diffracted wave at the 90° corner was within 350 and 400 μs in both figures. From these images of iso-pressure contours, the reflected compression wave was observed to reflect off the upper wall boundary at 300 μs for P41 = 3.2 and 7.7. After reflection, its position within the flow domain could not readily be established. However, it was assumed, for the given flow domain geometry in these figures, the arrival of the reflected leading edge diffracted wave was followed by that for the reflected compression wave.

We now consider the high-speed experimental images to identify when rig-dependent effects occur.

C.1.1.2 High Speed Image Data

The simulation results have indicated that rig-dependent effects would occur between 350 and 400 μs. The experiment results may not be identical these values since the simulation represents ideal flow conditions. It was assumed that the measured time, for the experiment, would be close to the result obtained from simulation.

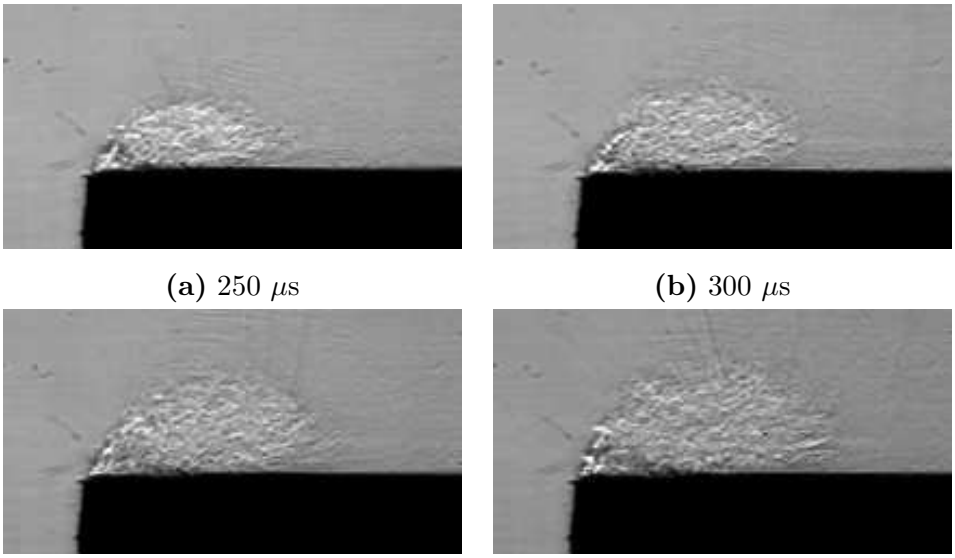
From the high speed shadowgraph image in figures C.3 and C.4, for P41 = 3.2 and 7.7 respectively, a gross change was observed in the separation bubbles structure, occurred in between 350 and 400 μs. In particular, there appeared large-scale breakdown at frame (d), in both figures, corresponding to 400 μs. This break down was noticeable towards the rear-end of the separation bubble and was not present at the earlier frames for these figures.

To conclude, the high-speed shadowgraph results have indicated that the onset of rig-dependent effects clearly developed at a measured time of 400 μs. However, it should be noted that this effect may have occurred between 350 and 400 μs. This result was, too, identified through the simulation results for P41 = 3.2 and P41 = 7.7.

We now consider the high-resolution experiment images to identify when rig-dependent effects occur.

C.1.2 High-Resolution Imaging

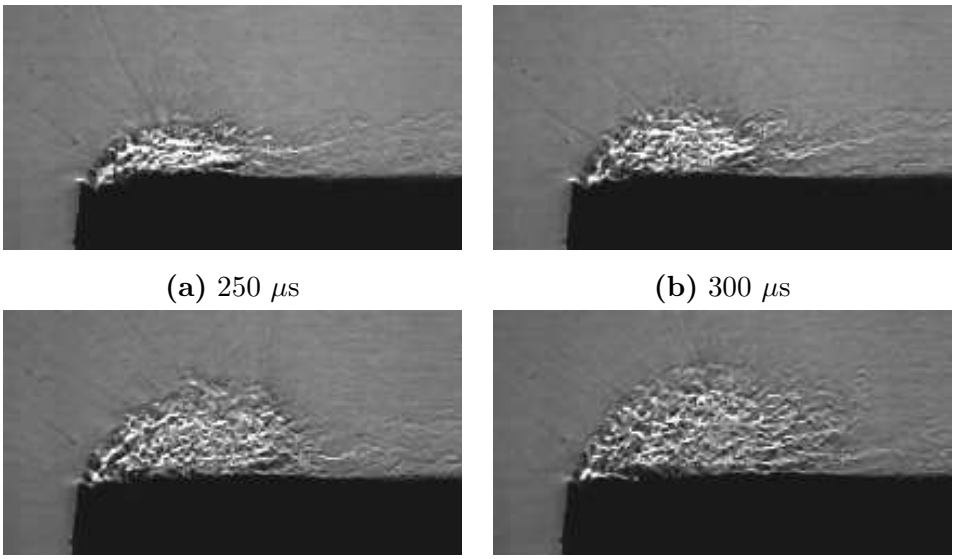
Since it was not possible to establish when flow originated at the 90° corner due to the diffraction of the leading characteristic of the incident expansion wave, an indirect method was devised to establish the onset of rig-dependent effects for the high-resolution images.



(a) 250 μs **(b)** 300 μs

(c) 350 μs **(d)** 400 μs

Figure C.3: High-speed shadowgraph images for P41 = 3.2 at various times, measured from the 90° corner.



(a) 250 μs **(b)** 300 μs

(c) 350 μs **(d)** 400 μs

Figure C.4: High-speed shadowgraph images for P41 = 7.7 at various times, measured from the 90° corner.

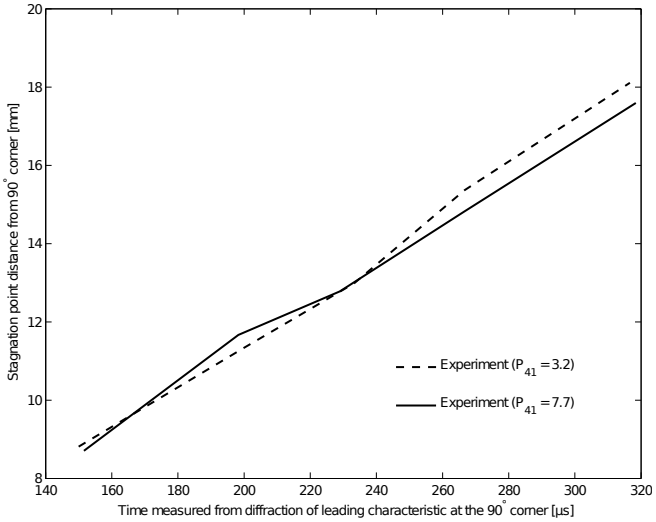


Figure C.5: Plot of stagnation point position from the 90° corner for high-speed shadowgraph data.

C.1.2.1 Establishing Onset Rig-Dependency for High-Resolution Images

From subsection C.1.1, it was concluded that rig dependent effects clearly developed at a measured time of 400 μs, however, the result taken for this measured time was the range between 350 - 400 μs. A similar result was achieved for the high-resolution images where the approach taken was:

The stagnation position from the 90° corner was noted for the measured times considered in the section on *Simulation and High-Speed Imaging* in section C.1.1. These measured times were: 250, 300, 350, and 400 μs. A line plot, in dimensional form, was developed as was similarly done in Chapter 4, Comparison of Results for the *Turbulence Modeling*, in section 5.5. This plot appears in figure.

For a particular high-resolution image, the *distance* of the stagnation position from the 90° corner and the images time-delay was recorded. This *distance* value was entered-with on the y- axis in figure C.5, and the corresponding, measured time, was then obtained. Should this measured time fall within the range of 350 - 400 μs, then this was a strong indication rig dependent effects have occurred, for the time-delay considered of the high-resolution image. A sample analysis is provided below.

Sample Analysis:

Consider a high-resolution image, for example figure C.7 (d) at P41 = 3.2. The measured value of D for this image is $\approx$ 17 mm and at a *time-delay* of 450 μs. The D value was then

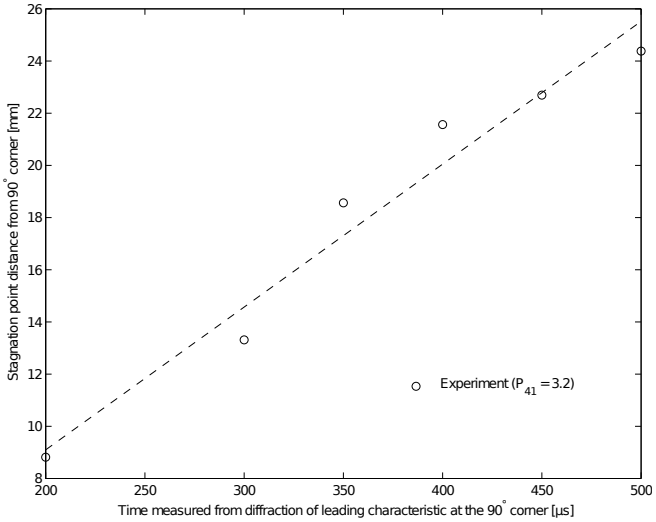


Figure C.6: Identification of rig-dependent effects for the high-resolution data, using a graphical plot of stagnation point position from the 90° corner for the high-speed data.

located along the vertical axis of figure C.5 for the high-speed image data. The corresponding *measured time* was then ≈ 350 μs. Therefore, it was expected that rig-dependent effects have occurred at time-delay images > 400 μs for P41 = 3.2. This procedure was repeated for image C.7 (e) at 500 μs time-delay.

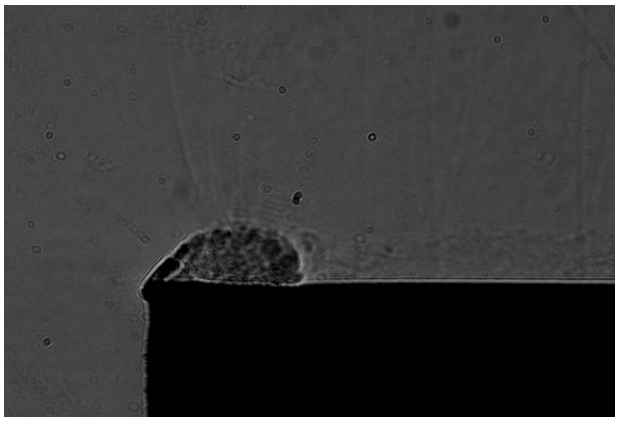
Both procedures are shown graphically in figure C.6. The corresponding measured time was with-in the range of 350-400 μs where rig-dependent effects are expected to have occurred.

C.1.2.2 High-Resolution Image Data

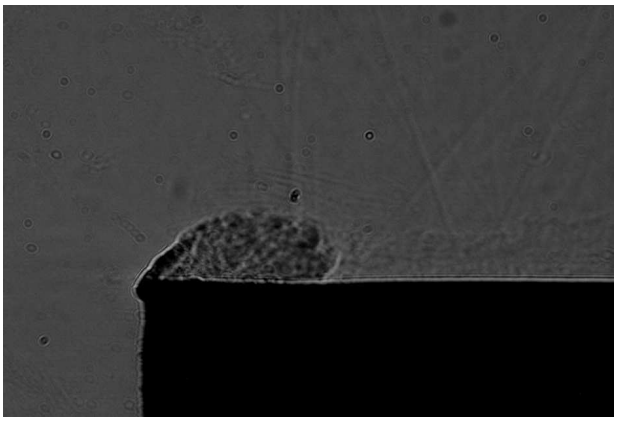
Figures C.7 and C.8 show high resolution images for P41 = 3.2 and 7.7 respectively, at time-delays of: 300-600 μs.

From figure C.7, for P41 = 3.2, the onset of rig dependent effects were found to occur between 450-500 μs time-delay where the separation bubble was found to undergo large scale breakdown. This large-scale breakdown was somewhat observed for the high speed imaging data in section C.1.1 but was evidently clear for these times. This was expected since the high resolution images were able to better resolve the flow field than the high-speed camera. The corresponding *measured time* obtained from figure C.5 was 400-450 μs and therefore a strong indication exists that this result, for the high resolution images, is true.

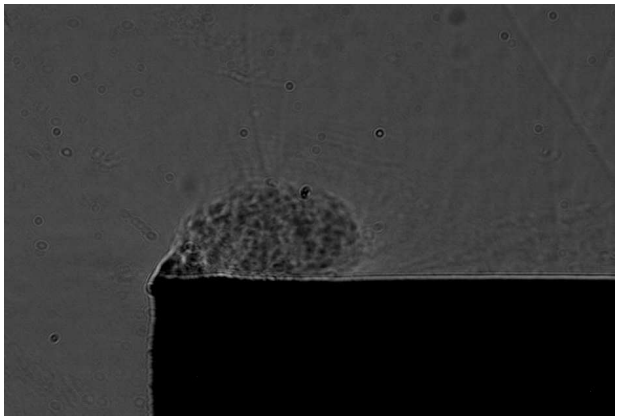
This analysis was similarly applied for P41 = 7.7 in figure C.8. However, the time-delay where large-scale breakdown of the separation bubble occurred at a slightly later time-delay and was evident between 450-500 μs. (The bubble breakdown was significant at 600 μs time-delay).



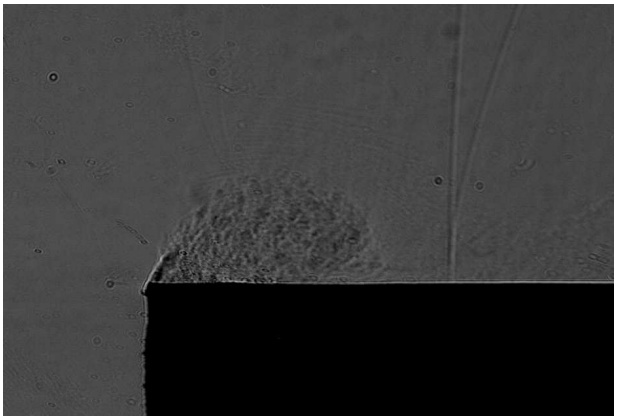
(a) 300 μs



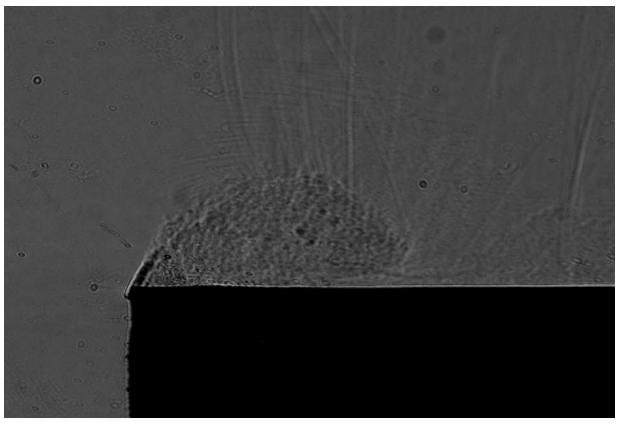
(b) 350 μs



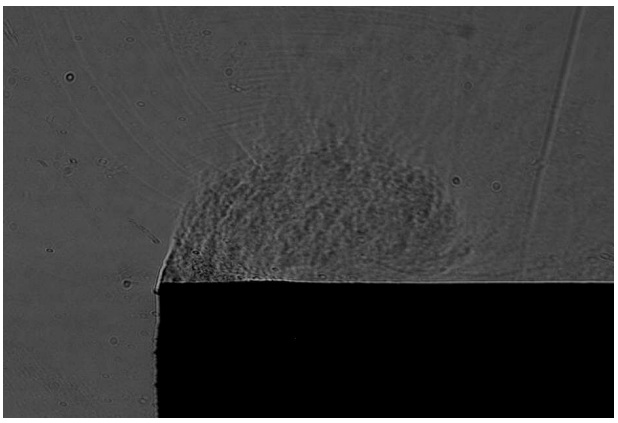
(c) 400 μs



(d) 450 μs



(e) 500 μs

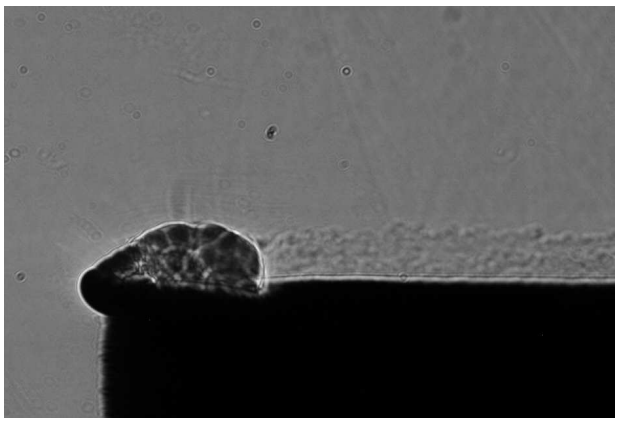


(f) 600 μs

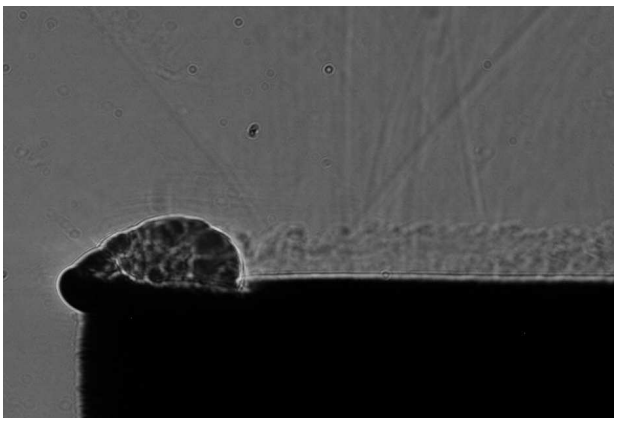
Figure C.7: High-resolution shadowgraph images for P41 = 3.2 at various time-delay values.

The measured time from figure C.5 was beyond 450 μs and therefore, a strong indication of rig dependent effects at these time-delay values for P41 = 7.7.

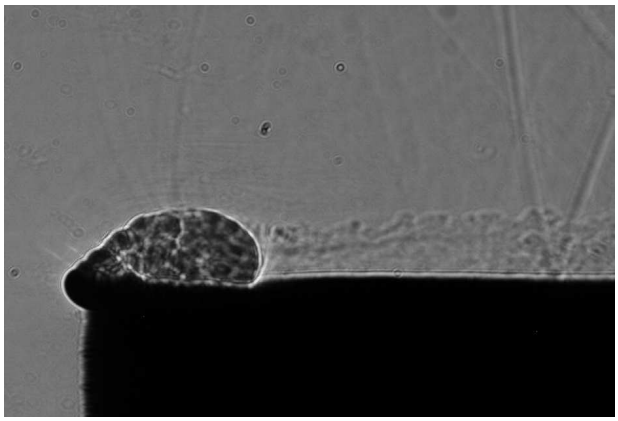
From the high resolution images, it was established that rig-dependent effects occurred sooner for P41 = 3.2 than at a larger value of, P41 = 7.7. By 400 μs time-delay, secondary flow structures would have developed at the 90° corner. Therefore, the high resolution image data



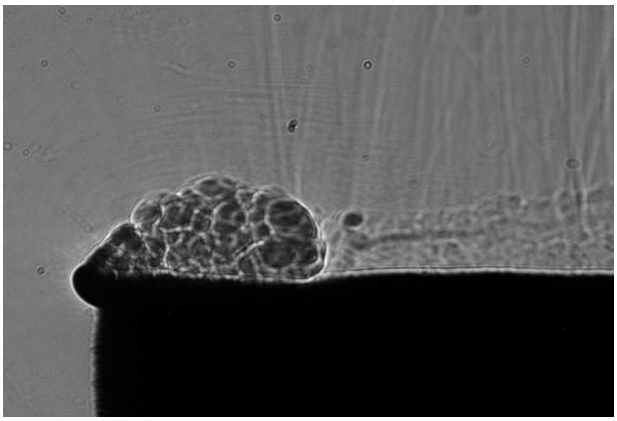
(a) 300 μs



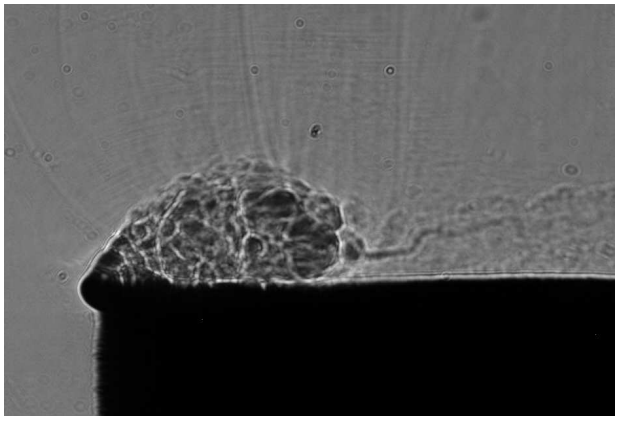
(b) 350 μs



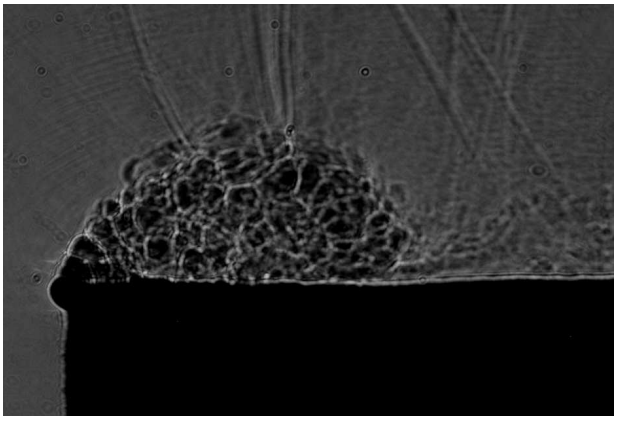
(c) 400 μs



(d) 450 μs



(e) 500 μs



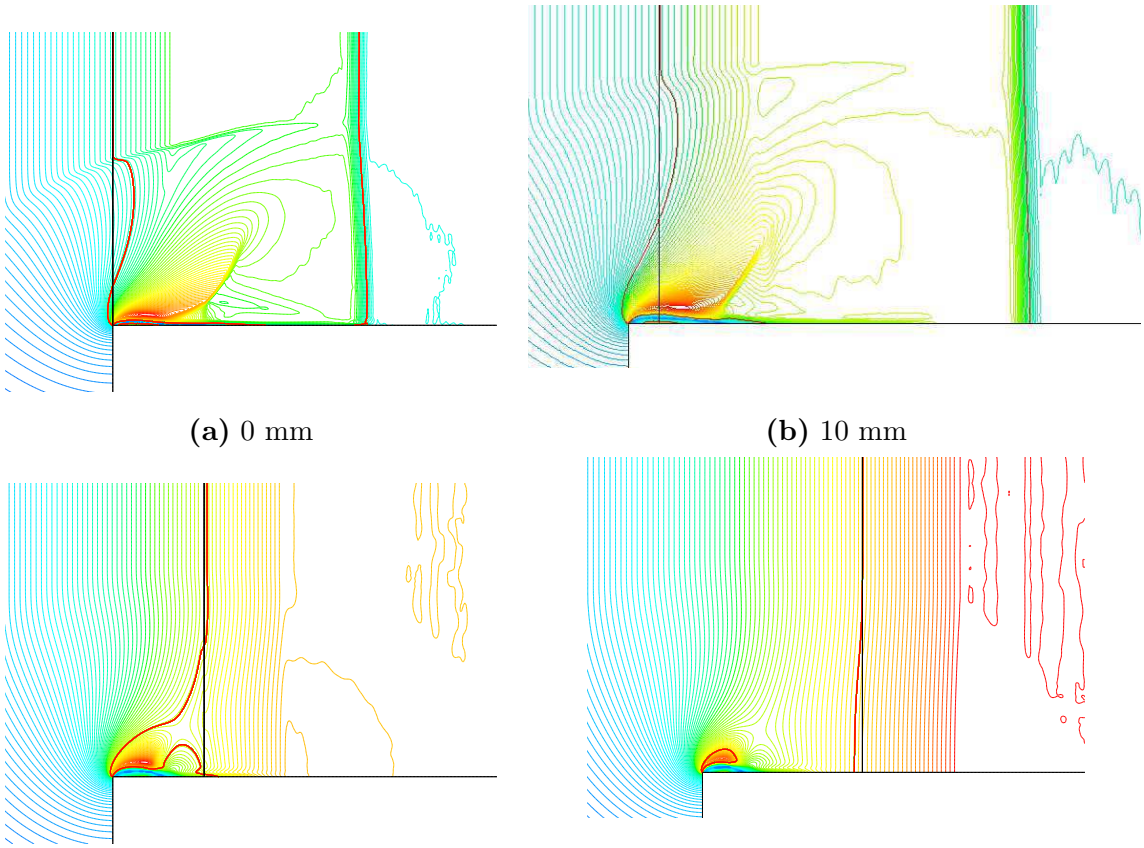
(f) 600 μs

Figure C.8: High-resolution shadowgraph images for P41 = 7.7 at various time-delay values

acquired beyond 400 μs time-delay would not be relevant to the primary objective of the study.

Appendix D Appendix D: Simulation results for P41 = 18

The images which appear in figure D.1, refer to a discussion in chapter 6, sections 6.7 and 6.7.2.



(a) 0 mm

(b) 10 mm

(c) 40 mm

(d) 70 mm

Figure D.1: Contour plots of Mach number, to emphasize the shock structure, with variation in D. P41 = 18 and t_f = 300 μs.

Appendix E Appendix E: Digital Appendix

The digital appendix, which appears on an attached CD, contains scripts produced using the MATLAB programming language to solve for the shock tube relation, in Chapter 3 of this dissertation. The objective of the code was:

1. Obtain P2/P1 for a user specified shock tube state.
2. Calculate P41 to produce sonic conditions at the tail of the one-dimensional expansion wave.
3. Generate various plots.

A flow chart to describe the major steps to obtain P2/P1 using the shock tube relation is outlined briefly in figure E.1.

User inputs the following parameters

Pressure and temperature for the driven and driver sections of the shock tube (P1, T1, P4, T4)

Specific heat ratio and gas molecular weight (γ and *M*)

Evaluate the Right Hand Side (RHS) in the equation shown to the right from the user specified data.

$$\frac{P_4}{P_1} = \frac{P_2}{P_1}\left[1 - \frac{(\gamma_4 - 1)\left(\frac{a_1}{a_4}\right)\left(\frac{P_2}{P_1} - 1\right)}{\sqrt{2\gamma_1\left[2\gamma_1 + (\gamma_1 + 1)\left(\frac{P_2}{P_1} - 1\right)\right]}}\right]^{\frac{-2\gamma_4}{\gamma_4 - 1}}$$

Generate an array of values for the parameter P2/P1 in the equation shown for step 2.

Note: In theory, for
(P4/P1) → ∞,
(P2/P1) → 42
Therefore upper limit in the array for P2/P1 is 42.

Evaluate Left Hand Side in the equation shown in step 2 for each element in the array of P2/P1.

If
L.H.S < R.H.S
and if
the next element in the array of P2/P1 yields L.H.S > R.H.S
Then stop and store the two values of P2/P1 that satisfy this step..

Interpolate between the two stored values of P2/P1 to obtain a more accurate value.

Use P2/P1 to solve for remainder of flow properties in the shock tube following diaphragm rupture.